Modelling the Dynamics of Vibration Assisted Drilling Systems Using Substructure Analysis

Vahid Ostad Ali Akbari

Department of Mechanical Engineering
University of Victoria

A thesis submitted in partial fulfillment of the requirements for the degree of
Master of Applied Science
in the Department of Mechanical Engineering

©Vahid Ostad Ali Akbari, 2020
University of Victoria
All rights reserved. This thesis may not be reproduced in whole or in part, by photocopy or other means, without the permission of the author.

Modelling the Dynamics of Vibration Assisted Drilling Systems Using Substructure Analysis

by

Vahid Ostad Ali Akbari
B.Sc., Amirkabir University of Technology, 2017

Supervisory committee

Dr. Keivan Ahmadi, Supervisor
Department of Mechanical Engineering

Dr. Ben Nadler, Departmental Member
Department of Mechanical Engineering

Abstract

Vibration Assisted Machining (VAM) refers to a non-conventional machining process where high-frequency micro-scale vibrations are deliberately superimposed on the motion of the cutting tool during the machining process. The periodic separation of the tool and workpiece material, as a result of the added vibrations, leads to numerous advantages such as reduced machining forces, reduction of damages to the material, extended tool life, and enabling the machining of brittle materials.

Vibration Assisted Drilling (VAD) is the application of VAM in drilling processes. The added vibrations in the VAD process are usually generated by incorporating piezoelectric transducers in the structure of the toolholder. In order to increase the benefits of the added vibrations on the machining quality, the structural dynamics of the VAD toolholder and its coupling with the dynamics of the piezoelectric transducer must be optimized to maximize the portion of the electrical energy that is converted to mechanical vibrations at the cutting edge of the drilling tool.

The overall dynamic performance of the VAD system depends of the dynamics of its individual components including the drill bit, concentrator, piezoelectric transducer, and back mass. In this thesis, a substructure coupling analysis platform is developed to study the structural dynamics of the VAD system when adjustments are made to its individual components. In addition, the stiffness and damping in the joints between the components of the VAD toolholder are modelled and their parameters are identified experimentally. The developed substructure coupling analysis method is used for structural modification of the VAD system after it is manufactured. The proposed structural modification approach can be used to fine-tune the dynamics of the VAD system to maximize its dynamic performance under various operational conditions. The accuracy of the presented substructure coupling method in modeling the dynamics of the VAD system and the effectiveness of the proposed structural modification method are verified using numerical and experimental case studies.

Table of contents

List of figures

Acknowledgements

I would like to thank the following people, without whom I would not have been able to complete this research. The Dynamics and Digital Manufacturing (DDM) team at the University of Victoria, especially to my supervisor Dr. Keivan Ahmadi, whose insight and knowledge into the subject matter steered me through this research. And special thanks to Mr. Yaser Mohammadi, whose consultation was always a precious help to me.

The axial and axial-torsional VAD systems used in this work were designed by Mr. Joshua Columbus, research associate at DDM in the summer of 2019. I would like to thank Mr. Columbus for his contribution to this project. I would also like thank Mr. Rodney Katz for machining the parts used in the VAD systems and Mr. Patrick Chang for his assistance to design and build their electrical components.

I would like to thank the Canadian Network for Research and Innovation in Machining Technology (CANRIMT) for financially supporting this project.

And my biggest thanks to my family without whose patience, encouragement, and support, I would not be able to achieve this success.

Chapter 1

Introduction

Vibration Assisted Machining (VAM) has attracted a great industrial interest in recent years due to its numerous advantages. In VAM, micro-vibrations with high frequency (around 20kHz) are superimposed on to the cutting motion of the tool during the machining process. A schematic of VAM is depicted in Fig.1.1.

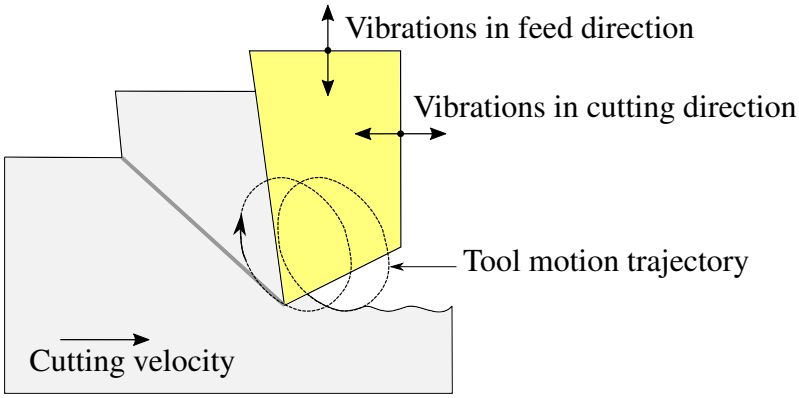

Fig. 1.1 Superposition of small-amplitude of vibrations in VAM [5]

The addition of the micro-vibrations to the material removal process has shown to significantly reduce the generated forces, heat, tool wear, and machining-induced damages to the workpiece. The extent of the effectiveness of the superposed vibrations depends on their frequency and amplitude as well as the cutting speed in the machining process[3, 10, 2]. The velocity of vibrations is proportional to its amplitude and frequency.

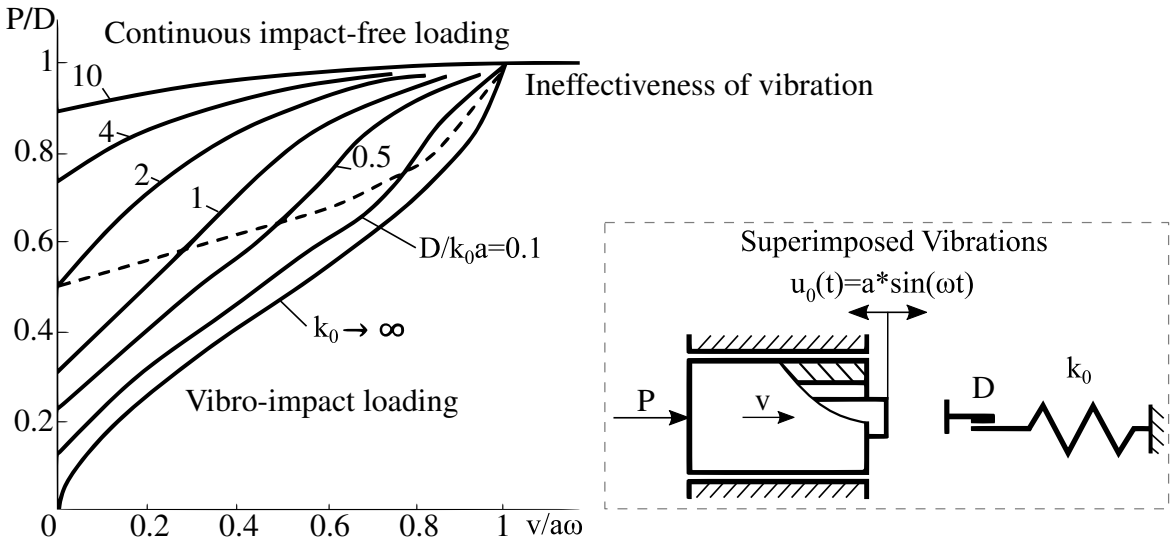

Fig. 1.2 Effect of vibration parameters on VAM process[3]

If the vibration velocity is greater than the cutting speed, the tool intermittently loses contact with the material, converting the chip generation mechanism from continuous impact-free to a vibro-impact process [3]. In vibro-impact regime, because the tool is only in contact with the workpiece in a small portion of time, the average of machining forces decreases. Figure 1.2 represents a model for explaining the effect of superimposed vibrations on the process of plastic deformation. It also contains information about the overall outcome of different values of effective parameters in a VAM process. In this figure, P stands for the average machining force, D for yield strength of the workpiece material, k_0 for static stiffness, v for cutting velocity, a for amplitude and ω for frequency of vibration. The overall displacement of the tool is described by $u(t) = vt + a * sin(\omega t)$. It illustrates that an increase in either amplitude (a) or frequency (ω) of vibration shifts the operational condition state to the left hand-side of the plot which is followed by higher drop in machining forces (P) and increasing the efficiency of VAM [3].

This intermittent cutting phenomena leads to important improvements in various machining operation. Vibration Assisted Drilling (VAD) refers to the application of VAM in drilling operation. These advantages in VAD include a reduction in the drilling thrust force and torque[13, 16, 10, 2] as shown in Fig.1.3, elimination of burr formation [20, 7, 10], increase in material removal rate [3], increasing tool life, improvement in the surface finish, [10] and the elimination of the damages and and deformations to the workpiece during the machining operation. In drilling composite materials, using VAD reduces delamination and fiber pullout compared to conventional drilling [23, 4]. A case in which VAD has reduced delamination is shown in Fig.1.5.

The reduction in the drilling thrust force provides the ability of drilling thin workpieces without unwanted deformations as shown in Fig.1.4 [3]. VAM is also a promising approach for rock sampling in space which is done by surface rovers drilling and retrieving the samples for analysis. Since the gravity in space is not sufficient to provide required thrust force for rock drilling, VAM is a suitable approach [6].

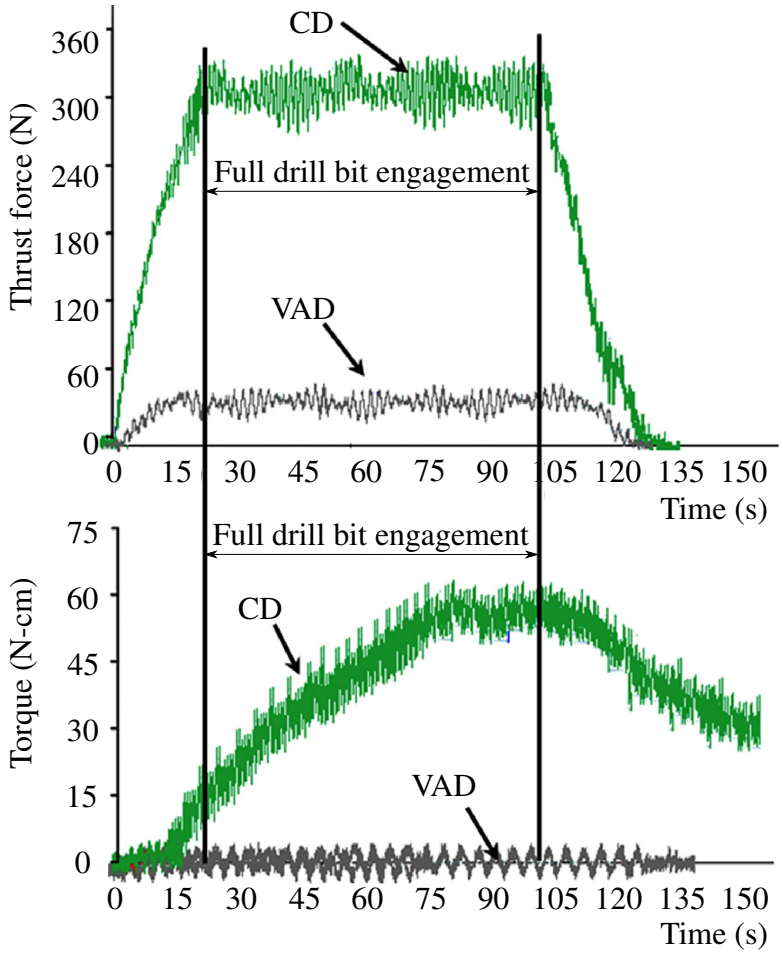

Fig. 1.3 The influence of VAD in reduction of drilling thrust force and torque compared to Conventional Drilling (CD)[13]

According to Fig.1.2, vibro-impact regime can be achieved by reducing the cutting speed, increasing the vibration velocity, or its frequency. Since reducing the cutting speed results in the reduction of productivity, vibro-impact regime is usually generated by exciting the high-frequency resonance modes of the VAD system. Also, the VAD system should be designed so that the highest amplitude of vibration is generated at the tip of the drill bit, where the cutting process occurs.

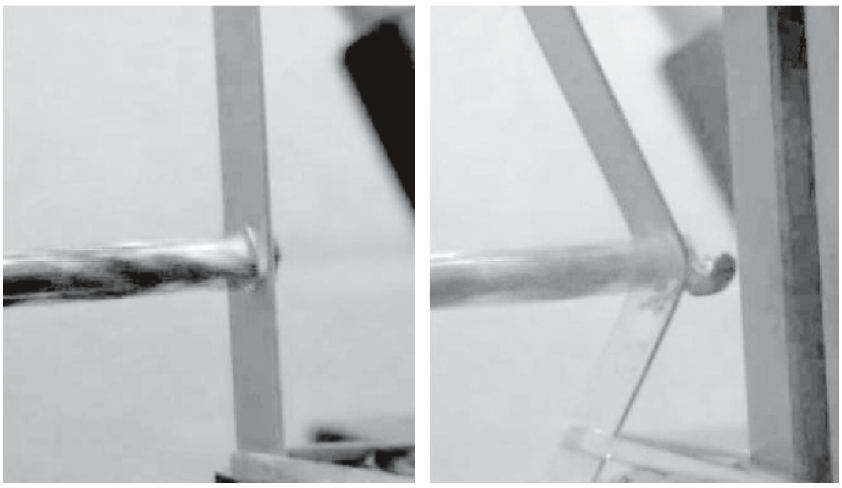

(a) (b)

Fig. 1.4 Reduction in deformation of thin plates in VAD [3]

Typical components of a VAD system are schematically shown in Fig.1.6. Vibrations are generated by providing electrical voltage to the piezoelectric transducers. The generated vibrations are amplified by the concentrator. This component has been designed in various shapes. Concentrators typically have a reducing cross-section toward the drill bit which magnifies the amplitude of vibration at the tip of the drill bit. Concentrator not only magnifies the amplitude of vibrations but also can transform part of the axial vibrations into a torsional motion in axial-torsional VAD system, generating vibrations in both cutting and feed directions. [6, 8, 17, 1, 12]. The back mass is a cylindrical component attached to the rear side of the tool holder. Since the tool holder operates in its first free-free axial mode, a heavy rear part leads to a high amplitude of vibration at the tip of the drill bit. Therefore, in a proper design of a VAD tool holder, the highest amplitude of vibrations corresponds to the tip of the drill bit.[14, 3]

1.1 Research Objectives

The overall dynamic performance of a VAD system is influenced by the dynamics of its individual components and the interactions between them. The primary objective of this project is to develop a computationally efficient method based on substructure analysis that can predict the overall dynamics of the VAD system based on the dynamic characteristics of the its components including the drill bit, concentrator, piezoelectric transducer as an electro-mechanical system, and the back-mass. Such substructure analysis framework will provide an efficient design platform that enables studying the sensitivity of the dynamics of

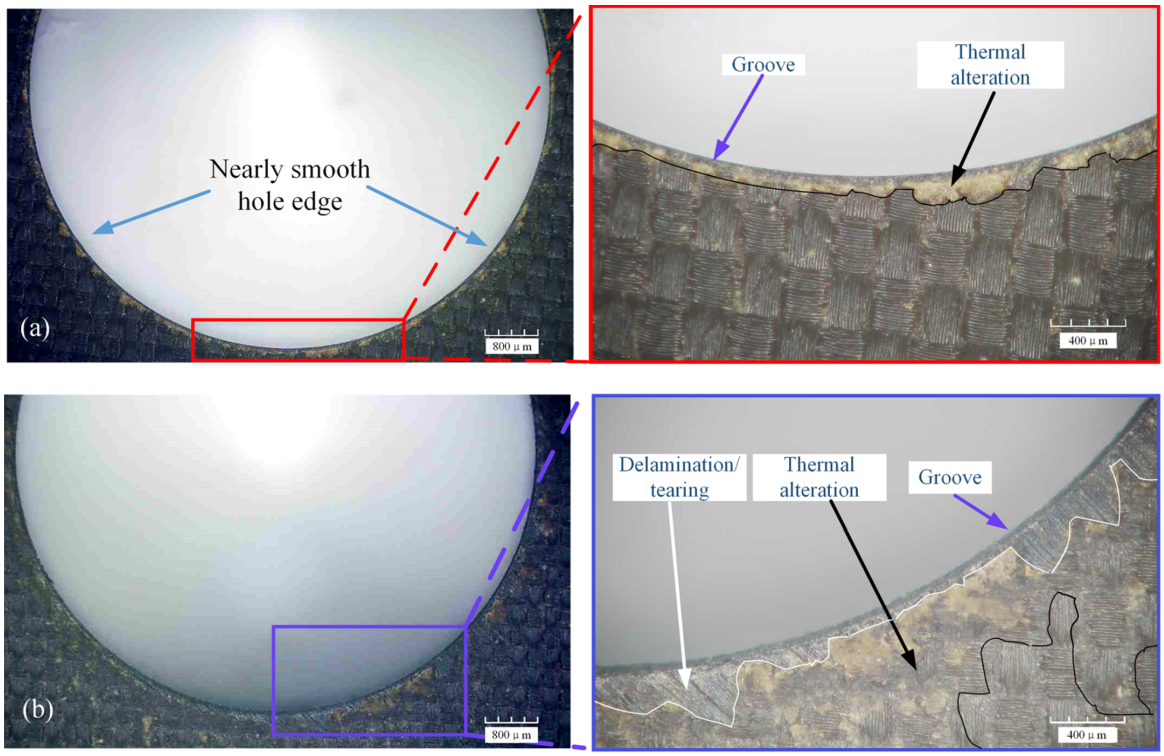

Fig. 1.5 Comparing delamination of composite materials in cases of VAD and conventional drilling [23]

the VAD assembly to variations in the design parameters of each substructure.

In addition to the dynamics of the individual components of the VAD, the dynamics at their interactions also influence the overall dynamics. Despite the significant effect that the stiffness and damping in the joint interfaces between the various components of the VAD may have on its overall dynamic performance, the joint compliance is usually neglected in the design process of VAD systems. In the presented substructure framework, the joint interfaces between VAD components are modelled and their damping and stiffness parameters are determined experimentally.

Although the design parameters of the VAD systems are tuned to maximize its dynamic response at the drill-tip, because of the manufacturing errors and un-modelled parameters such as joint stiffness and damping, the dynamic performance of the manufactured VAD system is usually sub-optimal. To enhance the performance of the manufactured VAD, the developed substructure analysis framework will be used for structural modification of the manufactured VAD by tuning its mechanical and electrical substructures.

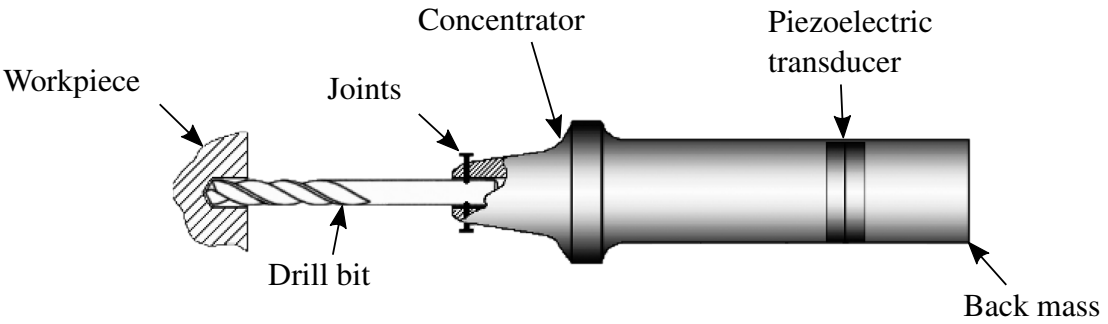

Fig. 1.6 Components of a VAD tool holder [3]

1.2 Contributions

The main contributions of this project are summarized as follows:

- A new electro-mechanical substructure analysis framework is presented to be used in designing axial and axial-torsional VAD systems with optimum dynamic performance
- The effect of damping and stiffness in the joints of the VAD system on its overall dynamics is considered in modeling
- The presented substructure analysis method is used for structural modification of the VAD system by adjusting the parameters of its mechanical as well as electrical components

1.3 Thesis organization

In Chapter 2, theoretical material required for modeling of substructures, coupling by RCSA and modeling of piezoelectric materials are discussed. Chapter 3 contains step-by-step coupling of substructures for cases of axial and axial-torsional VAD tool holders. Chapter 4 is devoted to model updating, electric current formulation and structural modification. The effect of changing drill bit overhang and active structural modification through electric circuit adjustment are studied.

Chapter 2

Background Theory

2.1 Introduction

In this chapter, the concept of Receptance Coupling Substructure Analysis (RCSA), which refers to coupling the dynamics of individual components to predict the dynamic response of the assembled system, is introduced. A VAD system is an assembly of several mechanical and electro-mechanical components. The RCSA method will be used in the next chapter to couple the receptances of the individual components to predict the overall response of the VAD systems at the drill tip.

Based on the geometry of tool holder components, different methods are used for computing their Frequency Response Functions (FRF). Modeling through continuous system theory and finite element methods are explained.

The last part of the chapter is about introducing piezoelectric materials, their constitutive equations, and presenting a model for the piezoelectric transducer. The model is based on a mechanical perspective.

2.2 Coupling substructures by RCSA

2.2.1 Axial receptance coupling

The aim of using RCSA method is to predict the FRF of a multi-component system by coupling the FRFs of their individual components [22].

The simplest case of substructure coupling is for rigid coupling of two substructures in one direction.

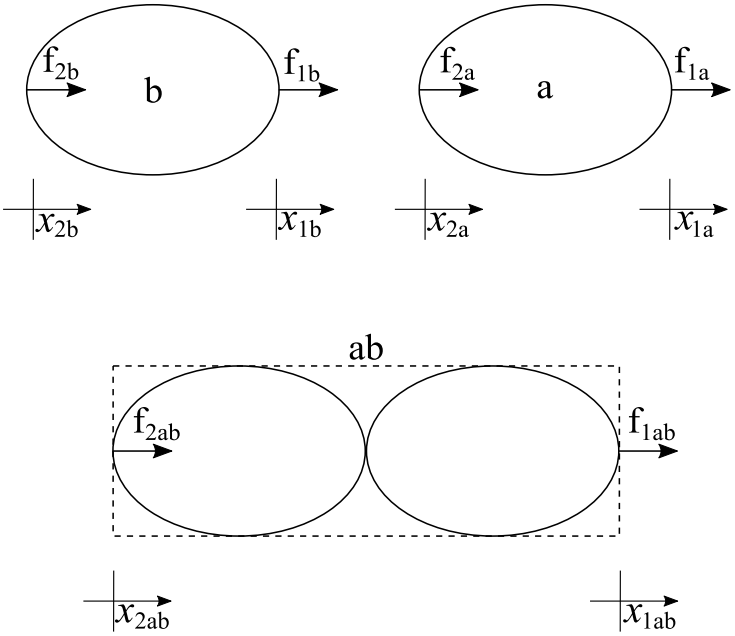

Fig. 2.1 Axial coupling of substructures a and b.

Consider the general structure ab consisting of two substructures, a and b, connected rigidly in one end as shown in Fig.2.1. Each substructure is characterized by two Degrees-Of-Freedom (DOF) (x_{1i} and x_{2i}, $i = a,b$). The receptance FRF of the individual substructures map the displacement responses at their two DOFs to the dynamic forces applied on them, as follows:

$$\left\{ \begin{array}{c} x_{1a}(\omega) \\ x_{2a}(\omega) \end{array} \right\} = \left[\begin{array}{cc} h_{1a1a}(\omega) & h_{1a2a}(\omega) \\ h_{2a1a}(\omega) & h_{2a2a}(\omega) \end{array} \right] \left\{ \begin{array}{c} f_{1a}(\omega) \\ f_{2a}(\omega) \end{array} \right\} \tag{2.1}$$

$$\left\{ \begin{array}{c} x_{1b}(\omega) \\ x_{2b}(\omega) \end{array} \right\} = \left[\begin{array}{cc} h_{1b1b}(\omega) & h_{1b2b}(\omega) \\ h_{2b1b}(\omega) & h_{2b2b}(\omega) \end{array} \right] \left\{ \begin{array}{c} f_{1b}(\omega) \\ f_{2b}(\omega) \end{array} \right\} \tag{2.2}$$

where $f_i(\omega)$ and $x_i(\omega)$, $i = 1a,2a,1b,2b$, are the forces applied at the DOF i, and the corresponding displacements, respectively. Each receptance $h_{ij}(\omega)$ is a complex-valued

function of frequency (ω) that maps the displacement at DOF i to the force at the DOF j. Similarly, the receptance FRFs of the assembled system, ab, maps the displacement response at its DOFs (i.e. $1ab, 2ab$) to the forces applied on them, as follows:

$$\left\{ \begin{array}{c} x_{1ab}(\omega) \\ x_{2ab}(\omega) \end{array} \right\} = \left[\begin{array}{cc} h_{1ab1ab}(\omega) & h_{1ab2ab}(\omega) \\ h_{2ab1ab}(\omega) & h_{2ab2ab}(\omega) \end{array} \right] \left\{ \begin{array}{c} f_{1ab}(\omega) \\ f_{2ab}(\omega) \end{array} \right\} \tag{2.3}$$

The force and displacement in the real world are real-valued and functions of time which can be converted to the frequency domain using the following Fourier transform

$$f_j(\omega) = \frac{1}{\sqrt{2\pi}} \int_{-\infty}^{+\infty} \hat{f}_j(t) e^{-i\omega t} dt \tag{2.4}$$

$$x_j(\omega) = \frac{1}{\sqrt{2\pi}} \int_{-\infty}^{+\infty} \hat{x}_j(t) e^{-i\omega t} dt \tag{2.5}$$

Where $\hat{f}_j(t)$ and $\hat{x}_j(t)$ are force and displacement corresponding to DOF j in time domain, respectively. Note that all of the displacement, force, and FRF parameters in this chapter are functions of frequency, which is omitted from notations for simplicity.

Substructure FRFs can be determined by a theoretical model or experimental measurement, and the objective in RCSA is to determine the receptance FRFs of the assembly ab in terms of the receptance FRFs of its substructure.

The compatibility of displacements in Fig.2.1, requires the same physical displacements for the coupling points of $2a$ and $1b$, as written below

$$x_{2a} = x_{1b} \tag{2.6}$$

In addition to the compatibility of displacements at the coupling point, the force equilibrium at this point also requires the following:

$$f_{2a} + f_{1b} = 0 \tag{2.7}$$

By applying the defined compatibility and equilibrium conditions, the direct (h_{1ab1ab} and h_{2ab2ab}) and cross (h_{1ab2ab} and h_{2ab1ab}) FRFs of the system (ab) are computed from the FRFs of the individual components, as follows:

$$h_{1ab1ab} = h_{1a1a} - h_{1a2a}(h_{2a2a} + h_{1b1b})^{-1} h_{2a1a} \tag{2.8}$$

$$h_{1ab2ab} = h_{1a2a}(h_{2a2a} + h_{1b1b})^{-1} h_{1b2b} \tag{2.9}$$

$$h_{2ab1ab} = h_{2b1b}(h_{1b1b} + h_{2a2a})^{-1} h_{2a1a} \tag{2.10}$$

$$h_{2ab2ab} = h_{2b2b} - h_{2b1b}(h_{1b1b} + h_{2a2a})^{-1} h_{1b2b} \tag{2.11}$$

The detailed derivations of applying compatibility and equilibrium conditions to obtain equations 2.8 to 2.11 is provided in Appendix A.

2.2.2 Axial-torsional receptance coupling

As will be described in the next chapter, both the axial and torsional deflections of the substructures of VAD systems are coupled. Therefore, substructure coupling formulation should be extended to consider the simultaneous coupling of the axial and torsional DOFs. [21].

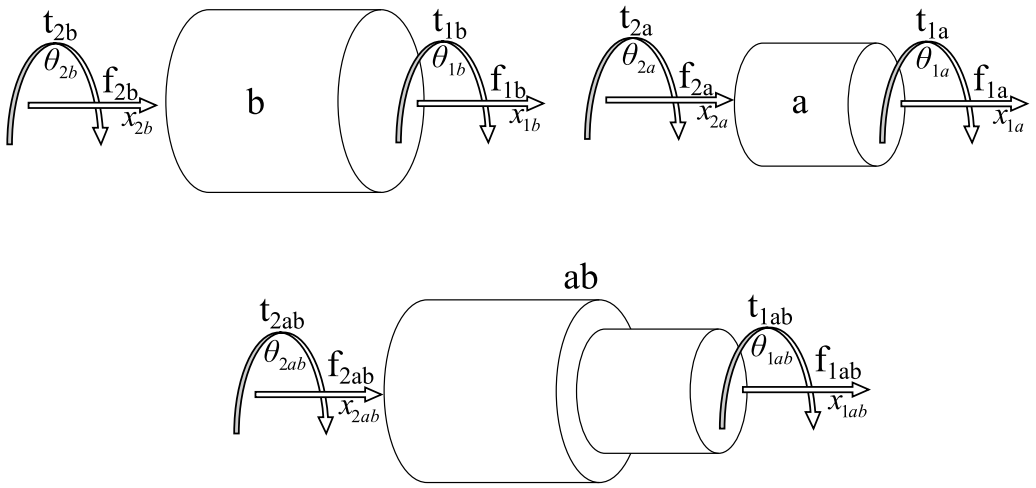

Fig. 2.2 Axial-torsional coupling of subsystems a and b

In Fig.2.2, x_i represents axial displacement, θ_i torsional displacement, f_i axial force, and t_i torsional torque at DOF i, where $i = 1a, 2a, 1b$, and $2b$. All of these parameters are scalar functions of frequency (ω).

In axial-torsional coupling, defining displacement and force in a vector form will simplify RCSA formulations. Displacement and force vectors are defined as follows:

$$\{X_i\} = \begin{Bmatrix} x_i \\ \theta_i \end{Bmatrix}; \{F_j\} = \begin{Bmatrix} f_j \\ t_j \end{Bmatrix} \tag{2.12}$$

where i, j are $1a, 2a$ for subsystem a, $1b, 2b$ for subsystem b, and $1ab, 2ab$ for the assembled system ab. The receptance FRF matrix, mapping the displacement vector at DOF i to the force vector at DOF j, is denoted by $[H_{ij}]$ and defined as follow:

$$\begin{Bmatrix} x_i \\ \theta_i \end{Bmatrix} = \begin{bmatrix} h_{ij}^{xf} & h_{ij}^{xt} \\ h_{ij}^{\theta f} & h_{ij}^{\theta t} \end{bmatrix} \begin{Bmatrix} f_j \\ t_j \end{Bmatrix} \rightarrow \{X_i\} = \left[H_{ij}\right] \left\{F_j\right\} \tag{2.13}$$

The FRFs written in lower-case letters represent scalar functions of frequency. The h_{ij}^{xf} stands for the frequency response of the axial displacement x_i to the excitation force f_j, h_{ij}^{xt} for

the frequency response of the axial displacement x_i to the excitation torque t_j, $h_{ij}^{\theta f}$ for the frequency response of torsional displacement θ_i to the excitation force f_j, and $h_{ij}^{\theta t}$ for the frequency response of the torsional displacement θ_i to the excitation torque t_j.

For the sake of simplicity, curly and square brackets are omitted from the notations, so the capital-uppercase letter notations of X_i, F_j and H_{ij} are considered for the displacement vector of DOF i, the force vector of DOF j and the 2×2 FRF matrix mapping them, respectively.

The FRF matrices of subsystems a and b in the vector-form notation are as follows:

$$\left\{ \begin{array}{c} X_{1a} \\ X_{2a} \end{array} \right\} = \left[\begin{array}{cc} H_{1a1a} & H_{1a2a} \\ H_{2a1a} & H_{2a2a} \end{array} \right] \left\{ \begin{array}{c} F_{1a} \\ F_{2a} \end{array} \right\} \tag{2.14}$$

$$\left\{ \begin{array}{c} X_{1b} \\ X_{2b} \end{array} \right\} = \left[\begin{array}{cc} H_{1b1b} & H_{1b2b} \\ H_{2b1b} & H_{2b2b} \end{array} \right] \left\{ \begin{array}{c} F_{1b} \\ F_{2b} \end{array} \right\} \tag{2.15}$$

And similarly for the FRF matrix of the assembled system ab:

$$\left\{ \begin{array}{c} X_{1ab} \\ X_{2ab} \end{array} \right\} = \left[\begin{array}{cc} H_{1ab1ab} & H_{1ab2ab} \\ H_{2ab1ab} & H_{2ab2ab} \end{array} \right] \left\{ \begin{array}{c} F_{1ab} \\ F_{2ab} \end{array} \right\} \tag{2.16}$$

In the axial-torsional coupling of subsystems a and b in Fig.2.2, the compatibility condition is defined by the same displacement vector for the coupling points of $2a$ and $1b$, as written below

$$X_{2a} = X_{1b} \tag{2.17}$$

The equilibrium condition leads to the following equation for the force vectors at the coupling point:

$$F_{2a} + F_{1b} = 0 \tag{2.18}$$

By applying the defined compatibility and equilibrium conditions, the direct (H_{1ab1ab} and H_{2ab2ab}) and cross (H_{1ab2ab} and H_{2ab1ab}) FRFs of the system ab are computed from the FRFs of the individual components, as follows:

$$H_{1ab1ab} = H_{1a1a} - H_{1a2a}(H_{2a2a} + H_{1b1b})^{-1} H_{2a1a} \tag{2.19}$$

$$H_{1ab2ab} = H_{1a2a}(H_{2a2a} + H_{1b1b})^{-1} H_{1b2b} \tag{2.20}$$

$$H_{2ab1ab} = H_{2b1b}(H_{1b1b} + H_{2a2a})^{-1} H_{2a1a} \tag{2.21}$$

$$H_{2ab2ab} = H_{2b2b} - H_{2b1b}(H_{1b1b} + H_{2a2a})^{-1} H_{1b2b} \tag{2.22}$$

The FRF matrix of the system *ab* defined in Eq.2.16 is now obtained from the FRF matrices of individual components and is written below:

$$
\begin{aligned}
H_{ab} &= \begin{bmatrix} H_{1ab1ab} & H_{1ab2ab} \\ H_{2ab1ab} & H_{2ab2ab} \end{bmatrix}_{4\times 4} \\
&= \begin{bmatrix} H_{1a1a} - H_{1a2a}(H_{2a2a} + H_{1b1b})^{-1} H_{2a1a} & H_{1a2a}(H_{2a2a} + H_{1b1b})^{-1} H_{1b2b} \\ H_{2b1b}(H_{1b1b} + H_{2a2a})^{-1} H_{2a1a} & H_{2b2b} - H_{2b1b}(H_{1b1b} + H_{2a2a})^{-1} H_{1b2b} \end{bmatrix}_{4\times 4}
\end{aligned}
\tag{2.23}
$$

The detailed derivations of applying compatibility and equilibrium conditions to obtain the FRF matrix of system *ab* is provided in Appendix A.

2.3 Theoretical modeling of substructures

In the preceding section, it was assumed that direct and cross FRFs of each substructure are available. In this section, theoretical models are introduced for modeling the substructures and computing their FRFs. Modeling cylindrical components through an analytical approach is presented in Section 2.3.1. Modeling through a numerical approach using the finite element method is also considered in Section 2.3.2.

2.3.1 Axial and torsional modeling of cylindrical components

Modeling of circular rod through an analytical solution is considered in this section [18] . In order to model a rod for axial vibrations, let's consider the elastic rod with the length of l, Young's modulus of E, density of ρ and cross-section area of A as shown in Fig.2.3.

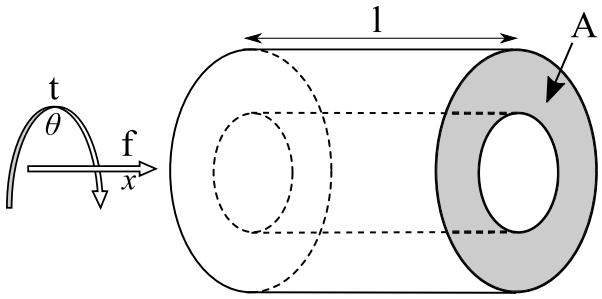

Fig. 2.3 Vibration of a rod as a continuous system

The partial differential equation describing axial vibrations of a rod is [18]

$$EA\frac{\partial^2 u}{\partial x^2}(x,t) = \rho A\frac{\partial^2 u}{\partial t^2}(x,t) \tag{2.24}$$

where u is axial displacement of the location x. Solving this partial-differential equation requires boundary conditions determined. By applying the free-free boundary conditions of

$$\frac{\partial u}{\partial x}(0,t) = 0; \frac{\partial u}{\partial x}(l,t) = 0 \tag{2.25}$$

The natural frequency of the n^{th} mode is computed from the equation below

$$\omega_n = \frac{n\pi\sqrt{\frac{E}{\rho}}}{l} \tag{2.26}$$

and the mode shape of the corresponding mode from the relation below

$$U_n(x) = C_n \cos \frac{n\pi x}{l} \tag{2.27}$$

Mode shape can be scaled by any arbitrary coefficient. The mass-normalized mode shape is the one which should be used in FRF computation. The modal mass of the n^{th} mode is computed using the following equation

$$m_n^a = \int_0^l \rho(x) A(x) U_n^2(x) dx \tag{2.28}$$

where m_n^a is the modal mass of the n^{th} axial mode. The modal mass corresponding to n^{th} mode shape will be computed by substituting Eq.2.27 in Eq.2.28

$$m_n^a = \int_0^l \rho(x) A(x) C_n^2 \cos^2(\frac{\pi n x}{l}) dx = \rho A C_n^2 \int_0^l \cos^2(\frac{\pi n x}{l}) dx = \frac{1}{2} \rho A C_n^2 \int_0^l [1 + \cos(\frac{2\pi n x}{l})] dx \tag{2.29}$$

For the rigid body mode where $n = 0$, the modal mass is

$$m_0^a = \frac{1}{2} \rho A C_0^2 \int_0^l [1 + \cos(0)] dx = \rho A C_0^2 l \tag{2.30}$$

By setting $m_0^a = 1$, the normalized mode shape corresponding to rigid body mode is found

$$U_0(x) = \frac{1}{\sqrt{\rho A l}} \tag{2.31}$$

For flexible modes where n is non-zero, the modal mass is

$$m_n^a = \frac{1}{2} \rho A C_n^2 \int_0^l [1 + \cos(\frac{2\pi n x}{l})] dx = \frac{1}{2} \rho A C_n^2 l \tag{2.32}$$

By setting the modal mass to be 1, the normalized mode shape corresponding to mode $n (n \neq 0)$ is found as below

$$U_n(x) = \sqrt{\frac{2}{\rho A l}} \cos \frac{n\pi x}{l} \tag{2.33}$$

The axial FRF between points x_i and x_j will be computed using the following equation

$$h_{ij}^{xf}(x_i,x_j,\omega) = \sum_{n=0}^{Nm} \frac{U_n(x_i)U_n(x_j)}{-\omega^2+\omega_n^2} \tag{2.34}$$

In order to model a rod for torsional vibrations, consider the same elastic rod in Fig.2.3 with the length of l, modulus of rigidity of G, the density of ρ and polar moment of inertia of J.

The partial differential equation describing torsional vibrations of the rod is

$$GJ\frac{\partial^2\theta}{\partial x^2}(x,t) = I_0\frac{\partial^2\theta}{\partial t^2}(x,t) \tag{2.35}$$

where $I_0 = \rho J$ and θ is torsional displacement of the location x. By applying the free-free boundary conditions of

$$\frac{\partial\theta}{\partial x}(0,t) = 0; \frac{\partial\theta}{\partial x}(l,t) = 0 \tag{2.36}$$

The natural frequency of the n^{th} mode is computed from the equation below

$$\omega_n = \frac{n\pi\sqrt{\frac{G}{\rho}}}{l} \tag{2.37}$$

and the mode shape of the corresponding mode from the relation below

$$\Theta(x) = C_n\cos(\frac{\pi nx}{l}) \tag{2.38}$$

Mode shape can be scaled by any arbitrary coefficient. The mass-normalized mode shape is the one which should be used in FRF computation. The modal mass of the n^{th} mode is computed using the following equation

$$m_n^t = \int_0^l \rho(x)J(x)U_n^2(x)dx \tag{2.39}$$

where m_n^t stands for modal mass of the n^{th} torsional mode. The modal mass corresponding to n^{th} mode shape will be computed by substituting Eq.2.27 in Eq.2.39

$$m_n^t = \int_0^l \rho(x)J(x)C_n^2\cos^2(\frac{\pi nx}{l})dx = \rho JC_n^2\int_0^l \cos^2(\frac{\pi nx}{l})dx = \frac{1}{2}\rho JC_n^2\int_0^l [1+\cos(\frac{2\pi nx}{l})]dx \tag{2.40}$$

For the rigid body mode where $n = 0$, the modal mass is

$$m_0^t = \frac{1}{2}\rho J C_0^2 \int_0^l [1+\cos(0)]dx = \rho J C_0^2 l \tag{2.41}$$

By setting $m_0^t = 1$, the normalized mode shape corresponding to rigid body mode is found

$$\Theta_0(x) = \frac{1}{\sqrt{\rho J l}} \tag{2.42}$$

For flexible modes where n is non-zero, the modal mass is

$$m_n^t = \frac{1}{2}\rho J C_n^2 \int_0^l [1+\cos(\frac{2\pi n x}{l})]dx = \frac{1}{2}\rho J C_n^2 l \tag{2.43}$$

By setting the modal mass to be 1, the normalized mode shape corresponding to mode n is found as below

$$\Theta_n(x) = \sqrt{\frac{2}{\rho J l}}\cos(\frac{\pi n x}{l}) \tag{2.44}$$

The torsional FRF between points x_i and x_j will be computed using the following equation

$$h_{ij}^{\theta t}(x_i, x_j, \omega) = \sum_{n=0}^{Nm} \frac{\Theta_n(x_i)\Theta_n(x_j)}{-\omega^2 + \omega_n^2} \tag{2.45}$$

Finally, the FRF matrix including axial and torsional FRFs between the two ends a rod component, where x_i and x_j are corresponding to $x = 0$ and $x = l$ respectively, will be obtained as follow

$$H_r = \begin{bmatrix} H_{1r1r} & H_{1r2r} \\ H_{2r1r} & H_{2r2r} \end{bmatrix} = \begin{bmatrix} h_{1r1r}^{xf}(0,0,\omega) & 0 & h_{1r2r}^{xf}(0,l,\omega) & 0 \\ 0 & h_{1r1r}^{\theta t}(0,0,\omega) & 0 & h_{1r2r}^{\theta t}(0,l,\omega) \\ h_{2r1r}^{xf}(l,0,\omega) & 0 & h_{2r2r}^{xf}(l,l,\omega) & 0 \\ 0 & h_{2r1r}^{\theta t}(l,0,\omega) & 0 & h_{2r2r}^{\theta t}(l,l,\omega) \end{bmatrix} \tag{2.46}$$

2.3.2 Axial and torsional modeling using finite element method

Axial-torsional disk element

Finite element method is commonly used in cases of complex geometries. In this work, rod elements [18] are used to model the dynamics of conical parts. Figure 2.4 shows a rod element with axial and torsional flexibility.

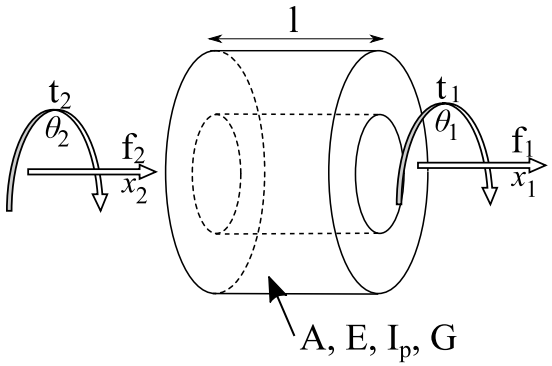

Fig. 2.4 Axial-torsional rod (disk) element

In this simple cylinder geometry, axial and torsional modes are uncoupled. Therefore, by considering a linear shape function for the axial deformation, the following mass and stiffness matrices will be obtained when the element displacement vector is defined as $\{u^a\} = [x_1, x_2]^T$.

$$[m^a] = \frac{\rho A l}{6}\begin{bmatrix} 2 & 1 \\ 1 & 2 \end{bmatrix}; [k^a] = \frac{EA}{l}\begin{bmatrix} 1 & -1 \\ -1 & 1 \end{bmatrix} \tag{2.47}$$

Considering a linear shape function for the torsional deformation will lead to the computation of mass and stiffness matrices for torsional displacement vector of $\{u^t\} = [\theta_1, \theta_2]^T$.

$$[m^t] = \frac{\rho I_p l}{6}\begin{bmatrix} 2 & 1 \\ 1 & 2 \end{bmatrix}; [k^t] = \frac{GJ}{l}\begin{bmatrix} 1 & -1 \\ -1 & 1 \end{bmatrix} \tag{2.48}$$

Although in the case of simple cylinder, shown in Fig,2.4, there is no coupling between axial and torsional modes of vibration, they should be considered together. This is necessary for the case of axial-torsional coupling. The mass matrix of the element considering axial and

torsional degrees of freedom at the same time will become in the following form

$$[m] = \frac{\rho l}{6} \begin{bmatrix} 2A & 0 & A & 0 \\ 0 & 2I_p & 0 & I_p \\ A & 0 & 2A & 0 \\ 0 & I_p & 0 & 2I_p \end{bmatrix} \tag{2.49}$$

Which is written by considering that the element displacement vector is $\{u\} = [x_1, \theta_1, x_2, \theta_2]^T$. The stiffness matrix of the axial-torsional displacement vector is

$$[k] = \frac{1}{l} \begin{bmatrix} EA & 0 & -EA & 0 \\ 0 & GJ & 0 & -GJ \\ -EA & 0 & EA & 0 \\ 0 & -GJ & 0 & GJ \end{bmatrix} \tag{2.50}$$

As can be seen in Eq.2.49 and Eq.2.50, half of matrix elements are zero which is due to decoupling of axial and torsional modes of the simple cylinder.

Drill bit element

Due to the pre-twisted geometry of the drill bit, its axial and torsional deflections are coupled, which is a different case than the rod element shown in Fig.2.4. As can be seen in Fig.2.5, when an axial force is applied to the drill bit element, axial and torsional deformations happen at the same time. The same happens when a torsional torque is applied to the element.

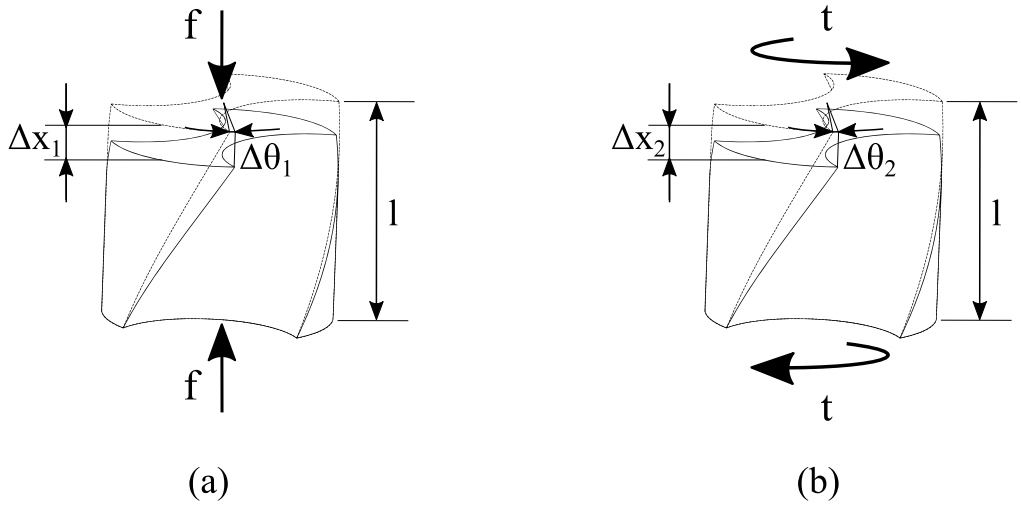

Fig. 2.5 Deformations of a drill bit element under a) an axial force b) a torsional torque

In the case of a drill bit, the cross section rotates continuously with respect to the longitudinal axis. The twisted geometry of the drill bit creates a coupling between its axial and torsional deformations. In this work, Rosen's model [19] of the coupled nonlinear deflection of pre-twisted bars is used to describe the dynamics of the drill-bit. Assuming that the total deformation of the pre-twisted bar is a superposition of Saint-Venant torsion and an axial motion of each cross-section, Rosen developed the following equation to describe the relationship between the applied force and torque and the resulting axial and torsional deformations:

$$f = EA\varepsilon + ES\varphi + \frac{1}{2}EI_p\varphi^2 \tag{2.51}$$

$$t = ES\varepsilon + (GJ_s + EK)\varphi + EI_p\varepsilon\varphi + \frac{3}{2}ED\varphi^2 + \frac{1}{2}EF\varphi^3 \tag{2.52}$$

Where f stands for axial force, t for torsional torque, ε for axial strain, φ for change in torsional displacement per unit length , E for modulus of elasticity, G for modulus of rigidity, A for cross section area ,I_p for polar moment of inertia of the cross section, S, J_s, K, D and F for section integrals which depends on wrapping function of the cross section[19].

Jin and Koya [9] showed that, for typical drill-bit deflections, the values of the nonlinear terms are less than 1% of the linear terms. Therefore, the effect of the nonlinear terms can be neglected which leads to the following linear equations:

$$f = EA\varepsilon + ES\varphi \tag{2.53}$$

$$t = ES\varepsilon + (GJ_s + EK)\varphi \tag{2.54}$$

The assumptions made in Rosen's work [19] require a uniform axial strain (ε) and twist per unit length (φ). As a result, the deformation of a drill bit element with the length l, the case shown in Fig.2.5, the variables ε and φ are computed as follows:

$$\varepsilon = \frac{\Delta x}{l}; \varphi = \frac{\Delta\theta}{l} \tag{2.55}$$

By substituting these values in Eq.2.53 and Eq.2.54, the following relations are obtained:

$$f = \frac{EA}{l}\Delta x + \frac{ES}{l}\Delta\theta \tag{2.56}$$

$$t = \frac{ES}{l}\Delta x + (\frac{GJ_s + EK}{l})\Delta\theta \tag{2.57}$$

Equations 2.56 and 2.57 illustrate that the drill bit element can be approximated with a linear axial-torsional spring. The stiffness coefficients of this spring are $k^{xf} = EA/l$, $k^{\theta f} = ES/l$,

$k^{xt} = ES/l$ and $k^{\theta t} = (GJ_s + EK)/l$ which are proportional to the modulus of elasticity E and inversely proportional to the element length l. This statement can be written in the following form for the drill bit element in Fig.2.5:

$$f = k^{xf}\Delta x + k^{\theta f}\Delta\theta \tag{2.58}$$

$$t = k^{xt}\Delta x + k^{\theta t}\Delta\theta \tag{2.59}$$

Various methods have been used in the literature to determine the section integral parameters, S, J_s, K, D and F, and subsequently the stiffness parameters. For example, a numerical method based on a 2D FE solution was used in [9]. In this work, a curve-fitting method is used to obtain relations for the stiffness coefficients. A drill bit element is modeled in the commercial finite element software COMSOL Multiphysics. The stiffness coefficients are obtained by applying axial force and torsional torque to the element and measuring the deformations.

From the case *a* in Fig.2.5 where only axial force is applied and no torque is applied, the following equations are obtained:

$$f = k^{xf}\Delta x_1 + k^{\theta f}\Delta\theta_1 \tag{2.60}$$

$$0 = k^{xt}\Delta x_1 + k^{\theta t}\Delta\theta_1 \tag{2.61}$$

and from the case *b* shown in Fig.2.5 where only torsional torque is applied and no force is applied, the following equations are obtained:

$$0 = k^{xf}\Delta x_2 + k^{\theta f}\Delta\theta_2 \tag{2.62}$$

$$t = k^{xt}\Delta x_2 + k^{\theta t}\Delta\theta_2 \tag{2.63}$$

By solving Eq.2.60 to Eq.2.63, the values of stiffness coefficients of k^{xf}, $k^{\theta f}$, k^{xt} and $k^{\theta t}$ will be determined. These stiffness coefficients are computed for a specific dimension of the drill bit. To make the model general for all diameters of typical drill bits, this process is repeated for a few different diameters and corresponding stiffness coefficients are collected. Each data set of these stiffness coefficients is approximated by a cubic polynomial:

$$\begin{aligned}
k^{xf} &= 765.6d^3 + 1.125\times10^5 d^2 + 1.49910^5 d - 3.089\times10^5 \\
k^{\theta f} &= 13.38d^3 + 0.8516d^2 - 0.6822d - 4.749 \\
k^{xt} &= 14.75d^3 - 30.09d^2 + 213d - 432.7 \\
k^{\theta t} &= 0.1071d^3 - 1.209d^2 + 5.622d - 8.954
\end{aligned} \tag{2.64}$$

where d is drill bit diameter in mm. This relations are obtained for typical types of drill bit available in the market with 30 degrees of helix angle, so the relations are only functions of the drill bit diameter. The cubic polynomials are plotted versus the data points collected from the finite element software (which are shown by the star signs) in the following figures:

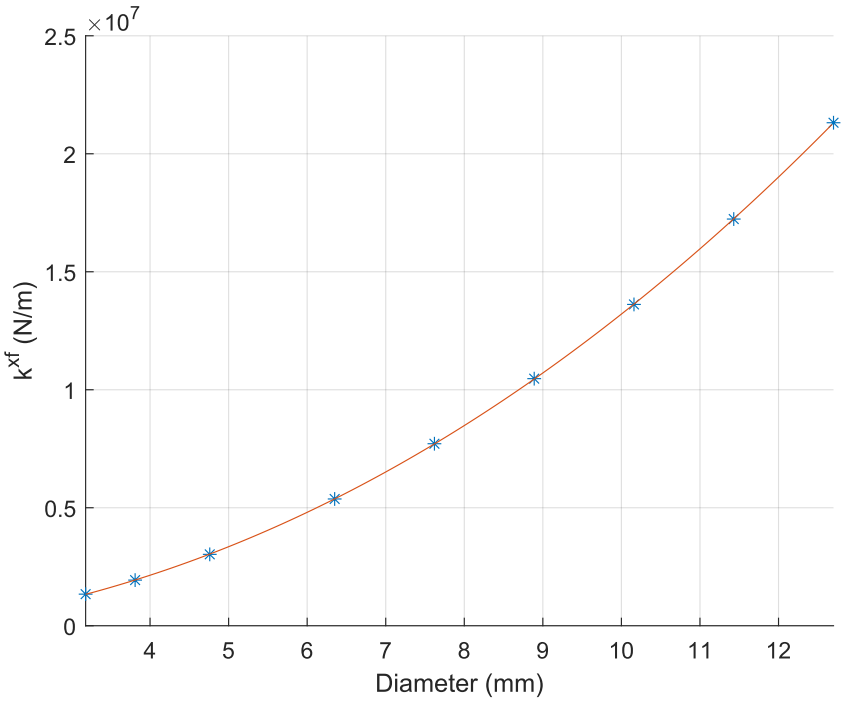

Fig. 2.6 Cubic polynomial of k^{xf} and data points

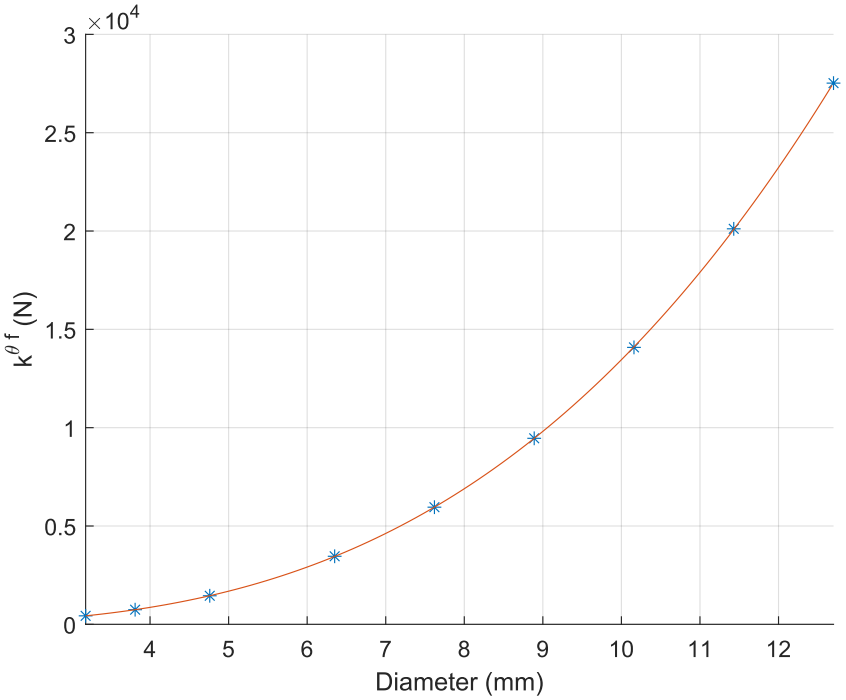

Fig. 2.7 Cubic polynomial of $k^{\theta f}$ and data points

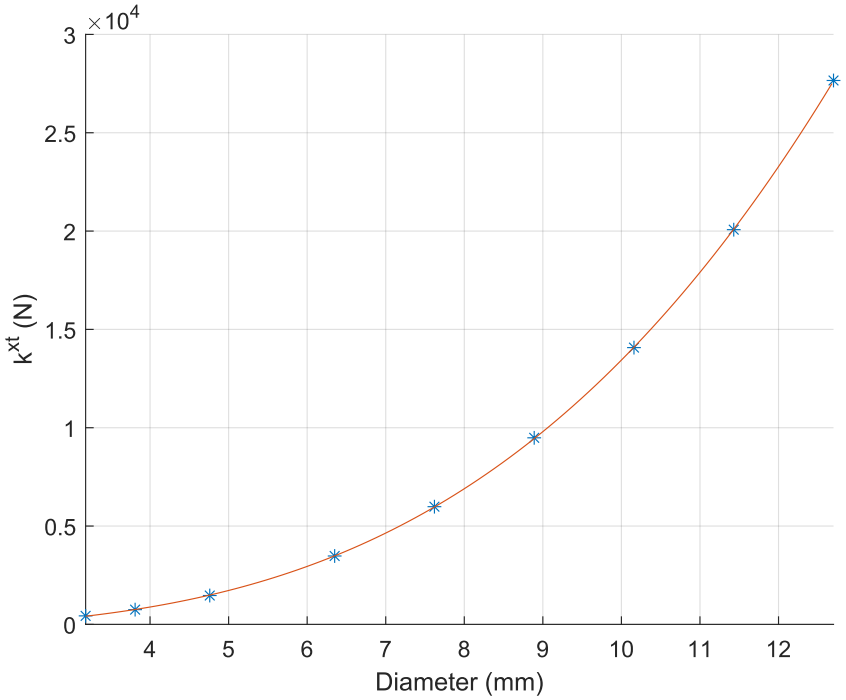

Fig. 2.8 Cubic polynomial of k^{xt} and data points

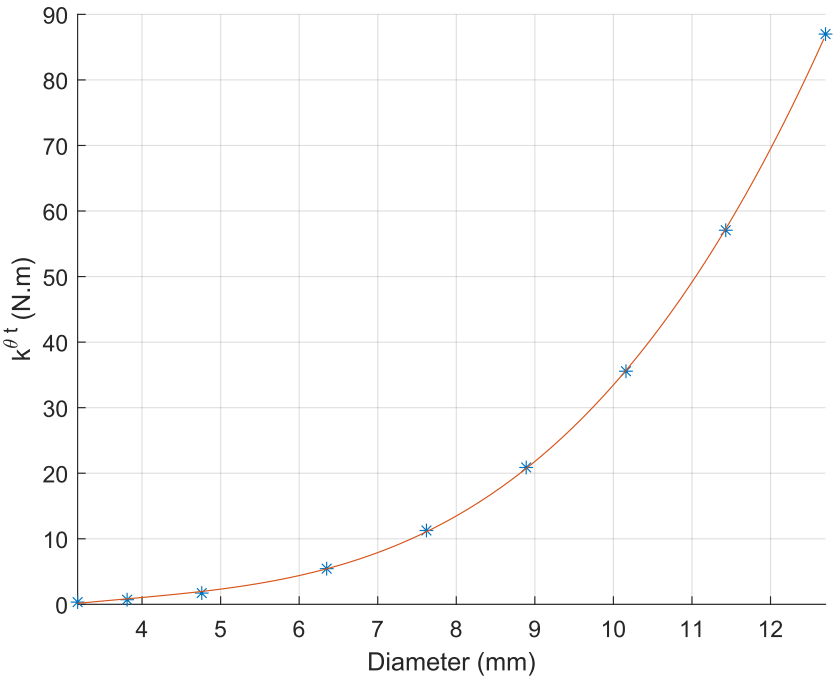

Fig. 2.9 Cubic polynomial of $k^{\theta t}$ and data points

Now that the stiffness coefficients are determined, the stiffness matrix of the drill bit element is known. The material considered for obtaining the cubic polynomials is Tungsten Carbide with modulus of elasticity of E_{WC} and for a unit length of the element. As mentioned before, the stiffness coefficients are proportional to the modulus of elasticity E and inversely proportional to the element length l. Therefore, the stiffness matrix for a material with the modulus of elasticity of $\hat{E}$ and the element length of l, will be as follow:

$$[k] = \frac{\hat{E}}{lE_{WC}} \begin{bmatrix} k^{xf} & k^{\theta f} & -k^{xf} & -k^{\theta f} \\ k^{xt} & k^{\theta t} & -k^{xt} & -k^{\theta t} \\ -k^{xf} & -k^{\theta f} & k^{xf} & k^{\theta f} \\ -k^{xt} & -k^{\theta t} & k^{xt} & k^{\theta t} \end{bmatrix} \tag{2.65}$$

The mass matrix of the drill bit element is as follow:

$$[m] = \begin{bmatrix} \frac{m}{3} & 0 & \frac{m}{6} & 0 \\ 0 & \frac{I}{3} & 0 & \frac{I}{6} \\ \frac{m}{6} & 0 & \frac{m}{3} & 0 \\ 0 & \frac{I}{6} & 0 & \frac{I}{3} \end{bmatrix} \tag{2.66}$$

where m and I are mass and inertia of the element, respectively.

Equations of motion of the complete system of finite elements

So far, the mass and stiffness matrices of either rod element or drill bit element are for one element in the local coordinate system. The global mass and stiffness matrices of a body which is the assemblage of N_e number of elements will be a $(2N_e+2)\times(2N_e+2)$ matrix. The global mass matrix is computed using following equation

$$[M] = \sum_{e=1}^{N_e} [A_e]^T [m][A_e] \tag{2.67}$$

And the global stiffness matrix using the following equation

$$[K] = \sum_{e=1}^{N_e} [A_e]^T [k][A_e] \tag{2.68}$$

where $[A_e]$ is a $4\times(2N_e+2)$ matrix which has all zero elements except a unity matrix $[I]_{4\times4}$ is replaced for the elements between the columns $2e-1$ and $2e+2$.

The equation describing free vibration of the body is

$$[M]\{\ddot{x}\} + [K]\{x\} = 0 \tag{2.69}$$

This equation can also written in an alternative form as written below

$$[-\omega^2[I] + [M]^{-1}[K]]\{x\} = 0 \tag{2.70}$$

which is in physical domain and includes $(2N_e+2)$ dependent equations. This coupling between equations come from the matrix $[M]^{-1}[K]$. Using eigenvalue decomposition for this matrix will provide matrices of natural frequencies and mode shapes.

$$[\Lambda] = \begin{bmatrix} \omega_1^2 & 0 & \cdots & 0 \\ 0 & \omega_2^2 & \cdots & 0 \\ \vdots & \vdots & \ddots & \vdots \\ 0 & 0 & \dots & \omega_{(2N_e+2)}^2 \end{bmatrix} \tag{2.71}$$

$$[\Phi] = \begin{bmatrix} \{\phi_1\} & \{\phi_2\} & \cdots & \{\phi_{(2N_e+2)}\} \end{bmatrix} \tag{2.72}$$

and the matrix $[\Phi]$ is mass normalized i.e.

$$[\Phi]^T [M] [\Phi] = [I] \tag{2.73}$$

$$[\Phi]^T [K] [\Phi] = [\Lambda] \tag{2.74}$$

The FRF of the body can be computed using the following formula

$$h_{jk}(\omega) = \frac{x_j}{f_k} = \sum_{r=1}^{(2N_e+2)} \frac{\phi_{jr}\phi_{kr}}{\omega_r^2 - \omega^2} \tag{2.75}$$

where x_j stands for j^{th} degree of freedom, which is axial displacement in case of odd numbers and torsional displacement in case of even numbers of j, and f_k stands for a load on k^{th} degree of freedom, which is axial force in case of odd numbers and torsional torque in case of even numbers of k. The FRF matrix of this system will be

$$H_s = \begin{bmatrix} H_{1s1s} & H_{1s2s} \\ H_{2s1s} & H_{2s2s} \end{bmatrix} = \begin{bmatrix} h_{1,1}(\omega) & h_{1,2}(\omega) & h_{1,(2N_e+1)}(\omega) & h_{1,(2N_e+2)}(\omega) \\ h_{2,1}(\omega) & h_{2,2}(\omega) & h_{2,(2N_e+1)}(\omega) & h_{2,(2N_e+2)}(\omega) \\ h_{(2N_e+1),1}(\omega) & h_{(2N_e+1),2}(\omega) & h_{(2N_e+1),(2N_e+1)}(\omega) & h_{(2N_e+1),(2N_e+2)}(\omega) \\ h_{(2N_e+2),1}(\omega) & h_{(2N_e+2),2}(\omega) & h_{(2N_e+2),(2N_e+1)}(\omega) & h_{(2N_e+2),(2N_e+2)}(\omega) \end{bmatrix} \tag{2.76}$$

2.4 Introduction to piezoelectric materials

A piezoelectric ceramic is made of specific crystals which are mostly oriented in the same direction through a process called poling process. Poling process refers to polarizing crystals in a high temperature condition under the effect of a strong electric field. A crystal structure of a piezoelectric ceramic, before and after polarization is depicted in Fig. 2.10.[15]

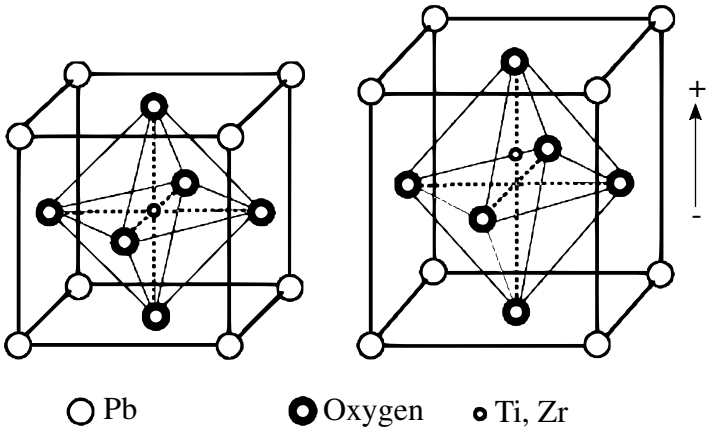

a) Before polarization b) After polarization

Fig. 2.10 Crystalline structure of a piezoelectric ceramic [15]

The constitutive equations describing the piezoelectric property are based on the assumption that the total strain in the transducer is the sum of mechanical strain by the mechanical stress and the strain caused by the applied electric field.

The describing electromechanical equations for the piezoelectric materials are given as follows [15]

$$\{\varepsilon_i\} = \left[S_{ij}^E\right]\{\sigma_j\} + [d_{mi}]\{E_m\} \tag{2.77}$$

$$\{D_m\} = [d_{im}]\{\sigma_i\} + [\xi_{ik}^{\sigma}]\{E_k\} \tag{2.78}$$

where $\{\varepsilon_i\} \in \Re^6$ stands for strain vector (m/m), $\{\sigma_j\} \in \Re^6$ for mechanical stress vector (N/m^2), $\{E_m\} \in \Re^3$ for vector of applied electric field (V/m), $\left[\xi_{ik}^{\sigma}\right] \in \Re^{3\times3}$ for permitivity (F/m) measured in a constant stress condition, $[d_{mi}] \in \Re^{6\times3}$ for matrix of piezoelectric strain constants (m/V), $\left[S_{ij}^E\right] \in \Re^{6\times6}$ for matrix of compliance coefficients (m^2/N) measured in a constant electric field condition, $\{D_m\} \in \Re^3$ for vector of electric displacement (C/m^2), and indexes $i, j = 1,2,...,6$ and $m,k = 1,2,3$ refer to different directions within the material coordinate system.

Equation 2.77 expresses the converse piezoelectric effect, which describes the situation when the device is being used as an actuator. Equation 2.78, on the other hand, expresses the

direct piezoelectric effect, which deals with the case when the transducer is being used as a sensor.

According to the constitutive relation of piezoelectric actuators in Eq.2.77, the deformation $\{\varepsilon_i\}$ is a linear combination of the deformation caused by mechanical stress and the additional deformation by the converse piezoelectric effect. In chapter 3, the piezoelectric transducer will be assumed to be a simple material with no piezoelectric effect. Instead, a pair of opposite mechanical forces denoted by F_{ext} will be considered as the converse piezoelectric effect.

These equations will be simplified as Eq.2.79 and Eq.2.80 for the transducer of the VAD tool holders. The reason for the simplification is that all stresses, stains and electrical fields are applied in the same axial direction.

$$\varepsilon = S^E \sigma + dE \tag{2.79}$$

$$D = d\sigma + \xi^\sigma E \tag{2.80}$$

In this stage, it is assumed that there is no electric field applied to the piezoelectric material meaning that E in Eq.2.79 is set to zero. What remains from the equation describes elasticity of a non-piezoelectric material with Young's modulus of $1/S^E$. According to the model presented for the rod using continuous system theory, a model for axial vibration of a rod considering the rigid-body and 1st longitudinal models for the piezoelectric transducer will be as follow

$$h_{ij}^{xf}(x_i,x_j,\omega) = \sum_{n=0}^{Nm} \frac{C_n^2 \cos(\frac{\pi n x_i}{l}) \cos(\frac{\pi n x_j}{l})}{-\omega^2+\omega_n^2} = \frac{1}{-\rho A l \omega^2} + \frac{C_1^2 \cos(\frac{\pi x_i}{l}) \cos(\frac{\pi x_j}{l})}{-\omega^2+\omega_1^2} \tag{2.81}$$

where $\omega_1 = \frac{\pi}{l}\sqrt{\frac{1}{\rho S^E}}$, $C_1 = \sqrt{\frac{2}{\rho A l}}$, ρ is piezoelectric density, S^E piezoelectric compliance, A and l are transducer cross-section area and thickness, respectively.

The transducer is assumed to be rigid in a torsional direction. Therefore, the FRF matrix only includes the torsional rigid-body mode.

$$h_{ij}^{\theta t}(x_i,x_j,\omega) = \sum_{n=0}^{Nm} \frac{C_n^2 \cos(\frac{\pi n x_i}{l}) \cos(\frac{\pi n x_j}{l})}{-\omega^2+\omega_n^2} = \frac{1}{-\rho J l \omega^2} \tag{2.82}$$

where J is polar moment of inertia of the transducer per unit length.

Axial direct and cross FRFs for the piezoelectric transducer are obtained as follows

$$h_{1p1p}^{xf} = h_{1p1p}^{xf}(0,0,\omega) = \frac{1}{-\rho A l \omega^2} + \frac{2}{-\rho A l \omega^2 + \frac{\pi^2 A}{l S^E}} \tag{2.83}$$

$$h^{xf}_{1p2p} = h^{xf}_{1p2p}(0,l,\omega) = \frac{1}{-\rho Al\omega^2} - \frac{2}{-\rho Al\omega^2 + \frac{\pi^2 A}{lS^E}} \tag{2.84}$$

$$h^{xf}_{2p1p} = h^{xf}_{2p1p}(l,0,\omega) = \frac{1}{-\rho Al\omega^2} - \frac{2}{-\rho Al\omega^2 + \frac{\pi^2 A}{lS^E}} \tag{2.85}$$

$$h^{xf}_{2p2p} = h^{xf}_{2p2p}(l,l,\omega) = \frac{1}{-\rho Al\omega^2} + \frac{2}{-\rho Al\omega^2 + \frac{\pi^2 A}{lS^E}} \tag{2.86}$$

where DOFs $1p$ and $2p$ refer to the DOFs at the two ends of the piezoelectric transducer. Writing the FRFs in a matrix form leads to the FRF matrix of the piezoelectric transducer in Eq.2.87. Since the transducer has a simple rod geometry, axial and torsional modes are independent which is the reason for the matrix to include several zero elements.

$$H_p = \begin{bmatrix} H_{1p1p} & H_{1p2p} \\ H_{2p1p} & H_{2p2p} \end{bmatrix} = \begin{bmatrix} h^{xf}_{1p1p} & 0 & h^{xf}_{1p2p} & 0 \\ 0 & h^{\theta t}_{1p1p} & 0 & h^{\theta t}_{1p2p} \\ h^{xf}_{2p1p} & 0 & h^{xf}_{2p2p} & 0 \\ 0 & h^{\theta t}_{2p1p} & 0 & h^{\theta t}_{2p2p} \end{bmatrix} \tag{2.87}$$

The transducer only generates axial vibrations. Axial displacements of the piezoelectric transducer have the following relations with mechanical forces

$$x_{1p} = h^{xf}_{1p1p} f_{1p} + h^{xf}_{1p2p} f_{2p} \tag{2.88}$$

$$x_{2p} = h^{xf}_{2p1p} f_{1p} + h^{xf}_{2p2p} f_{2p} \tag{2.89}$$

The deformation caused by mechanical forces is the difference between the two axial degrees of freedom of the transducer:

$$x_{1p} - x_{2p} = (h^{xf}_{1p1p} - h^{xf}_{2p1p}) f_{1p} + (h^{xf}_{1p2p} - h^{xf}_{2p2p}) f_{2p}$$

$$= \frac{4}{-\rho Al\omega^2 + \frac{\pi^2 A}{lS^E}} f_{1p} - \frac{4}{-\rho Al\omega^2 + \frac{\pi^2 A}{lS^E}} f_{2p} = \frac{4}{-\rho Al\omega^2 + \frac{\pi^2 A}{lS^E}} (f_{1p} - f_{2p}) \tag{2.90}$$

According to the constitutive equation of converse piezoelectric effect presented in Eq.2.79, the total deformation of a piezoelectric material is superposition of the deformations caused by mechanical forces and electric field. Involving the effect of electric field in the deformation of the transducer, the total deformation becomes

$$x_{1p} - x_{2p} = \frac{4}{-\rho Al\omega^2 + \frac{\pi^2 A}{lS^E}} (f_{1p} - f_{2p}) + d\frac{V}{l} l \tag{2.91}$$

As mentioned before, in coupling substructures by RCSA, the transducer will be consider as a simple material with no piezoelectric property. The converse piezoelectric effect will be considered as a pair of opposite-direction forces denoted by F_{ext}. The aim is to find a relation between F_{ext} and the voltage applied to the transducer. Equation 2.91, can be written in the following form

$$x_{1p} - x_{2p} = \frac{4}{-\rho Al\omega^2 + \frac{\pi^2 A}{lS^E}}(f_{1p} - f_{2p} + \frac{-\rho Adl\omega^2 + \frac{\pi^2 Ad}{lS^E}}{4}V) \tag{2.92}$$

By splitting the voltage term between mechanical forces, this equation can be written as

$$x_{1p} - x_{2p} = \frac{4}{-\rho Al\omega^2 + \frac{\pi^2 A}{lS^E}}((f_{1p} - \frac{\rho Adl\omega^2 - \frac{\pi^2 Ad}{lS^E}}{8}V) - (f_{2p} + \frac{\rho Adl\omega^2 - \frac{\pi^2 Ad}{lS^E}}{8}V)) \tag{2.93}$$

Therefore, the relation between F_{ext} and the excitation voltage to the piezoelectric transducer, which agrees with the RCSA formulation of VAD tool holders, will be as follow:

$$F_{ext} = \left\{ \begin{array}{c} \frac{Ad}{8}(\rho l\omega^2 - \frac{\pi^2}{lS^E})V \\ 0 \end{array} \right\} \tag{2.94}$$

Chapter 3

Substructure Coupling and Numerical Simulations

3.1 Introduction

A VAD tool holder consists of several mechanical and electro-mechanical components. The performance of the assembled system is the result of the cooperation of all the components. Therefore, studying the effect of substructures on the dynamic of assembled system provides the ability to modify the system by tuning properties of substructures. The approach used in this study is dividing the system into several segments with relatively simpler geometry and then step-by-step coupling using the RCSA coupling method.

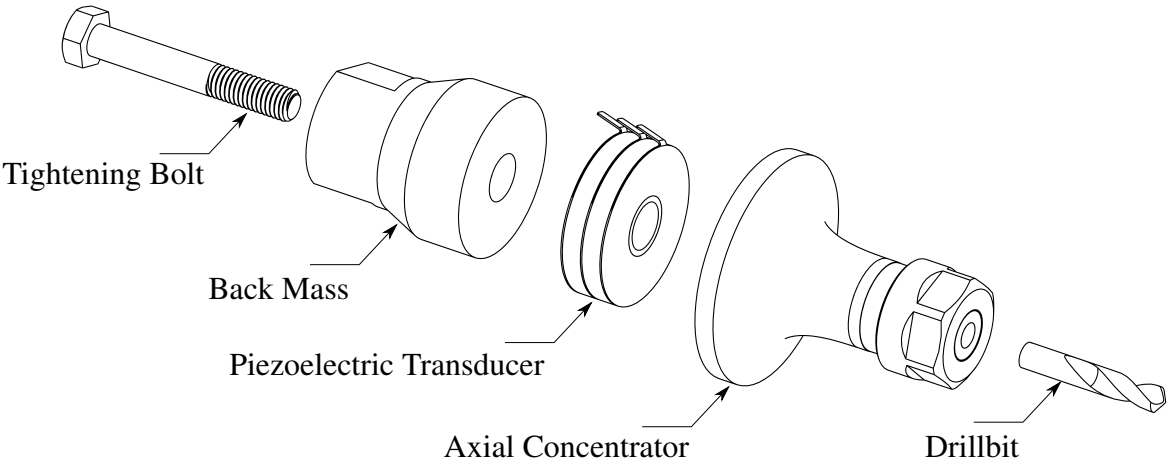

Fig. 3.1 Exploded view of axial toolholder

Two different types of VAD tool holders are studied: Axial tool holder and Axial-torsional tool holder. Axial tool holder refers to a VAD system with a type of concentrator that has

independent axial and torsional modes of vibration and there is no coupling between them. An exploded view of the axial tool holder is available in Fig.3.1.

In the axial-torsional tool holder, the type of concentrator used has a specific geometry which couples axial and torsional modes of vibration. An exploded view of the axial-torsional tool holder is shown in Fig.3.2.

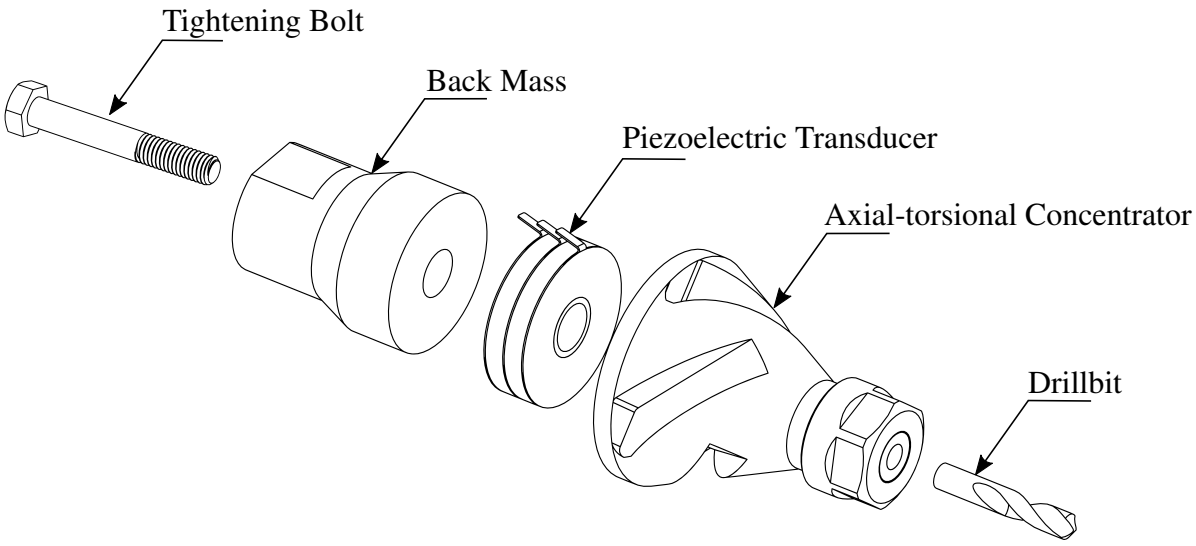

Fig. 3.2 Exploded view of axial-torsional toolholder

In this chapter, the axial and axial-torsional tool holders and their components are introduced and models of the assembled systems are developed through receptance coupling of their substructures. In the final section, the receptances computed by the models obtained from substructure coupling are compared to the receptances of the tool holder assembly simulated in a finite element software for validation.

3.2 Model development through substructure coupling

The VAD tool holders consist of several main components: drill bit, axial concentrator or axial-torsional concentrator, back mass, tightening bolt, and piezoelectric transducer. The components are shown in Fig.3.1 and Fig.3.2 for the axial tool holder and the axial-torsional tool holder, respectively. Substructures are divided into segments with simple geometries that efficient models are available for and are coupled using the RCSA method.

3.2.1 Modeling of back mass

One of the components of the VAD tool holder is the back mass. The back mass has three segments: two hollow cylinders with a truncated cone in between. The cylindrical parts are modeled using continuous system theory of rods and their FRF matrices are computed. For the truncated cone a finite element model consisting of 20 rod (disk) elements introduced in Chapter 2 is considered.

The first step is coupling the smaller hollow cylinder denoted as subsystem s and the truncated cone denoted as subsystem t.

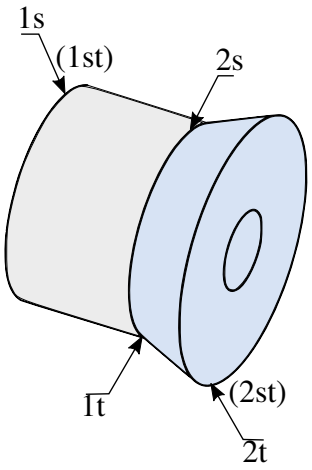

Fig. 3.3 Coupling of subsystems s (gray) and t (blue)

The two subsystems s and t are connected as shown in Fig.3.3. In this coupling, subsystem s at DOF $2s$ has the same physical displacement as subsystem t at DOF $1t$. The compatibility condition is

$$X_{2s} = X_{1t} \tag{3.1}$$

The equilibrium condition in this coupling is as follow:

$$F_{2s} + F_{1t} = 0 \tag{3.2}$$

The compatibility and equilibrium conditions of coupling subsystems s and t are the same as coupling subsystems a and b which was discussed in Chapter 2. Considering subsystem s as subsystem a and subsystem t as subsystem b, the FRF matrix of assembled system st becomes as follows:

$$\begin{aligned} H_{st} &= \begin{bmatrix} H_{1st1st} & H_{1st2st} \\ H_{2st1st} & H_{2st2st} \end{bmatrix}_{4\times4} \\ &= \begin{bmatrix} H_{1s1s} - H_{1s2s}(H_{2s2s}+H_{1t1t})^{-1}H_{2s1s} & H_{1s2s}(H_{2s2s}+H_{1t1t})^{-1}H_{1t2t} \\ H_{2t1t}(H_{1t1t}+H_{2s2s})^{-1}H_{2s1s} & H_{2t2t} - H_{2t1t}(H_{1t1t}+H_{2s2s})^{-1}H_{1t2t} \end{bmatrix}_{4\times4} \end{aligned} \tag{3.3}$$

The third segment of the back mass is a hollow cylinder. This subsystem is denoted as subsystem l. The model for the back mass denoted as system m is the outcome of coupling subsystems st and l. The coupling is shown in Fig.3.4.

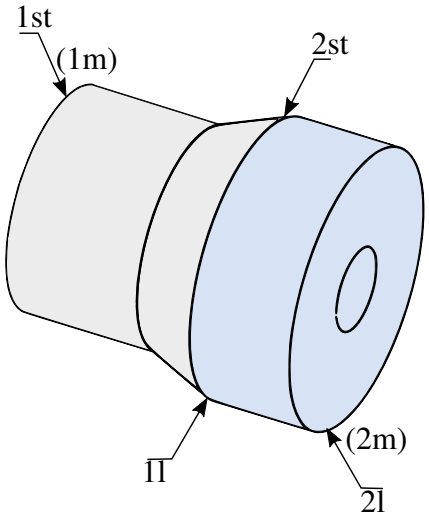

Fig. 3.4 Coupling of subsystem st (gray) and subsystem l (blue)

In this coupling, subsystem st at DOF $2st$ has the same physical displacement as subsystem l at DOF $1l$. The compatibility condition is

$$X_{2st} = X_{1l} \tag{3.4}$$

The equilibrium condition in this coupling is as follow:

$$F_{2st} + F_{1l} = 0 \tag{3.5}$$

The compatibility and equilibrium conditions of coupling subsystems *st* and *l* are the same as coupling subsystems *a* and *b* from Chapter 2. Considering subsystem *st* as subsystem *a* and subsystem *l* as subsystem *b*, the FRF matrix of assembled system *m* becomes as follows:

$$
\begin{aligned}
H_m &= \begin{bmatrix} H_{1m1m} & H_{1m2m} \\ H_{2m1m} & H_{2m2m} \end{bmatrix}_{4\times4} \\
&= \begin{bmatrix} H_{1st1st} - H_{1st2st}(H_{2st2st} + H_{1l1l})^{-1} H_{2st1st} & H_{1st2st}(H_{2st2st} + H_{1l1l})^{-1} H_{1l2l} \\ H_{2l1l}(H_{1l1l} + H_{2st2st})^{-1} H_{2st1st} & H_{2l2l} - H_{2l1l}(H_{1l1l} + H_{2st2st})^{-1} H_{1l2l} \end{bmatrix}_{4\times4}
\end{aligned}
\tag{3.6}
$$

3.2.2 Coupling of back mass and tightening bolt

The next step is coupling the back mass (subsystem *m*) to the tightening bolt which is denoted as subsystem *b*. The tightening bolt is modeled using the continuous system model of a rod. Fig.3.5 shows how these two subsystems are in contact.

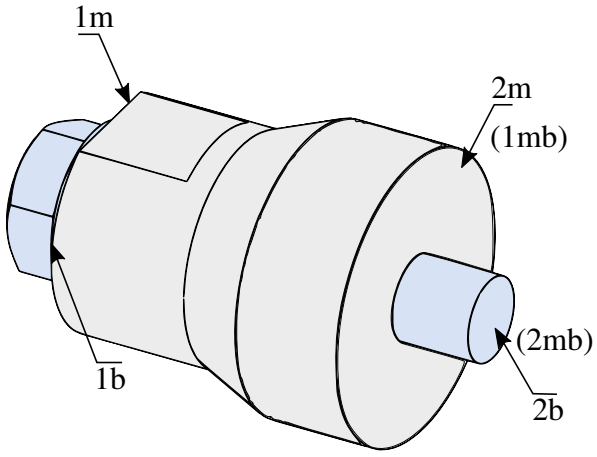

Fig. 3.5 Coupling of subsystem *m* (gray) and subsystem *b* (blue)

The subsystem *m* at DOF $1m$ is connected to the subsystem *b* at DOF $1b$. The compatibility condition is

$$X_{1m} = X_{1b} \tag{3.7}$$

In addition, in the coupling point the equilibrium condition is as follow:

$$F_{1b} + F_{1m} = 0 \tag{3.8}$$

Displacement vector of X_{2m} is a function of excitation at points $1m$ and $2m$:

$$X_{2m} = H_{2m1m}F_{1m} + H_{2m2m}F_{2m} \tag{3.9}$$

Considering the compatibility condition in Eq.3.7 and the equilibrium condition from Eq.3.8, the relation for F_{1m} will be as follow

$$X_{1m} = X_{1b} \rightarrow F_{1m} = (H_{1m1m} + H_{1b1b})^{-1}H_{1b2b}F_{2b} - (H_{1m1m} + H_{1b1b})^{-1}H_{1m2m}F_{2m} \tag{3.10}$$

In this stage, by substituting the relations of F_{1m} and F_{1b} (which is already known due to equilibrium condition of Eq.3.8), the displacement vector of point $2m$ from Eq.3.9 can be written as a function of excitation at points $2m$ and $2b$.

$$X_{2m} = (H_{2m2m} - H_{2m1m}(H_{1m1m} + H_{1b1b})^{-1}H_{1m2m})F_{2m} + H_{2m1m}(H_{1m1m} + H_{1b1b})^{-1}H_{1b2b}F_{2b} \tag{3.11}$$

The point $2mb$ in the system mb is the same point of $2b$ in subsystem b. Displacement vector of X_{2b} is a function of excitation at points $1b$ and $2b$:

$$X_{2b} = H_{2b1b}F_{1b} + H_{2b2b}F_{2b} \tag{3.12}$$

Considering the compatibility condition in Eq.3.7 and the equilibrium condition from Eq.3.8, the relation for F_{1b} will be as follow

$$X_{1m} = X_{1b} \rightarrow F_{1b} = (H_{1b1b} + H_{1m1m})^{-1}H_{1m2m}F_{2m} - (H_{1b1b} + H_{1m1m})^{-1}H_{1b2b}F_{2b} \tag{3.13}$$

In this stage, by substituting the relations of F_{1b} and F_{1m} (which is already known due to equilibrium condition of Eq.3.8), the displacement vector of point $2b$ from Eq.3.12 can be written as a function of excitation at points $2m$ and $2b$.

$$X_{2b} = H_{2b1b}(H_{1b1b} + H_{1m1m})^{-1}H_{1m2m}F_{2m} + [H_{2b2b} - H_{2b1b}(H_{1b1b} + H_{1m1m})^{-1}H_{1b2b}]F_{2b} \tag{3.14}$$

As mentioned before, the assembled subsystem of mb has degrees of freedom at points $1mb$ and $2mb$ which have the same values as $2m$ and $2b$, respectively. Therefore, the equations describing the assembled subsystem are obtained as follows

$$X_{1mb} = [H_{2m2m} - H_{2m1m}(H_{1m1m} + H_{1b1b})^{-1}H_{1m2m}]F_{1mb} + [H_{2m1m}(H_{1m1m} + H_{1b1b})^{-1}H_{1b2b}]F_{2mb} \tag{3.15}$$

$$X_{2mb} = [H_{2b1b}(H_{1b1b} + H_{1m1m})^{-1} H_{1m2m}]F_{1mb} + [H_{2b2b} - H_{2b1b}(H_{1b1b} + H_{1m1m})^{-1} H_{1b2b}]F_{2mb} \tag{3.16}$$

According to the Eq.3.15 and Eq.3.16, the direct and cross FRFs of the assembled system *mb* in a matrix form are

$$H_{mb} = \begin{bmatrix} H_{1mb1mb} & H_{1mb2mb} \\ H_{2mb1mb} & H_{2mb2mb} \end{bmatrix}_{4\times4}$$
$$= \begin{bmatrix} H_{2m2m} - H_{2m1m}(H_{1m1m} + H_{1b1b})^{-1} H_{1m2m} & H_{2m1m}(H_{1m1m} + H_{1b1b})^{-1} H_{1b2b} \\ H_{2b1b}(H_{1b1b} + H_{1m1m})^{-1} H_{1m2m} & H_{2b2b} - H_{2b1b}(H_{1b1b} + H_{1m1m})^{-1} H_{1b2b} \end{bmatrix}_{4\times4} \tag{3.17}$$

3.2.3 Coupling back mass and tightening bolt with piezoelectric transducer

The piezoelectric transducer consists of two piezoelectric rings and both of them are used as actuator which means they convert the applied alternative voltage to mechanical vibrations. In this application in VAD tool holder, the transducer only generates axial vibrations. Therefore, the effect of voltage on deformation of piezoelectric transducer is considered as external mechanical forces which applies at the two ends of piezoelectric transducer with opposite directions.

Since the effect of voltage will be involved as equivalent external forces, the set of two rings can be modeled as a regular material with no piezoelectric effect. This subsystem is in parallel contact with the assembly of back mass and tightening bolt which is considered as subsystem *mb*.

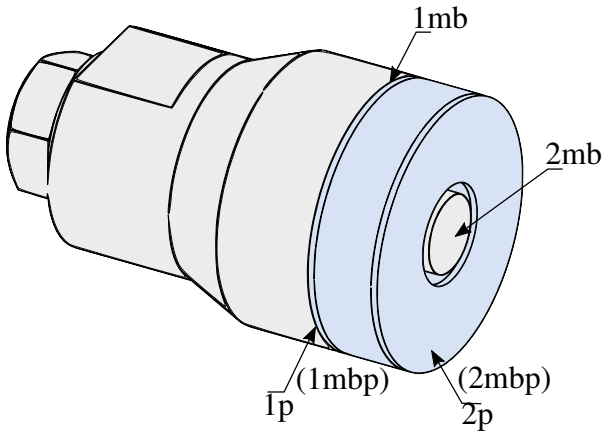

Fig. 3.6 Coupling of subsystem *mb* (gray) and subsystem *p* (blue)

Figure 3.6 shows coupling between subsystem *mb* and the subsystem p, the piezoelectric transducer. As shown in Fig.3.6, the point $1mb$ of subsystem *mb* has the same displacement as the point $1p$ of subsystem p. Also, the point $2mb$ of subsystem *mb* has the same displacement as the point $2p$ of subsystem p. Therefore, the compatibility conditions are

$$\begin{aligned} X_{1mb} &= X_{1p} \\ X_{2mb} &= X_{2p} \end{aligned} \tag{3.18}$$

Regarding the equilibrium conditions, the following equations hold

$$\begin{aligned} F_{1mbp} &= F_{1mb} + F_{1p} \\ F_{2mbp} &= F_{2mb} + F_{2p} \end{aligned} \tag{3.19}$$

According to the compatibility conditions in Eq.3.18, each one of the displacement vectors can be written as a function of the excitation forces acting on each subsystem

$$\begin{aligned} X_{1mb} = X_{1p} \rightarrow H_{1mb1mb}F_{1mb} + H_{1mb2mb}F_{2mb} &= H_{1p1p}F_{1p} + H_{1p2p}F_{2p} \\ X_{2mb} = X_{2p} \rightarrow H_{2mb1mb}F_{1mb} + H_{2mb2mb}F_{2mb} &= H_{2p1p}F_{1p} + H_{2p2p}F_{2p} \end{aligned} \tag{3.20}$$

In this type of coupling which subsystems are in parallel contact, the following matrix formation will simplify RCSA computations. For the subsystem *mb*

$$\left\{ \begin{array}{c} X_{1mb} \\ X_{2mb} \end{array} \right\} = \left[\begin{array}{cc} H_{1mb1mb} & H_{1mb2mb} \\ H_{2mb1mb} & H_{2mb2mb} \end{array} \right] \left\{ \begin{array}{c} F_{1mb} \\ F_{2mb} \end{array} \right\} \rightarrow H_{mb} = \left[\begin{array}{cc} H_{1mb1mb} & H_{1mb2mb} \\ H_{2mb1mb} & H_{2mb2mb} \end{array} \right] \tag{3.21}$$

and for the subsystem p

$$\left\{ \begin{array}{c} X_{1p} \\ X_{2p} \end{array} \right\} = \left[\begin{array}{cc} H_{1p1p} & H_{1p2p} \\ H_{2p1p} & H_{2p2p} \end{array} \right] \left\{ \begin{array}{c} F_{1p} \\ F_{2p} \end{array} \right\} \rightarrow H_{p} = \left[\begin{array}{cc} H_{1p1p} & H_{1p2p} \\ H_{2p1p} & H_{2p2p} \end{array} \right] \tag{3.22}$$

where FRF matrices of H_{mb} and H_p are 4×4 matrices containing direct and cross FRFs of axial and torsional modes of subsystem *mb* and p, respectively.

In parallel coupling, the assembled system has the same displacement vectors as the individual subsystems:

$$\left\{ \begin{array}{c} X_{1mbp} \\ X_{2mbp} \end{array} \right\} = \left\{ \begin{array}{c} X_{1mb} \\ X_{2mb} \end{array} \right\} = \left\{ \begin{array}{c} X_{1p} \\ X_{2p} \end{array} \right\} \tag{3.23}$$

where each one of the displacement vectors are 4×1 vectors consist of axial and torsional displacements of the two coupling points of each subsystem. The equlibrium condition

mentioned in Eq.3.19 in this matrix format is

$$\left\{ \begin{array}{c} F_{1mbp} \\ F_{2mbp} \end{array} \right\} = \left\{ \begin{array}{c} F_{1mb} \\ F_{2mb} \end{array} \right\} + \left\{ \begin{array}{c} F_{1p} \\ F_{2p} \end{array} \right\} = H_{mb}^{-1} \left\{ \begin{array}{c} X_{1mb} \\ X_{2mb} \end{array} \right\} + H_{p}^{-1} \left\{ \begin{array}{c} X_{1p} \\ X_{2p} \end{array} \right\} \tag{3.24}$$

and by considering the Eq.3.23

$$\left\{ \begin{array}{c} F_{1mbp} \\ F_{2mbp} \end{array} \right\} = (H_{mb}^{-1} + H_{p}^{-1}) \left\{ \begin{array}{c} X_{1mbp} \\ X_{2mbp} \end{array} \right\} \tag{3.25}$$

At the end, the FRF matrix of the assembled system mbp will be

$$H_{mbp} = (H_{mb}^{-1} + H_{p}^{-1})^{-1} \tag{3.26}$$

where H_{mbp} is a 4×4 matrix containing direct and cross FRFs of axial and torsional modes of the system mbp.

3.2.4 Coupling of concentrator and drill bit

The difference between axial tool holder and axial-torsional tool holder is the type of their concentrators. The FRF matrix of the axial concentrator has independent axial and torsional modes while the FRF matrix of the axial-torsional concentrator includes coupled axial and torsional modes. Nevertheless, from the RCSA coupling perspective, they will be treated the same and are considered as subsystem c. The FRF matrices of each concentrator are computed using a 3D model in finite element software. The drill bit is denoted as subsystem d. The FRF matrix of the drill bit is obtained from the finite element method presented in Chapter 2.

The concentrator and drill bit are assembled as depicted in Fig.3.7 and Fig.3.8 for axial tool holder and axial-torsional tool holder, respectively.

In this coupling, subsystem c at DOF $2c$ has the physical displacement as subsystem d at DOF $1d$. This defines the compatibility condition as follow:

$$X_{2c} = X_{1d} \tag{3.27}$$

and the following equilibrium condition holds:

$$F_{2c} + F_{1d} = 0 \tag{3.28}$$

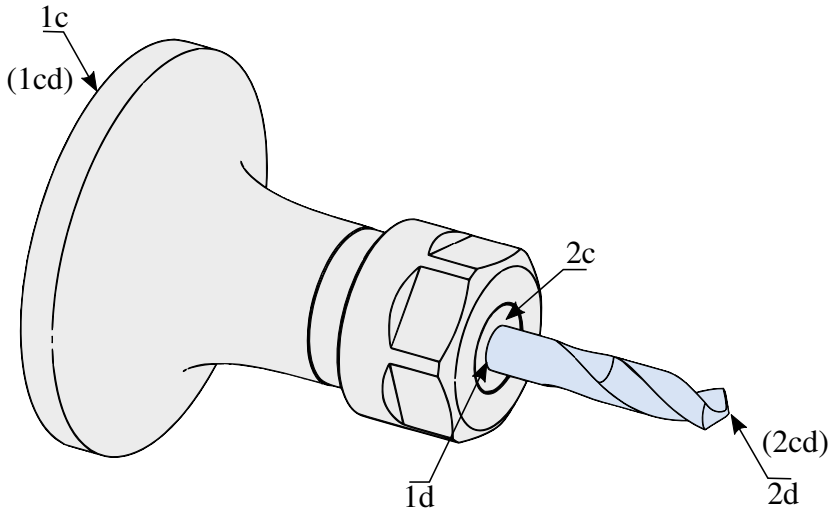

Fig. 3.7 Coupling of axial concentrator and drill bit

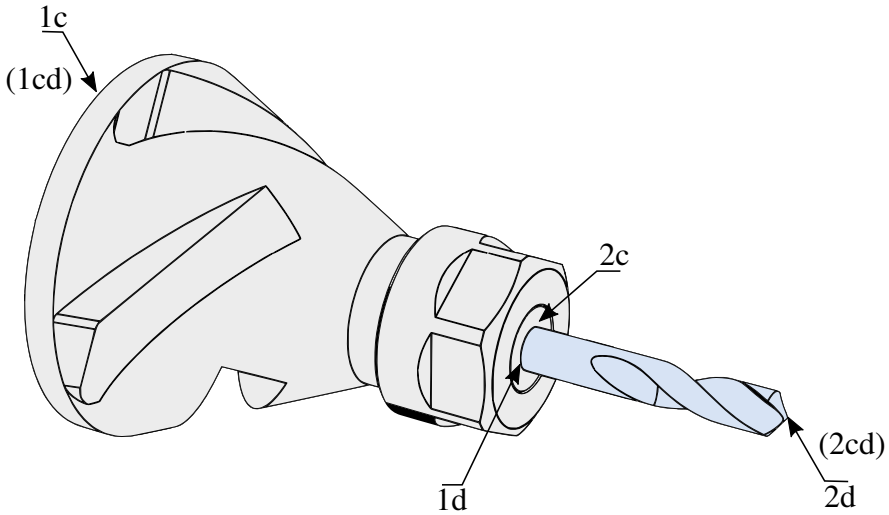

Fig. 3.8 Coupling of axial-torsional concentrator and drill bit

The coupling of subsystems c and d is similar to the case discussed in Chapter 2. Considering subsystem c as a and d and b, the FRF matrix of assembled system cd becomes as follow:

$$H_{cd} = \begin{bmatrix} H_{1cd1cd} & H_{1cd2cd} \\ H_{2cd1cd} & H_{2cd2cd} \end{bmatrix}_{4\times4}$$
$$= \begin{bmatrix} H_{1c1c} - H_{1c2c}(H_{2c2c} + H_{1d1d})^{-1} H_{2c1c} & H_{1c2c}(H_{2c2c} + H_{1d1d})^{-1} H_{1d2d} \\ H_{2d1d}(H_{1d1d} + H_{2c2c})^{-1} H_{2c1c} & H_{2d2d} - H_{2d1d}(H_{1d1d} + H_{2c2c})^{-1} H_{1d2d} \end{bmatrix}_{4\times4} \tag{3.29}$$

3.2.5 Assembly model of VAD tool holders

In the previous steps, different components of the VAD tool holder are coupled into the two subsystems of *mbp* and *cd*. In this step, these two subsystems will be coupled and the model for the axial tool holder and also axial-torsional tool holder will be completed.

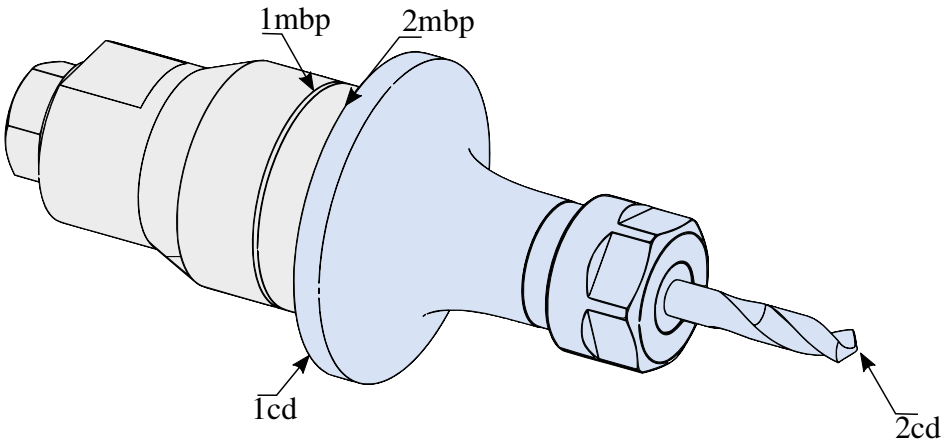

Fig. 3.9 Completed assembly of axial tool holder

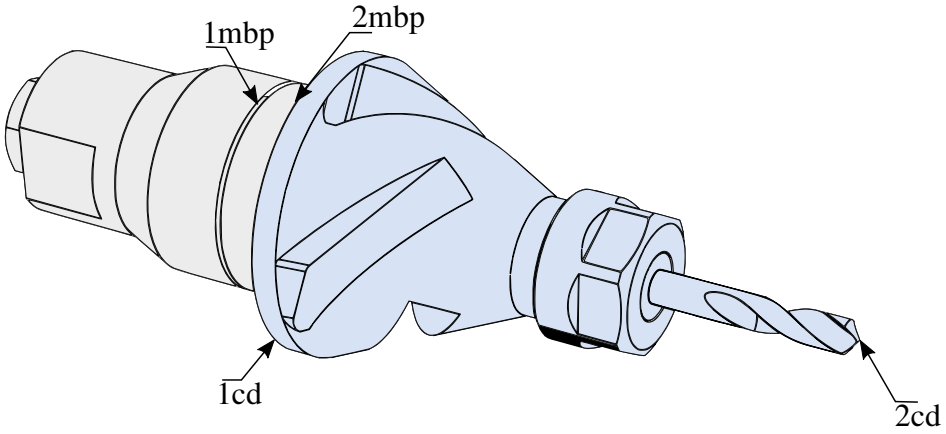

Fig. 3.10 Completed assembly of axial-torsional tool holder

In this coupling step, subsystem *mbp* at DOF 2*mbp* is connected to the subsystem *cd* at DOF 1*cd*. Figure 3.11 contains a schematic model describing the final coupling step to achieve the assembly model of axial and axial-torsional tool holders.

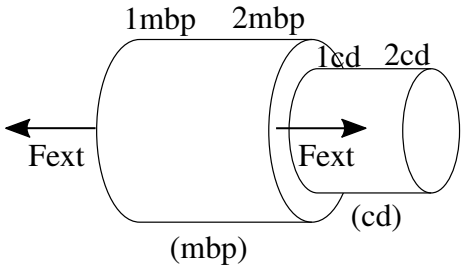

Fig. 3.11 Schematic coupling model of subsystems *mbp* and *cd*

Subsystem *mbp* at DOF 2*mbp* is connected to the subsystem *cd* at DOF 1*cd*. The pair of opposite-direction forces of F_{ext} represents the effect of the voltage applied to the piezoelectric transducer. The relation between F_{ext} and the voltage is mentioned in Eq.2.94. The compatibility condition is as follow

$$X_{2mbp} = X_{1cd} \tag{3.30}$$

The following relations hold for equilibrium condition of the forces

$$\begin{aligned} F_{1mbp} &= F_{ext} \\ F_{2mbp} + F_{1cd} &= -F_{ext} \end{aligned} \tag{3.31}$$

The point of interest in this formulation is the tip of the drill bit which is denoted as the DOF 2*cd*. Considering the subsystem *cd*, the displacement vector 2*cd* is computed through the following equation

$$X_{2cd} = H_{2cd1cd} F_{1cd} \tag{3.32}$$

In Eq.3.32, the force vector of F_{1cd} should be replaced as a function of F_{ext}. Using the compatibility condition from Eq.3.30, the value of F_{1c} will be as follow

$$\begin{aligned} X_{2mbp} = X_{1cd} \rightarrow H_{2mbp1mbp} F_{1mbp} + H_{2mbp2mbp} F_{2mbp} &= H_{1cd1cd} F_{1cd} \\ \rightarrow F_{1cd} = (H_{1cd1cd} + H_{2mbp2mbp})^{-1} (H_{2mbp1mbp} - H_{2mbp2mbp}) F_{ext} \end{aligned} \tag{3.33}$$

By substituting F_{1cd} from Eq.3.33 into Eq.3.32, the final equation which relates the displacement vector of the drill tip to the force F_{ext} will be written as follow

$$X_{2cd} = H_{2cd1cd} (H_{1cd1cd} + H_{2mbp2mbp})^{-1} (H_{2mbp1mbp} - H_{2mbp2mbp}) F_{ext} \tag{3.34}$$

3.3 Validation of VAD tool holder models

In the previous sections, models for axial and axial-torsional tool holders were developed through receptance coupling of substructures. This section aims to investigate the validation of the models developed earlier. For this purpose, the receptance FRFs at the drillbit's tip obtained from the RCSA models are compared to the ones obtained using a 3D finite element model developed in a commercial software. A tool holder assembly is modeled in COMSOL Multiphysics software using structural modeling interface. The type of mesh used is free tetrahedral with 169208 number of elements for the axial tool holder shown in Fig.3.12 and 177040 number of elements for the axial-torsional tool holder shown in Fig.3.13.

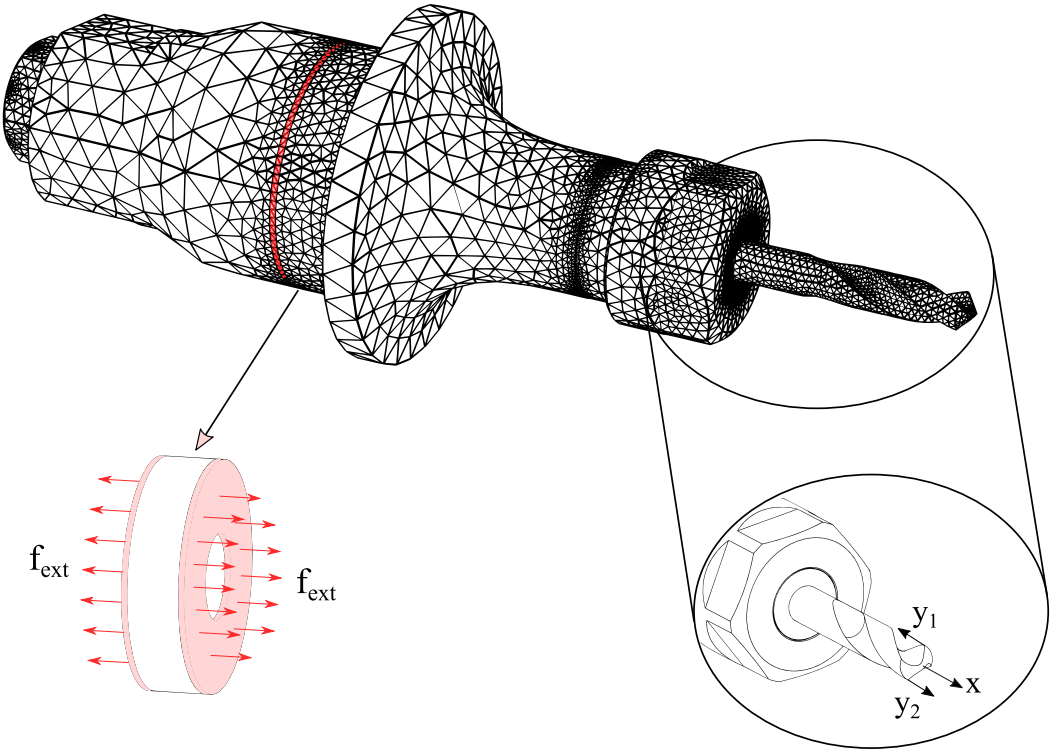

Fig. 3.12 Excitation and measurements of axial tool holder in COMSOL Multiphysics

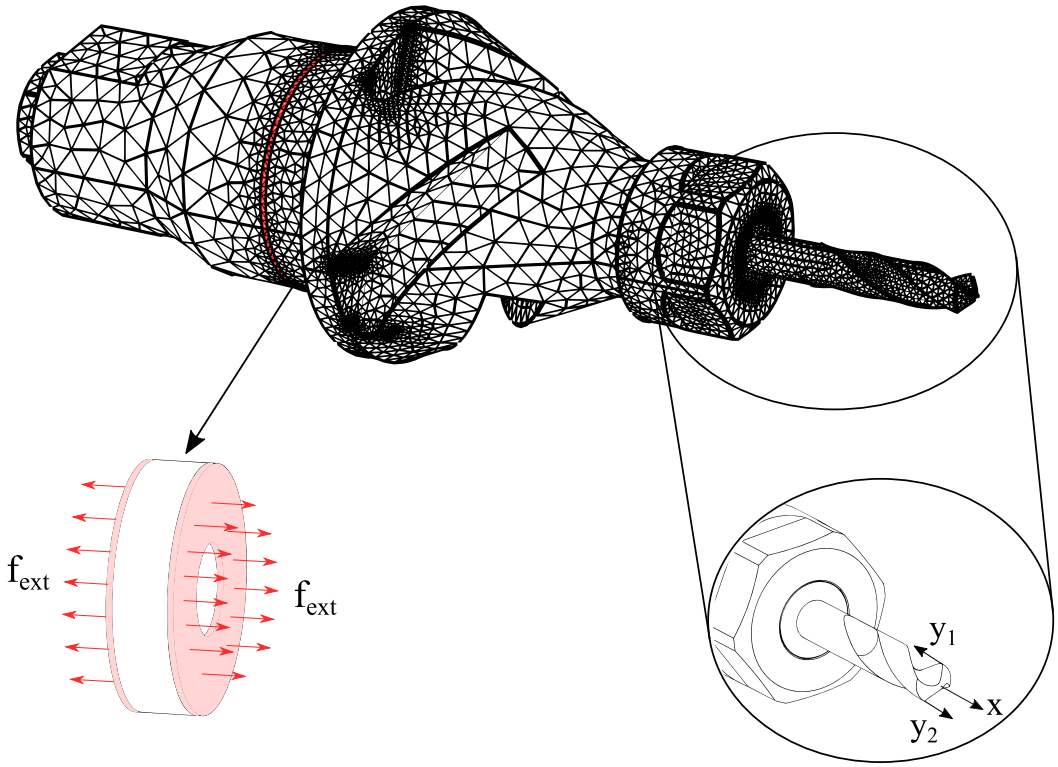

Fig. 3.13 Excitation and measurements of axial-torsional tool holder in COMSOL Multi-physics

As can be seen in Fig.3.12 and Fig.3.13, the excitation to the assembly is a pair of opposite-direction distributed forces applied at the two DOFs of the piezoelectric transducer. This forces are shown by the red color arrows. The axial displacement is measures at the tip of the drill bit which is shown by the vector x. The torsional displacement of the drill bit tip is computed by measuring the tangential displacements of y_1 and y_2 and substituting in the following equation:

$$\theta = \frac{y_1 + y_2}{d} \tag{3.35}$$

Where d is the diameter of the drill bit. The tangential displacement is influenced by torsional modes and also bending modes. In order to eliminate the effect of the bending modes, the tangential displacements are measured at two opposite locations at the tip of the drill bit.

3.3.1 Validation of the axial tool holder model

In order to validate the model developed through the RCSA approach, the system responses at the drill bit tip are compared to results obtained from the 3D finite element model. For this simulation, the pair of F_{ext} forces are considered as the excitation to the system and the axial

displacement (DOFs x) and torsional displacement (DOF θ) at the drill bit tip are considered as the responses of the system as shown in Fig.3.14.

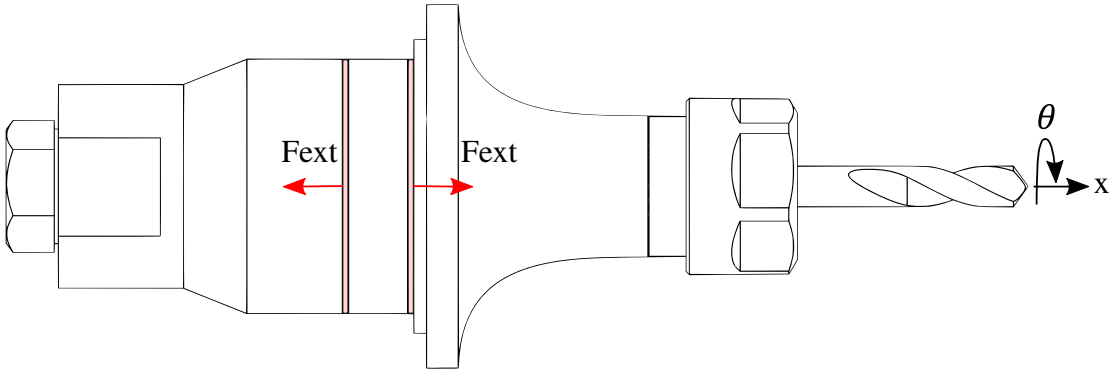

Fig. 3.14 Axial tool holder assembly model

The assembly's axial receptance at the drill bit tip obtained from the RCSA model is plotted versus the axial receptance of the 3D model computed by the finite element software in the semi-logarithmic plot shown in Fig.3.15.

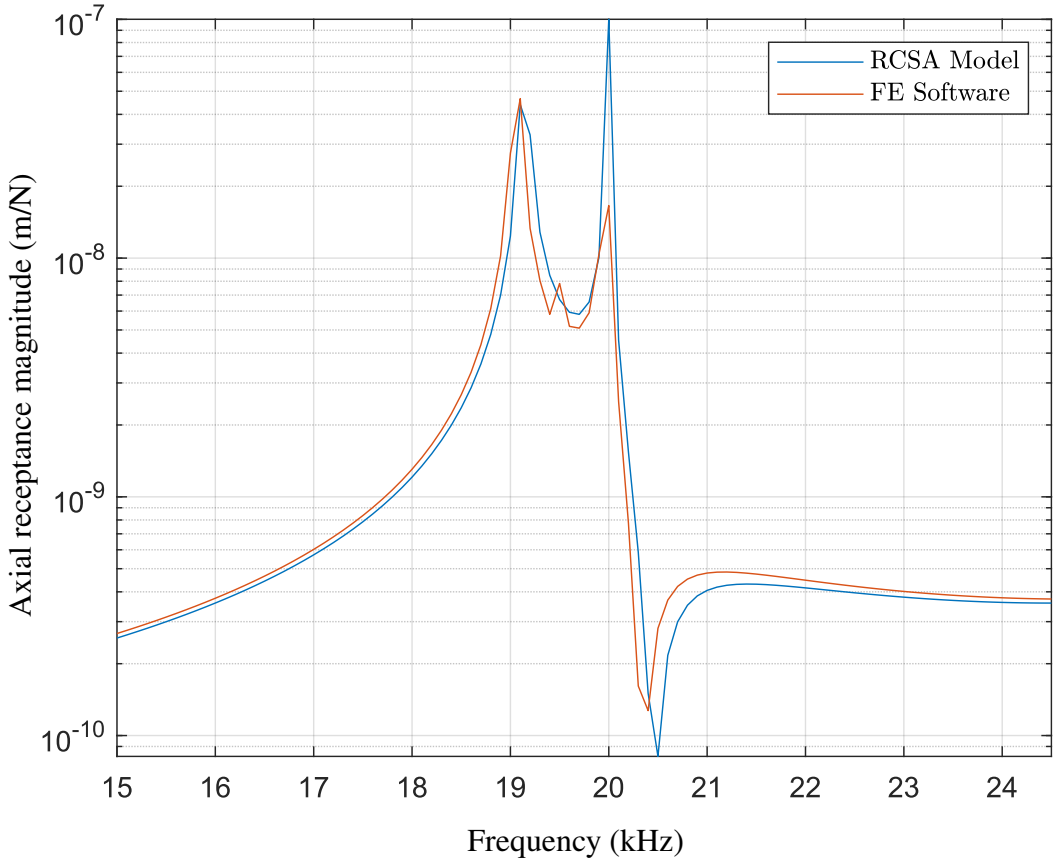

Fig. 3.15 Axial receptance at drill tip for axial tool holder

The semi-logarithmic plot shown in Fig.3.16, contains the assembly's torsional receptance obtained from the RCSA model and the 3D model in the finite element software for the DOF θ at the drill bit tip.

The results presented in Fig.3.15 and Fig.3.16 shows that the RCSA approach can predict the dynamics of the axial tool holder with a good accuracy. The required computation time for the RCSA model was in the order of a few seconds while the finite element software required around one hour.

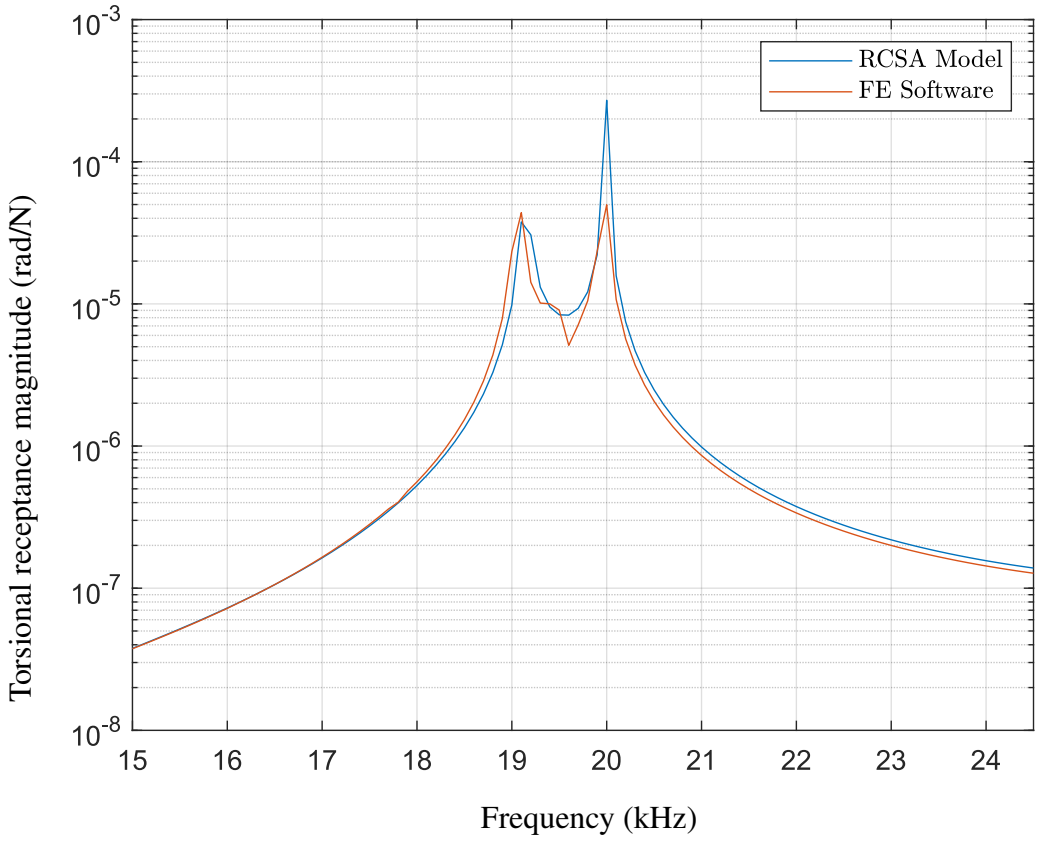

Fig. 3.16 Torsional receptance at drill tip for axial tool holder

3.3.2 Validation of axial-torsional tool holder model

In order to validate the model of axial-torsional tool holder developed through the RCSA approach, the system responses at the drill bit tip are plotted versus the results obtained from the 3D finite element model. For this simulation, the pair of F_{ext} forces are considered as the excitation to the system and the axial displacement (DOFs x) and torsional displacement (DOF θ) at the drill bit tip are considered as the responses of the system as shown in Fig.3.17.

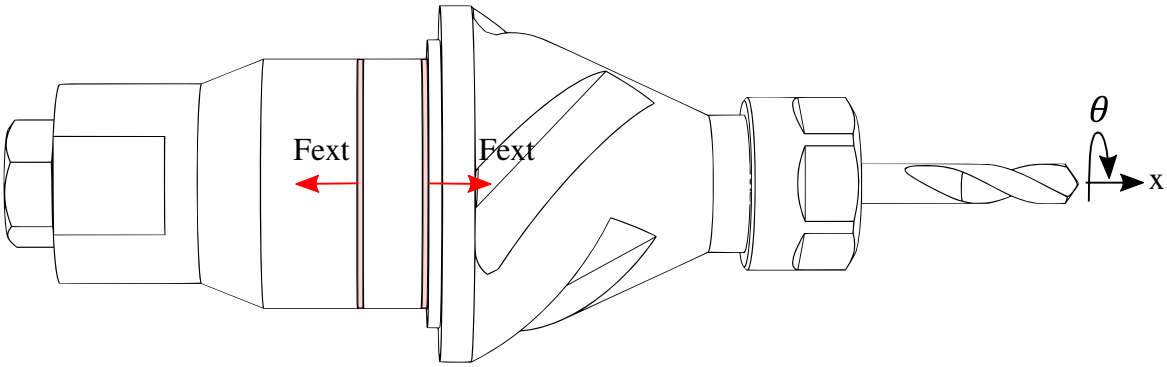

Fig. 3.17 Axial-torsional tool holder assembly model

The assembly's axial receptance at the drill bit tip obtained from the RCSA model is plotted versus the axial receptance of the 3D model computed by the finite element software in the semi-logarithmic plot shown in Fig.3.18.

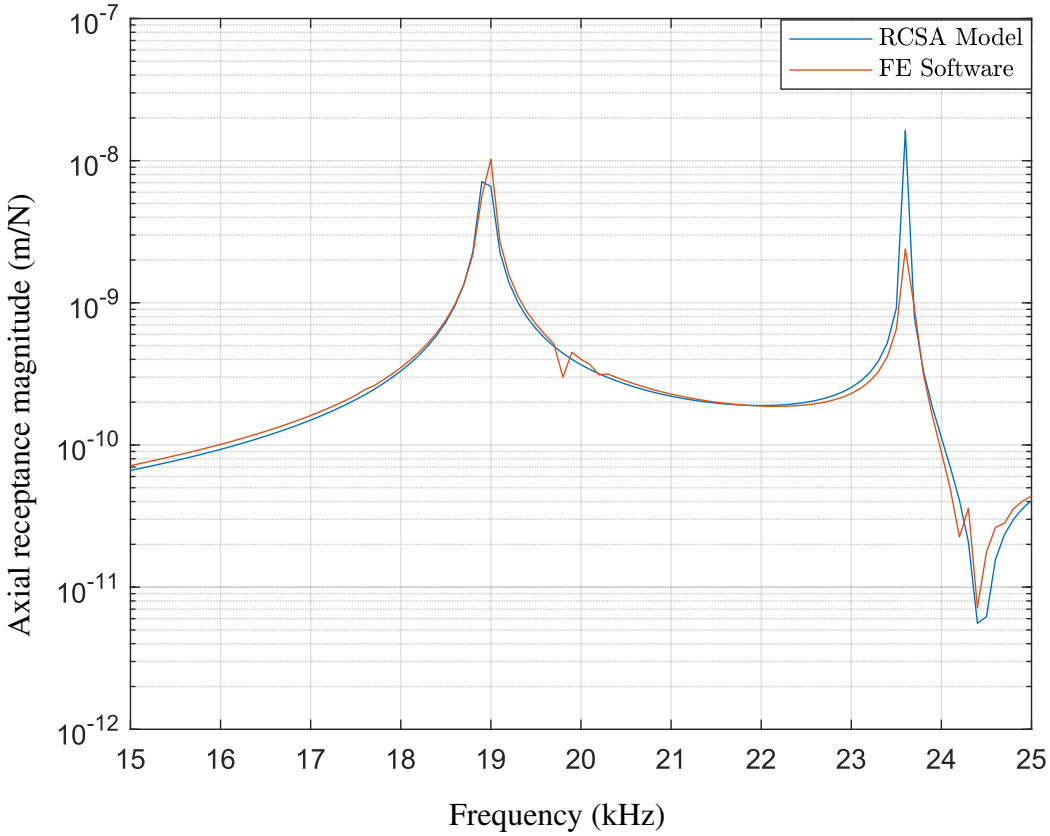

Fig. 3.18 Axial receptance at drill tip for axial-torsional tool holder

The semi-logarithmic plot shown in Fig.3.19, contains the assembly's torsional receptance obtained from the RCSA model and the 3D model in the finite element software for the DOF θ at the drill bit tip.

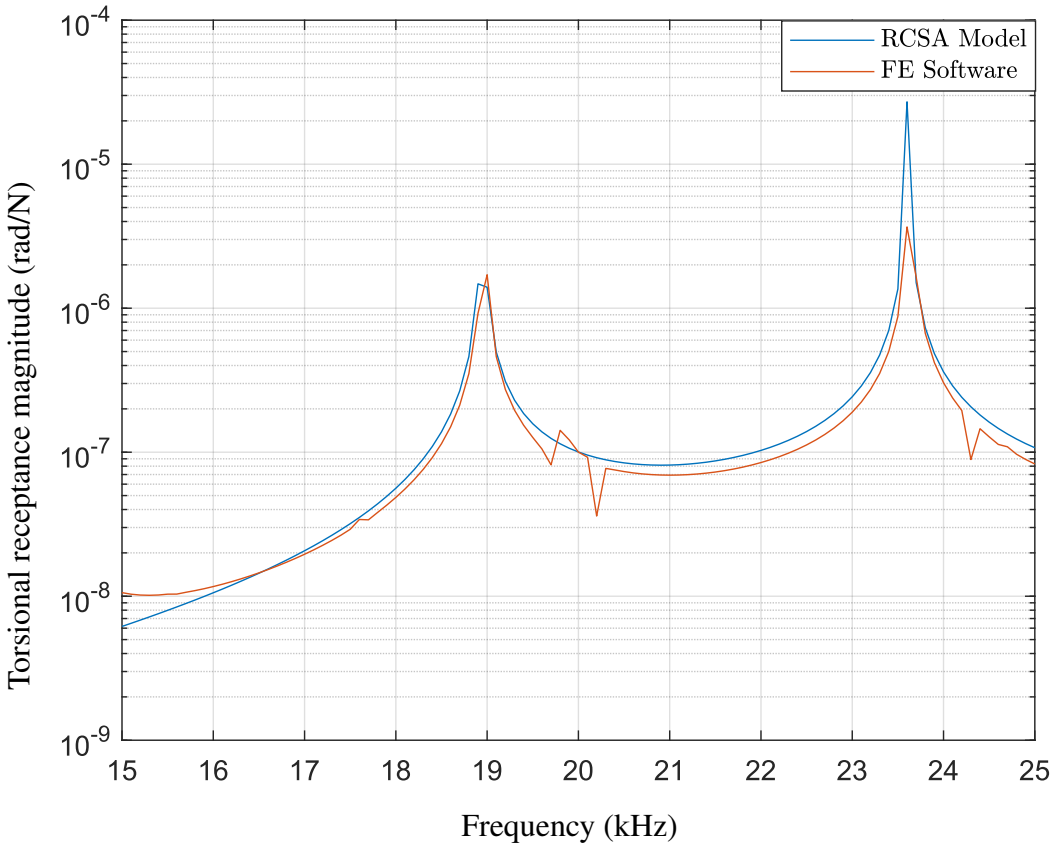

Fig. 3.19 Torsional receptance at drill tip for axial-torsional tool holder

The results presented in Fig.3.18 and Fig.3.19, show that the RCSA approach can predict the dynamics of the axial-torsional tool holder with a good accuracy. Similar to the axial tool holder, the required computation time for the RCSA model was in the order of a few seconds while the finite element software required around one hour.

Chapter 4

Experimental Results and Structural Modification

4.1 Introduction

In this chapter, the presented RCSA approach is used to determine the axial and torsional receptances of a VAD system with axial concentrator. In addition, the substructure analysis method is extended to include the stiffness and damping at the joint interfaces between the components of the VAD system. After experimentally validating the accuracy of the presented RCSA approach in modeling the dynamics of the VAD system, this model is used to change the dynamic characteristics of the built VAD system by adjusting the overhang length of the drill bit and the electrical components of the piezoelectric transducer.

4.2 Experimental setup

The experimental setup consisting of the VAD and data acquisition systems is described in this section. The piezoelectric transducer needs an AC voltage to excite the operational mode of the tool holder on its resonant frequency. The AC voltage is generated by a function generator. A schematic view of the powering circuit of the VAD toolholder is depicted in Fig.4.1.

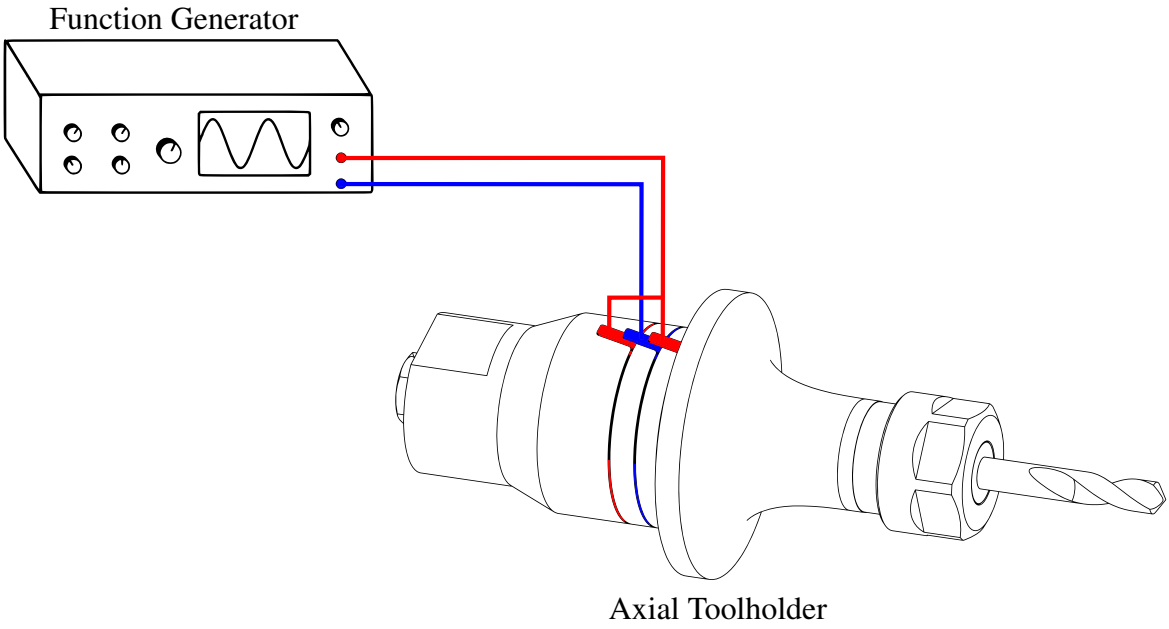

Fig. 4.1 Powering VAD tool holder by function generator

The input to this system is the excitation voltage applied by the function generator and the outputs are axial displacement and torsional displacement of the drill bit tip as well as the electric current flowing through the circuit. In order to experimentally identify the dynamics of the physical system, the data corresponding to the input and the outputs of the system must be collected. The system is fed with a sine sweep signal in the frequency range of 15 to 24.5 kHz.

Data collection is done using a Data Acquisition Card (DAQ). As mentioned, the input to the system is the voltage applied to the piezoelectric transducer. This voltage is in the range of -11 to +11 volts. The DAQ card only can tolerate voltages in the range of -5 to +5 volts. Therefore, the piezoelectric transducer terminals cannot be directly connected to the DAQ card channels for voltage measurement. In order to bring this voltage to the range of DAQ card measurement, a voltage divider circuit is employed.

The circuit used as the voltage divider is shown in Fig.4.2. In this figure, piezoelectric voltage is denoted by V_p which will damage the DAQ card if connected directly. The voltage

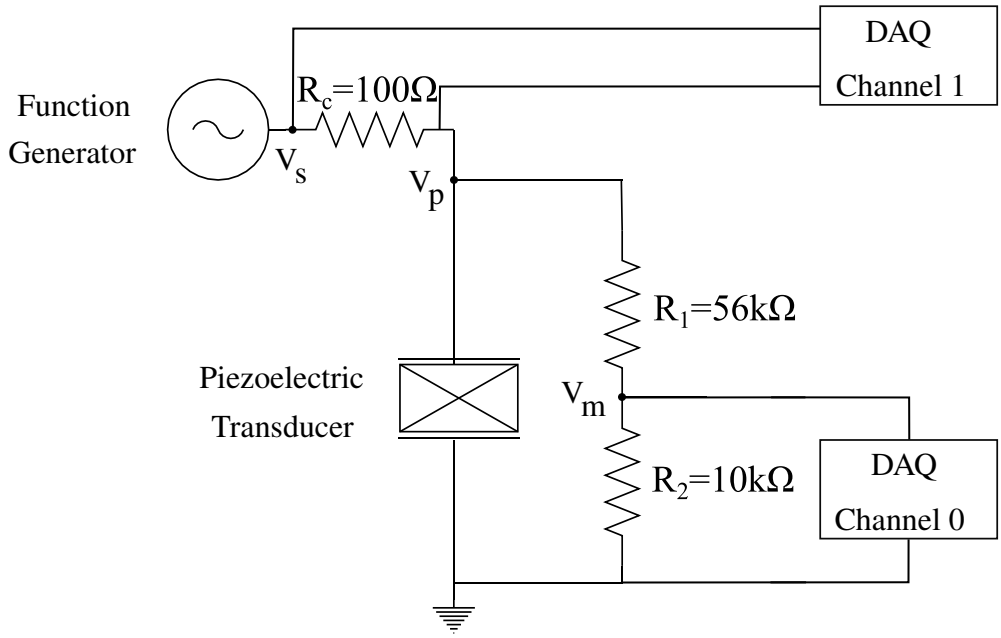

Fig. 4.2 Measuring Voltage and Current of piezoelectric transducer

measured by the DAQ card is V_m which is computed using the following relation of voltage dividers:

$$V_m = \frac{R_1}{R_1 + R_2} V_p \rightarrow V_m = \frac{10}{10+56} V_p = \frac{1}{6.6} V_p \tag{4.1}$$

Considering Eq.4.1, V_p which was in the range of -11 to +11 volts is now mapped to the range of -1.67 to +1.67 volts of V_m. This range of voltage is safe to be connected to Channel 0 of the DAQ card.

As shown in Fig.4.2, Channel 1 of the DAQ card is measuring the voltage drop by the R_c resistor, which is connected in series to the piezoelectric transducer. Therefore, the same current taken by the piezoelectric transducer passes through the R_c resistor. Using Ohm's law, the current can easily be computed through the voltage data collected by Channel 1 of the DAQ card.

$$I_p = \frac{V_s - V_p}{R_c} \tag{4.2}$$

The current is valuable data for the reason that can be measured easily even through the machining process. This data will be used for model updating and can be used for online process monitoring. As mentioned before, piezoelectric materials have a coupling between their mechanical and electrical properties. The direct piezoelectric effect is the concept for piezoelectric sensors and the converse effect for piezoelectric actuators.

The converse piezoelectric effect determines the relation between the excitation voltage and the mechanical deformation generating mechanical vibrations and, at the same time, the direct piezoelectric effect determines how much current is taken by the piezoelectric transducer in that operational condition. Therefore, the current data contains valuable information about the structural dynamics of the assembly and the parameters influencing their dynamics.

The equipment used for measuring vibration is accelerometers. The data collected using accelerometers is converted to displacement by integration in frequency-domain. Since the drill bit tip does not have flat surfaces to attach accelerometers on, an adaptor is designed and attached to the tip of the drill bit as shown with a blue color in Fig.4.3. This figure also shows the positions where the accelerometers are installed. The accelerometer measuring axial acceleration is connected to channel 1 of the DAQ card. Two accelerometers located at the two sides are for measuring tangential acceleration and are connected to channels 2 and 3 of the DAQ card. The reason for using two accelerometers is to cancel the effect of bending modes and measure torsional acceleration of the drill bit tip with higher accuracy.

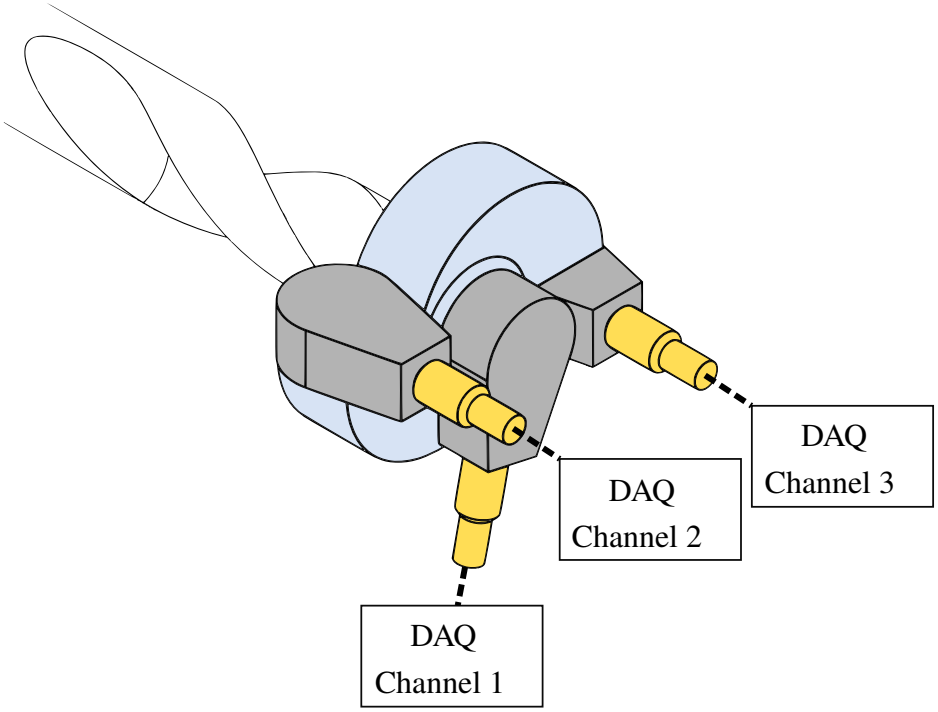

Fig. 4.3 Measuring axial and torsional displacements of drill bit tip

In the model development process, there was no consideration of boundary conditions. In other words, the model has free-free boundary conditions. The free-free boundary condition

is attempted to be provided to the physical system by hanging the tool holder by rubbers from a top support. A picture of the experimental setup is provided in Fig. 4.4.

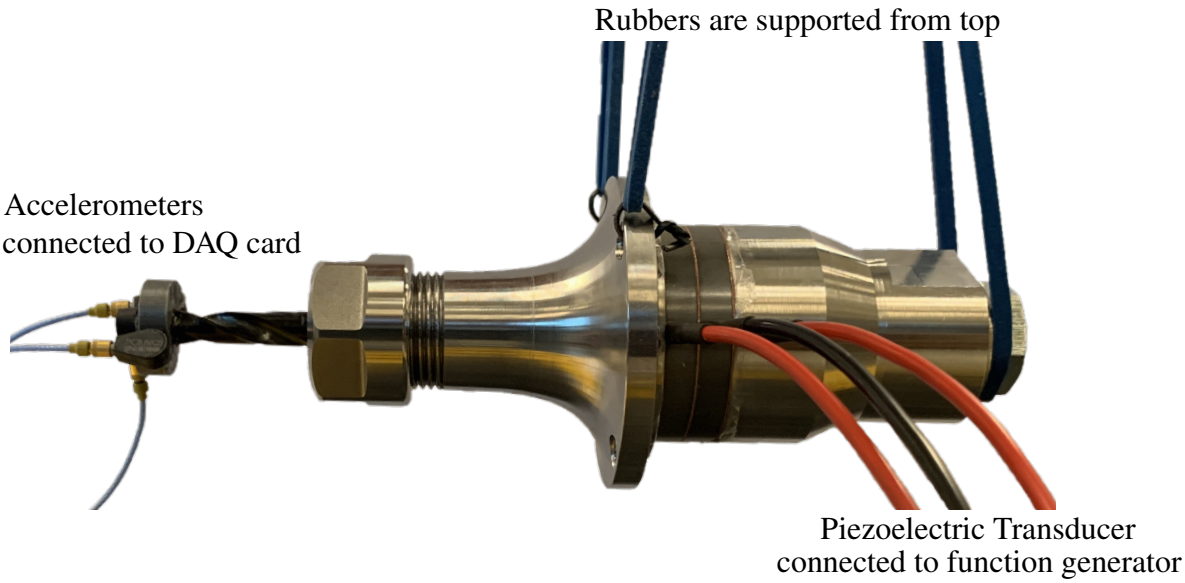

Fig. 4.4 Experimental setup

4.3 Electric current modeling through RCSA

The converse piezoelectric effect was studies in the previous sections for modeling the actuation role of the piezoelectric transducer in exciting the structure of VAD systems at their resonant frequency. The direct piezoelectric effect also can be used simultaneously which enables the ability of using the piezoelectric transducer as a sensor at the same time being used as an actuator. The constitutive equation describing the direct piezoelectric effect is provided in Eq.2.78 and the simplified form of Eq.2.80 for the VAD tool holder transducer. Rewriting the Eq.2.79 for mechanical stress leads to the relation below

$$\sigma = \frac{\varepsilon - dE}{S^E} \tag{4.3}$$

By substituting Eq.4.3 into Eq.2.80, the relation of electric displacement as a function of strain and electric field is written as

$$D = \frac{d}{S^E}\varepsilon + (\xi^\sigma - \frac{d^2}{S^E})E \tag{4.4}$$

In order to achieve a relation for the electric charge, the parameters of Eq.4.4 should be substituted by the following relations: the relation between electric displacement (D) and

electric charge (q) of $D = q/A$, where A stands for the cross-section area of the piezoelectric transducer; the mechanical strain (ε) relation with axial displacement of $\varepsilon = (x_{1p} - x_{2p})/l$, where x_{1p} and x_{2p} are axial displacements at the two DOFs of the piezoelectric transducer; the relation for electric field (E) caused by the applied voltage (V) of $E = V/l$, where l is the thickness of piezoelectric transducer. Note that all of the displacement, force, voltage, current, electric charge and FRF parameters are functions of frequency, which is omitted from notations for simplicity.

$$q = \frac{Ad}{lS^E}(x_{1p} - x_{2p}) + (\frac{AS^E\xi^\sigma - Ad^2}{lS^E})V \tag{4.5}$$

Electric current is defined as the rate of change in electric charge over time. This description in the frequency domain is expressed as $I = (j\omega) * q$. Therefore, the electric current relation is obtained as follow

$$I = \frac{Ad}{lS^E}j\omega(x_{1p} - x_{2p}) + (\frac{AS^E\xi^\sigma - Ad^2}{lS^E}j\omega)V \tag{4.6}$$

The relations for x_{1p} and x_{2p} should be obtained through the model developed by the RCSA approach. In the final coupling step in Chapter 3, subsystems *mbp* and *cd* were coupled to obtain the model of the VAD tool holder assembly. Figure 3.11 shows a schematic of the final coupling to obtain a model for the completed assembly. The same compatibility condition of Eq.3.30 and equilibrium condition of Eq.3.31 hold here as well.

Since the system *mbp* was the result of parallel coupling of subsystems *p* and *mb*, the displacement vector X_{1p} has the same value as X_{1mbp}. X_{1p} is written as a function of the forces applied to the subsystem *mbp* as follow

$$X_{1p} = X_{1mbp} = H_{1mbp1mbp}F_{1mbp} + H_{1mbp2mbp}F_{2mbp} \tag{4.7}$$

By substituting the equilibrium condition from Eq.3.31, X_{1p} becomes

$$X_{1p} = (H_{1mbp1mbp} - H_{1mbp2mbp})F_{ext} - H_{1mbp2mbp}F_{1cd} \tag{4.8}$$

Equation 3.33 illustrates the relation of F_{1cd} and F_{ext}. By substituting Eq.3.33 in Eq.4.8, the following relation between X_{1p} and F_{ext} will be the obtained

$$\begin{aligned} X_{1p} = [&H_{1mbp1mbp} - H_{1mbp2mbp} - \\ &H_{1mbp2mbp}(H_{1cd1cd} + H_{2mbp2mbp})^{-1}(H_{2mbp1mbp} - H_{2mbp2mbp})]F_{ext} \end{aligned} \tag{4.9}$$

By substituting Eq.2.94 in Eq.4.9, the relation between X_{1p} and the voltage will be derived as follows

$$X_{1p} = [H_{1mbp1mbp} - H_{1mbp2mbp} - H_{1mbp2mbp}(H_{1cd1cd} + H_{2mbp2mbp})^{-1}(H_{2mbp1mbp} - H_{2mbp2mbp})] \begin{Bmatrix} \frac{Ad}{8}(\rho l \omega^2 - \frac{\pi^2}{lS^E})V \\ 0 \end{Bmatrix} \tag{4.10}$$

The displacement vector X_{2p} is also the same as the displacement vector X_{2mbp} because of the parallel coupling of subsystems p and mbp. X_{2p} can also be written as a function of the forces applied to the subsystem mbp as follow

$$X_{2p} = X_{2mbp} = H_{2mbp1mbp}F_{1mbp} + H_{2mbp2mbp}F_{2mbp} \tag{4.11}$$

Considering the equilibrium condition presented in Eq.3.31, X_{2p} is written as

$$X_{2p} = (H_{2mbp1mbp} - H_{2mbp2mbp})F_{ext} - H_{2mbp2mbp}F_{1cd} \tag{4.12}$$

By substituting the relation between F_{1cd} and F_{ext} from Eq.3.33 in Eq.4.12, the following relation between X_{2p} and F_{ext} will be derived

$$X_{2p} = [H_{2mbp1mbp} - H_{2mbp2mbp} - H_{2mbp2mbp}(H_{1cd1cd} + H_{2mbp2mbp})^{-1}(H_{2mbp1mbp} - H_{2mbp2mbp})]F_{ext} \tag{4.13}$$

By substituting Eq.2.94 in Eq.4.13, the relation between X_{2p} and the voltage will be derived as follows

$$X_{2p} = [H_{2mbp1mbp} - H_{2mbp2mbp} - H_{2mbp2mbp}(H_{1cd1cd} + H_{2mbp2mbp})^{-1}(H_{2mbp1mbp} - H_{2mbp2mbp})] \begin{Bmatrix} \frac{Ad}{8}(\rho l \omega^2 - \frac{\pi^2}{lS^E})V \\ 0 \end{Bmatrix} \tag{4.14}$$

Through the RCSA approach, the displacement vectors X_{1p} and X_{2p} are obtained in Eq.4.10 and Eq.4.14 as functions of voltage, respectively. As mentioned in Chapter 2, the displacement vectors contain both axial and torsional displacements i.e. $X_{1p} = [x_{1p}, \theta_{1p}]^T$ and $X_{2p} = [x_{2p}, \theta_{2p}]^T$. Therefore, axial displacements x_{1p} and x_{2p} are determined as functions of V.

When both piezoelectric rings are used as actuators, which is the case for the VAD system shown in Fig.4.1, V and l in Eq.4.6 should be substituted by the effective voltage to the piezoelectric transducer of $2V_p$ and the total thickness of $2l_p$, respectively. V_p is the voltage applied to the piezoelectric transducer and l_p is the thickness of a single piezoelectric ring.Therefore, the equation describing the electric current I_p as a function of V_p will be as follow

$$I_p = \frac{Ad}{2l_pS^E} j\omega(x_{1p} - x_{2p}) + (\frac{AS^E\xi^\sigma - Ad^2}{2l_pS^E} j\omega)2V_p \tag{4.15}$$

The current FRF H_{I_p} is defined as follow

$$H_{I_p} = \frac{I_p}{V_p} \tag{4.16}$$

where H_{I_p}, I_p and V_p are complex-valued functions of frequency.

4.4 Model updating and joint identification

The theoretical model developed through substructure coupling is not necessarily representative of the physical model dynamics. In the theoretical model, it was assumed that the system is undamped and all substructures are coupled rigidly. These assumptions may not apply to the physical system. In order to make the model a better representative of the physical model, springs and dampers are places in the joints shown in Fig. 4.5. These are the connections that are more probable to behave non-rigidly.

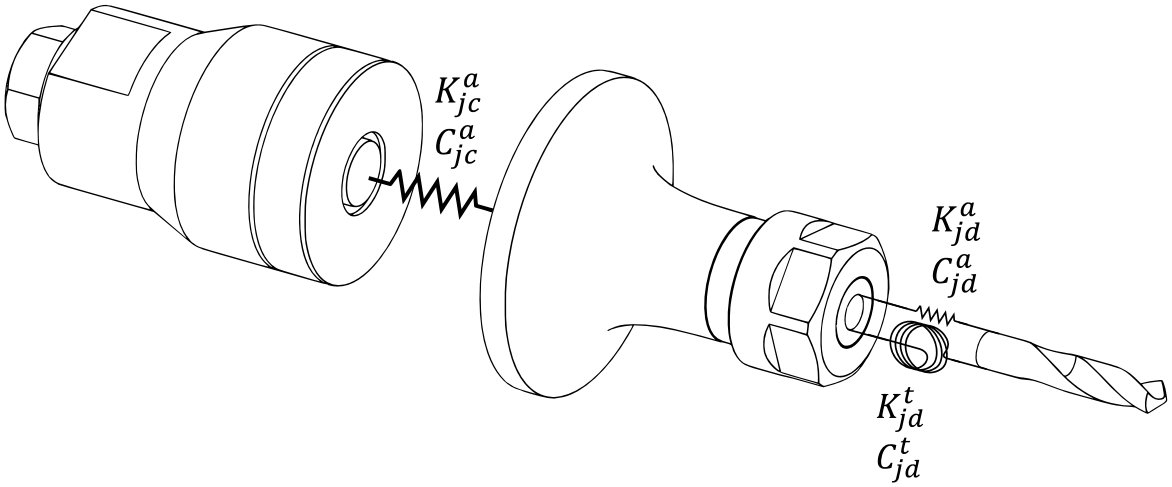

Fig. 4.5 RCSA model with joint flexibility and damping

The joint between concentrator and drill bit which will be considered as subsystem *jd* has both axial and torsional flexibility and dissipation. This joint is considered as a thin weightless cylindrical element coupled with the drill bit as shown in Fig.4.6. This flexible cylindrical element is modeled by the rod model developed in Section 2.3.1. Young's modulus (E_{jd}) and modulus of rigidity (G_{jd}) of the joint element are complex numbers which respectively represent axial and torsional flexibility and damping of the joint. Their values should be identified experimentally. Identifying the complex-valued parameter of E_{jd} leads to compute K^a_{jd} and C^a_{jd}. Similarly, identifying the complex-valued parameter of G_{jd} leads to compute K^t_{jd} and C^t_{jd}.

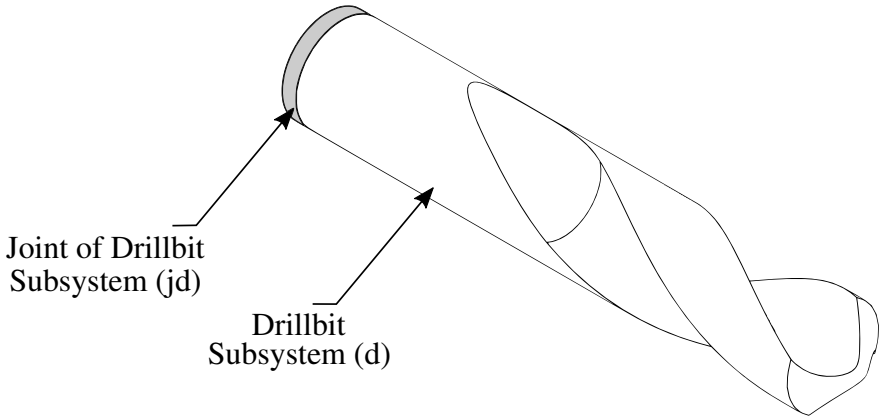

Fig. 4.6 Coupling drill bit and subsystem jd

According to the formulation for coupling subsystems in Section 2.2.2, the FRF matrix of the system of coupled d (equivalent of subsystem a) and jd (equivalent of subsystem b), denoted as subsystem d' will be as follow

$$H_{d'} = \begin{bmatrix} H_{1d'1d'} & H_{1d'2d'} \\ H_{2d'1d'} & H_{2d'2d'} \end{bmatrix}_{4\times4}$$
$$= \begin{bmatrix} H_{1jd1jd} - H_{1jd2jd}(H_{2jd2jd} + H_{1d1d})^{-1}H_{2jd1jd} & H_{1jd2jd}(H_{2jd2jd} + H_{1d1d})^{-1}H_{1d2d} \\ H_{2d1d}(H_{1d1d} + H_{2jd2jd})^{-1}H_{2jd1jd} & H_{2d2d} - H_{2d1d}(H_{1d1d} + H_{2jd2jd})^{-1}H_{1d2d} \end{bmatrix}_{4\times4} \tag{4.17}$$

The joint between the concentrator and the piezoelectric transducer has flexibility and damping in the axial direction. This joint will be considered as subsystem jc. This joint is also considered as a thin weightless cylindrical element coupled with the concentrator as shown in Fig.4.7. Young's modulus (E_{jc}) of the joint element is a complex number that represents axial flexibility and damping of the joint. Its value should be identified experimentally. Identifying the complex-valued parameter of E_{jc} leads to computing K^a_{jc} and C^a_{jc}.

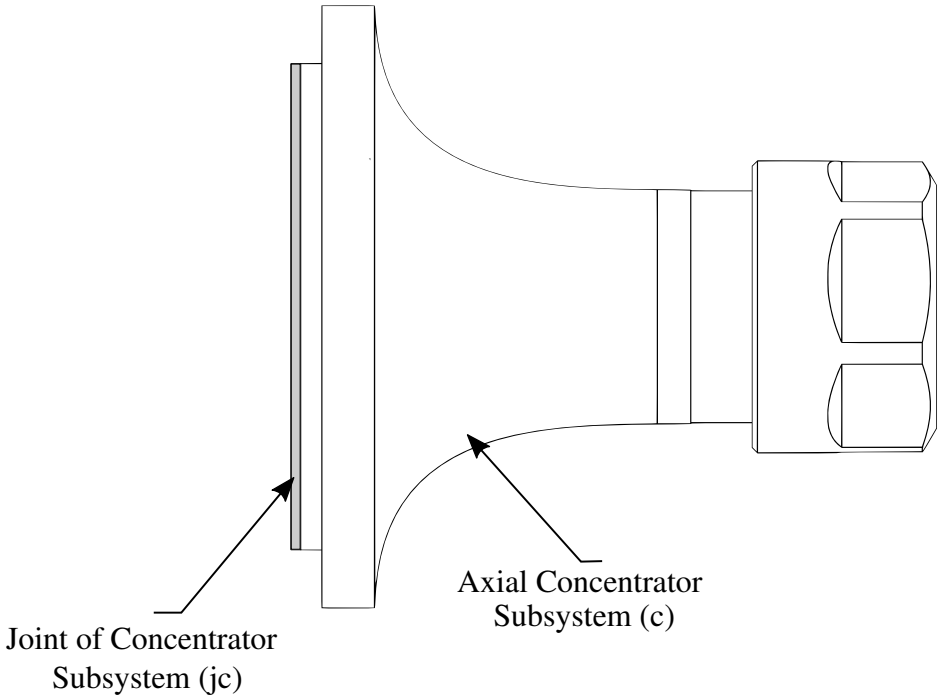

Fig. 4.7 Coupling concentrator and subsystem jc

According to the formulation for coupling subsystems in Section 2.2.2, the FRF matrix of the system of coupled c (equivalent of subsystem a) and jc (equivalent of subsystem b), denoted as subsystem c' will be as follow

$$
\begin{aligned}
H_{c'} &= \begin{bmatrix} H_{1c'1c'} & H_{1c'2c'} \\ H_{2c'1c'} & H_{2c'2c'} \end{bmatrix}_{4\times4} \\
&= \begin{bmatrix} H_{1jc1jc} - H_{1jc2jc}(H_{2jc2jc} + H_{1c1c})^{-1} H_{2jc1jc} & H_{1jc2jc}(H_{2jc2jc} + H_{1c1c})^{-1} H_{1c2c} \\ H_{2c1c}(H_{1c1c} + H_{2jc2jc})^{-1} H_{2jc1jc} & H_{2c2c} - H_{2c1c}(H_{1c1c} + H_{2jc2jc})^{-1} H_{1c2c} \end{bmatrix}_{4\times4}
\end{aligned}
\tag{4.18}
$$

Subsystems c' and d' are connected with the same arrangement as subsystems c and d, as shown in Fig.3.7. FRF matrix of the system $c'd'$ will be as follow

$$H_{c'd'} = \begin{bmatrix} H_{1c'd'1c'd'} & H_{1c'd'2c'd'} \\ H_{2c'd'1c'd'} & H_{2c'd'2c'd'} \end{bmatrix}_{4\times4}$$
$$= \begin{bmatrix} H_{1c'1c'} - H_{1c'2c'}(H_{2c'2c'} + H_{1d'1d'})^{-1}H_{2c'1c'} & H_{1c'2c'}(H_{2c'2c'} + H_{1d'1d'})^{-1}H_{1d'2d'} \\ H_{2d'1d'}(H_{1d'1d'} + H_{2c'2c'})^{-1}H_{2c'1c'} & H_{2d'2d'} - H_{2d'1d'}(H_{1d'1d'} + H_{2c'2c'})^{-1}H_{1d'2d'} \end{bmatrix}_{4\times4} \tag{4.19}$$

An schematic view of coupling the substructures for the system shown in Fig.4.5, is provided in Fig.4.8. It is the result of coupling subsystems mbp and $c'd'$.

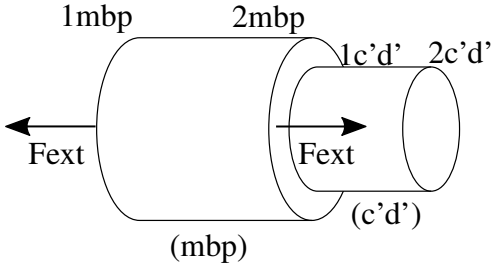

Fig. 4.8 Coupling subsystems $c'd'$ and mbp

The result of coupling subsystem $c'd'$ and mbp, has the same formulation of coupling subsystems mbp and cd as presented in Eq.3.34. Therefore, the displacement vector for the DOF $2c'd'$ at the tip of the drill bit will be as follow

$$X_{2c'd'} = H_{2c'd'1c'd'}(H_{1c'd'1c'd'} + H_{2mbp2mbp})^{-1}(H_{2mbp1mbp} - H_{2mbp2mbp})F_{ext} \tag{4.20}$$

As mentioned before, joint stiffness and damping are the parameters which should be identified experimentally. In this work, an optimization algorithm is used to determine the joint parameters that would lead to minimum difference between predicted and measured FRFs. Usually this model updating method is implemented by using displacement to force FRFs, which requires the installation of accelerometers on the setup to measure the FRFs. To avoid the practical complexities involved in the installation of accelerometers in an industrial setup, in this work the FRF between the transducer current and the supplied voltage is used for model updating. A sine sweep voltage is applied to the system and the resulting current is measured using the setup described in Section 4.2.

Joints are identified through an optimization algorithm whose objective is to minimize the difference between the magnitudes of the current FRF obtained from the theoretical model

and experimental data. The frequency range chosen for the optimization algorithm is the half-power bandwidth of the system in the operating mode. The half-power bandwidth is a range of frequency in which the magnitude of the current FRF is not less than $\sqrt{2}$ of the magnitude of current FRF at the resonant frequency.[18] This bandwidth is shown in Fig.4.9.

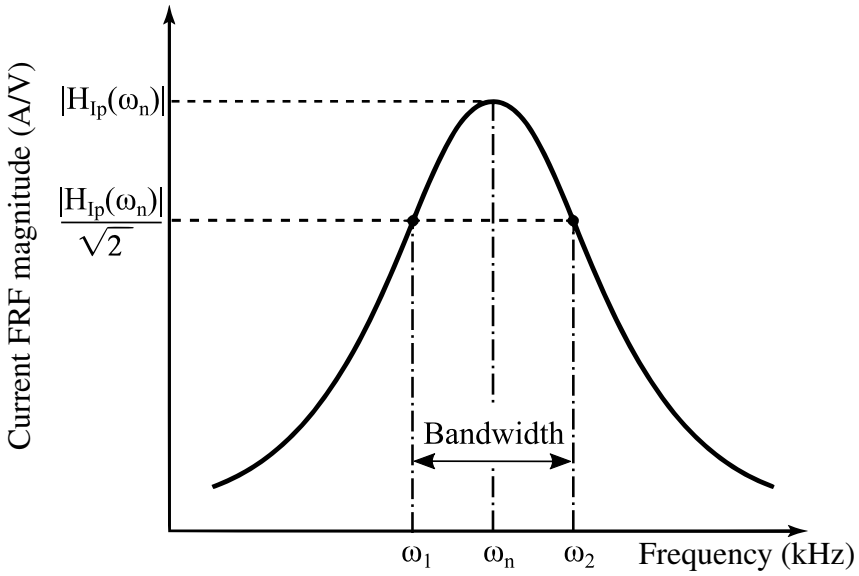

Fig. 4.9 Half-power bandwidth of the system [18]

The objective is elimination of the difference between 1) natural frequencies of the model and experimental data 2) magnitude of current FRF in the frequency range of the half-power bandwidth. The objective function satisfying these criteria would be as follow

$$f_{obj}(E_{jd},G_{jd},E_{jc}) =$$
$$(\omega_n-\omega_n^{\exp})^2+\frac{1}{N_\omega}\sum_{i=-N_\omega/2}^{N_\omega/2}\left(\left|H_{I_p}(\omega_n+i\delta\omega,E_{jd},G_{jd},E_{jc})\right|-\left|H_{I_p}^{\exp}(\omega_n^{\exp}+i\delta\omega)\right|\right)^2 \quad (4.21)$$

where H_{I_p} is the current FRF computed by the RCSA approach in Section 4.3 and is influenced by the joint parameters (E_{jd}, G_{jd} and E_{jc}), $H_{I_p}^{exp}$ is current FRF measured experimentally, ω_n is the natural frequency computed by the RCSA model, $\omega_n^{\exp}$ is the natural frequency measured experimentally, $\delta\omega$ is the frequency resolution and N_ω is the number of data points in the bandwidth computed using following equation

$$N_\omega=\frac{\omega_2-\omega_1}{\delta\omega} \quad (4.22)$$

Figure 4.10 shows that after convergence of the optimization algorithm, the current FRF magnitude has approached to the current FRF magnitude measured experimentally. The outcome of the optimization algorithm is the computation of the joint parameters values.

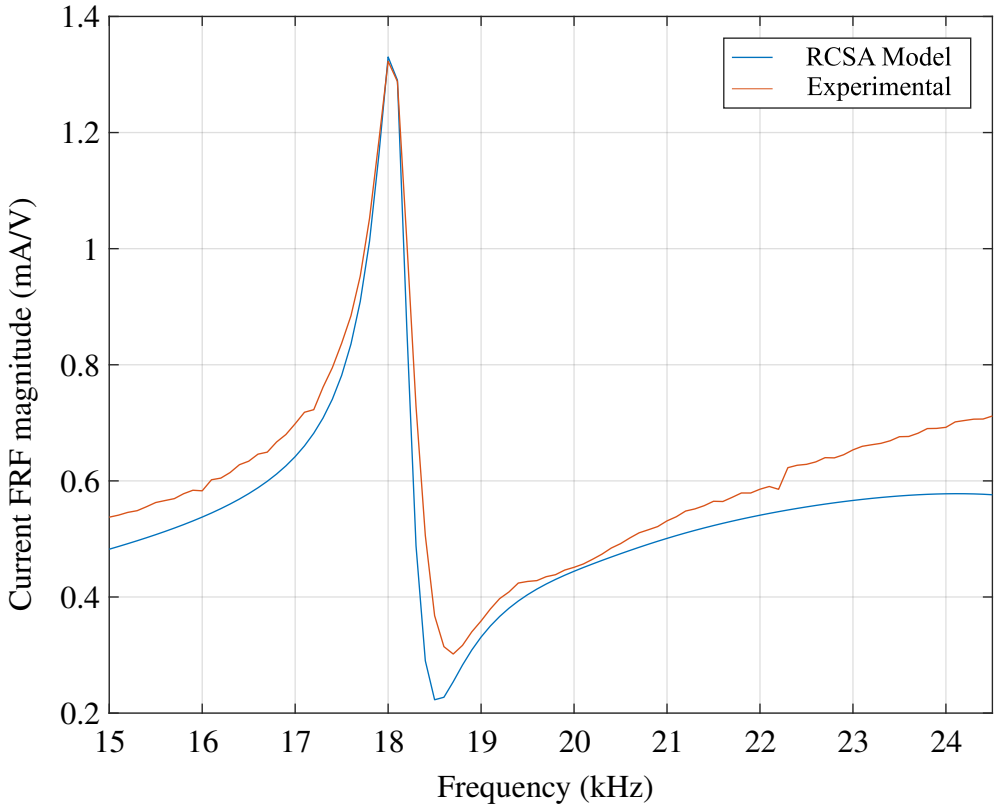

Fig. 4.10 Current FRF magnitude for 27.5 mm clamped length

Through this identification process the values for axial and torsional stiffness and damping of the joints are computed as follows

$$\begin{aligned} K^a_{jd} &= 1.9224\text{e}+09[\text{N/m}]; C^a_{jd} = 9.6203\text{e}+07[\text{N.s/m}] \\ K^t_{jd} &= 7.1503\text{e}+02[\text{N/m}]; C^t_{jd} = 1.4994\text{e}+02[\text{N.m.s}] \\ K^a_{jc} &= 7.5839\text{e}+10[\text{N/m}]; C^a_{jc} = 3.1325\text{e}+10[\text{N.s/m}] \end{aligned} \tag{4.23}$$

Using the identified joint parameters the axial and torsional receptances of the drill bit tip are computed and plotted alongside with the experimentally measured receptances in Fig.4.11 and Fig.4.12, respectively. The agreement between predicted and measured data shows that joint identification using current FRF data is a promising approach.

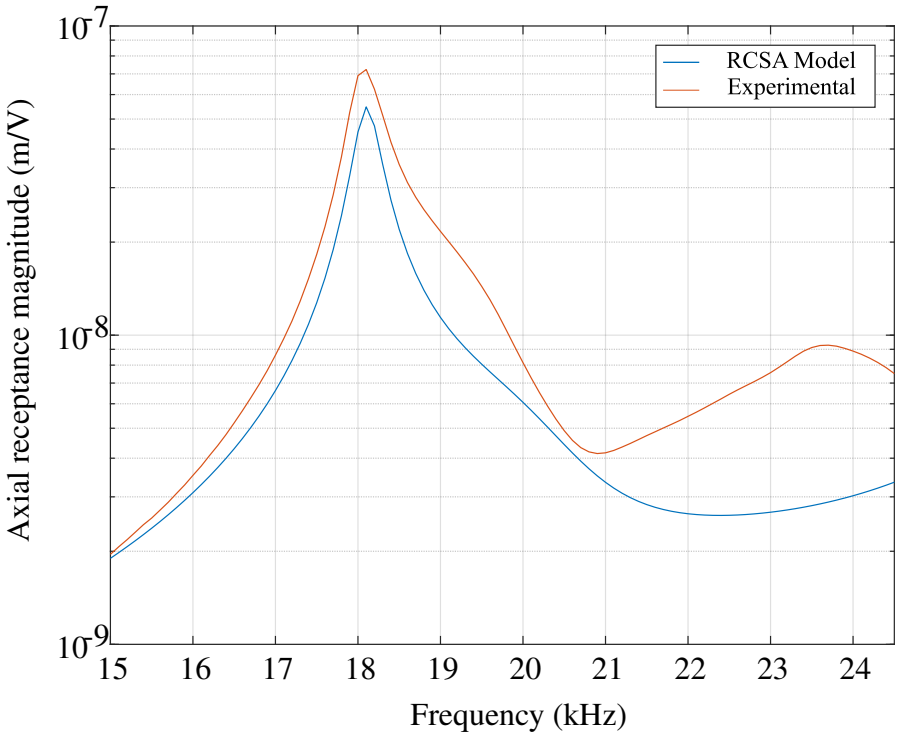

Fig. 4.11 Axial receptance magnitude for 27.5 mm clamped length

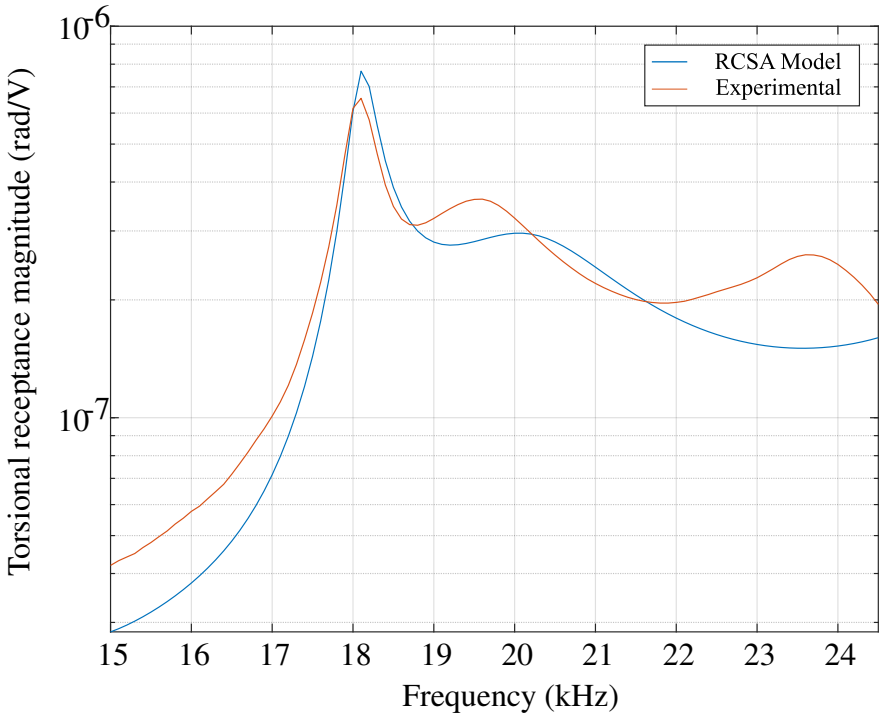

Fig. 4.12 Torsional receptance magnitude for 27.5 mm clamped length

4.5 Structural modification by tuning drillbit clamped length

Tuning the overhang length of the drill bit is one of the techniques that can be used for structural modification of the VAD systems. The case presented in Fig.4.10, Fig.4.11 and Fig.4.12 were for the case of clamping 27.5 mm of the shank length inside the collet.

For the other case, 30 mm of shank length is clamped inside the collet. Joint parameters are identified using current FRF data. Figure 4.13 shows the convergence of current FRF magnitude to the experimental measurement data after convergence of the optimization algorithm.

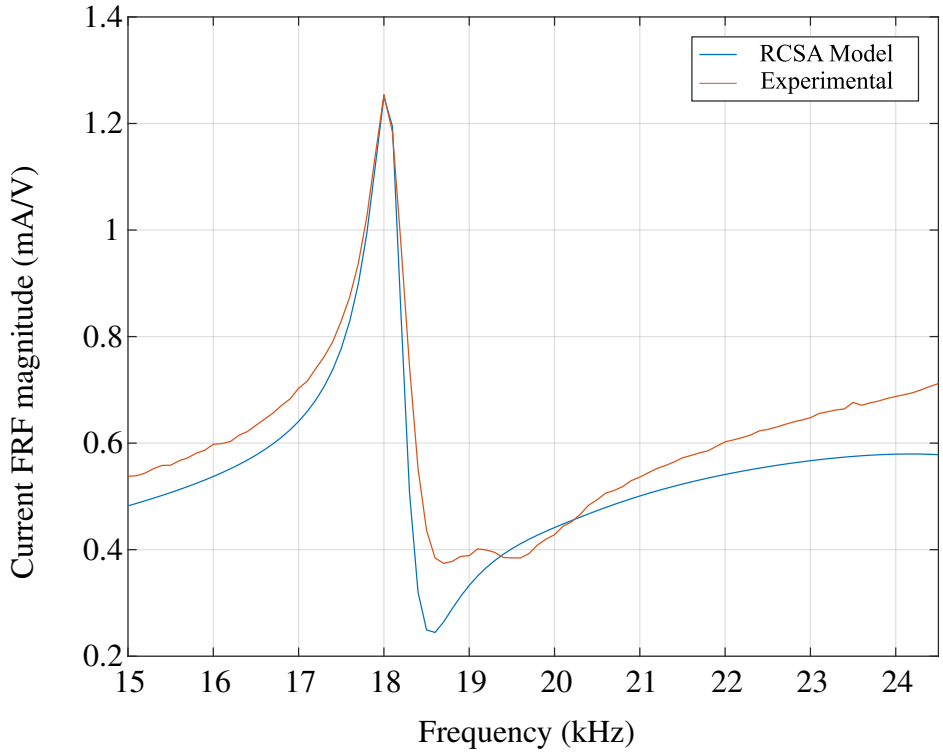

Fig. 4.13 Current FRF magnitude for 30 mm clamped length

The joint parameters computed through the optimization algorithm are as follow

$$\begin{aligned} K^a_{jd} &= 1.5436\text{e}+09[\text{N/m}]; C^a_{jd} = 6.1777\text{e}+07[\text{N.s/m}] \\ K^t_{jd} &= 6.0086\text{e}+02[\text{N.m}]; C^t_{jd} = 1.2600\text{e}+02[\text{N.m.s}] \\ K^a_{jc} &= 7.5839\text{e}+10[\text{N/m}]; C^a_{jc} = 3.1325\text{e}+10[\text{N.s/m}] \end{aligned} \tag{4.24}$$

Axial and torsional receptances of the drill bit tip are computed using the identified values for the joints. The predicted receptances are plotted versus the experimental data in Fig.4.14 and Fig.4.15.

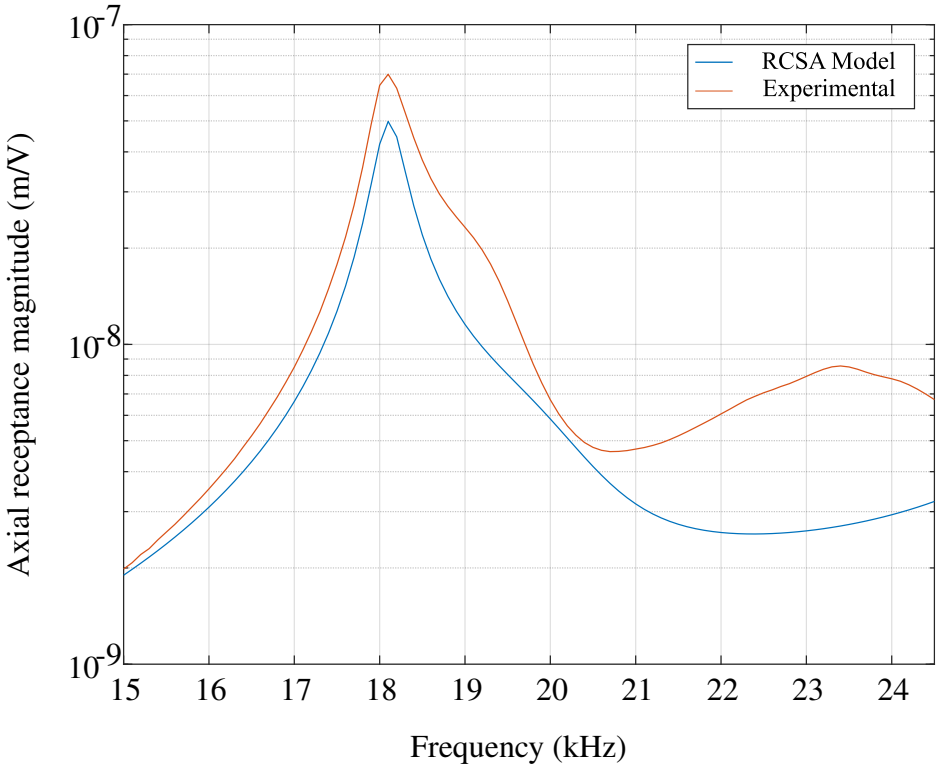

Fig. 4.14 Axial receptance magnitude for 30 mm clamped length

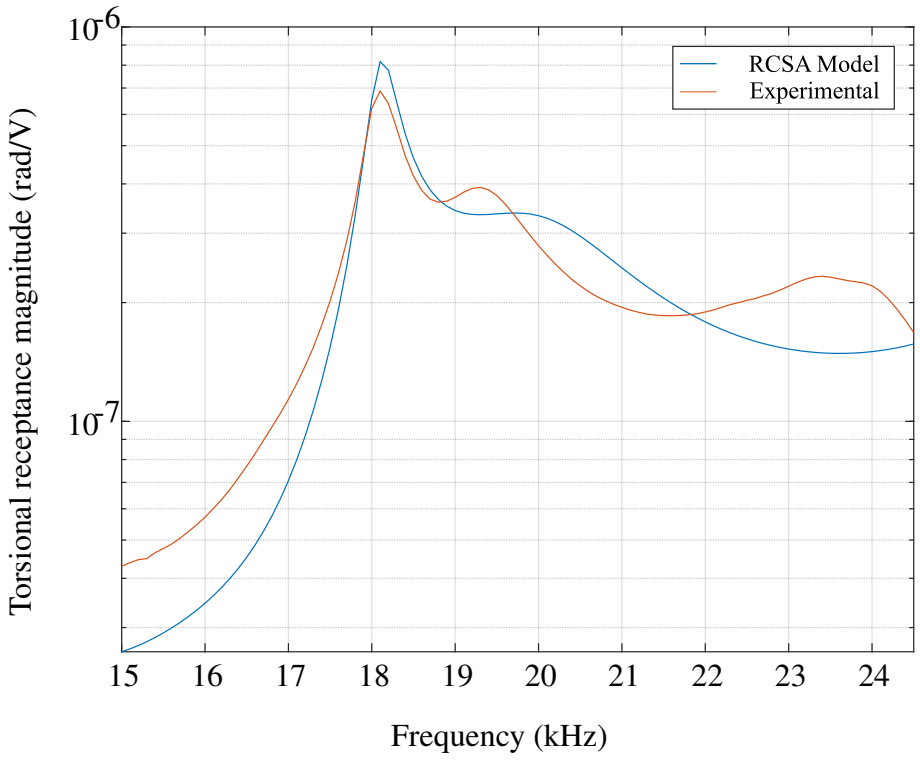

Fig. 4.15 Torsional receptance magnitude for 30 mm clamped length

The case in which 35 mm of shank length is clamped inside the collet is considered. Joint parameters are identified using current FRF data. Figure 4.16 shows with the computed joint parameters, the predicted current FRF and the measured one are in a good agreement.

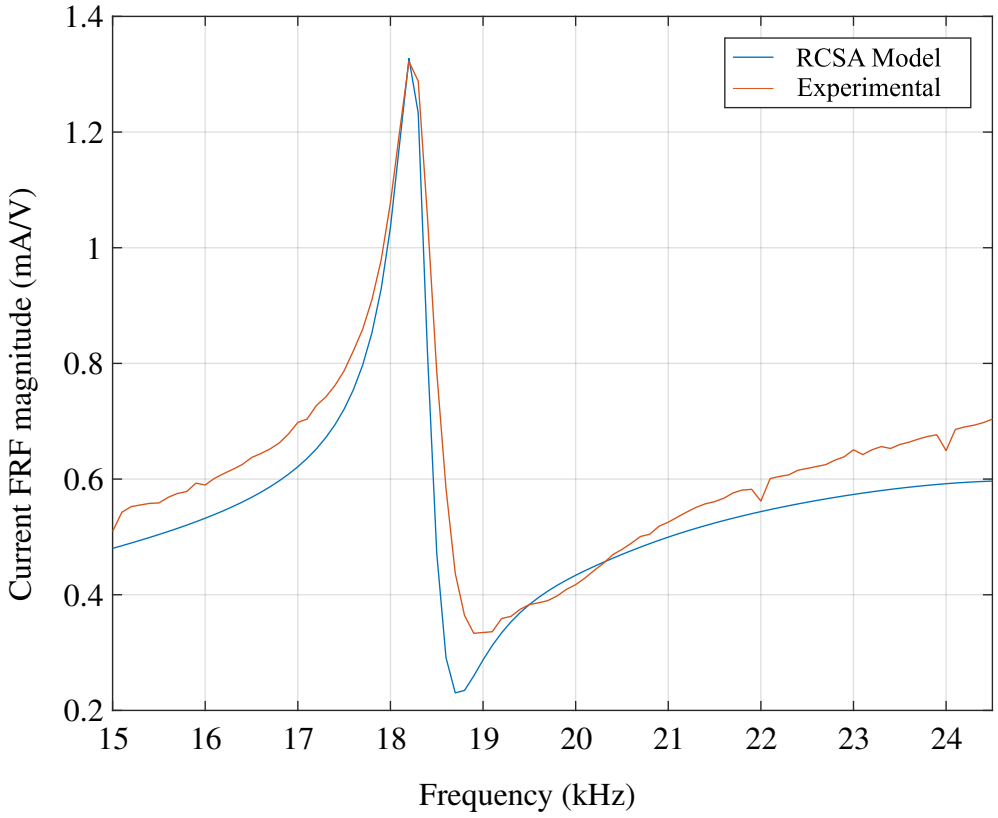

Fig. 4.16 Current FRF magnitude for 35 mm clamped length

The identified joint parameters are as follows

$$\begin{aligned} K^a_{jd} &= 2.8416\text{e}+09[\text{N/m}]; C^a_{jd} = 1.1373\text{e}+08[\text{N.s/m}] \\ K^t_{jd} &= 4.5666\text{e}+02[\text{N.m}]; C^t_{jd} = 9.5759\text{e}+01[\text{N.m.s}] \\ K^a_{jc} &= 7.5839\text{e}+10[\text{N/m}]; C^a_{jc} = 3.1325\text{e}+10[\text{N.s/m}] \end{aligned} \tag{4.25}$$

Axial and torsional receptances of the drill bit tip are computed using the identified values for the joints. The predicted receptances are plotted versus the experimental data in Fig.4.17 and Fig.4.18.

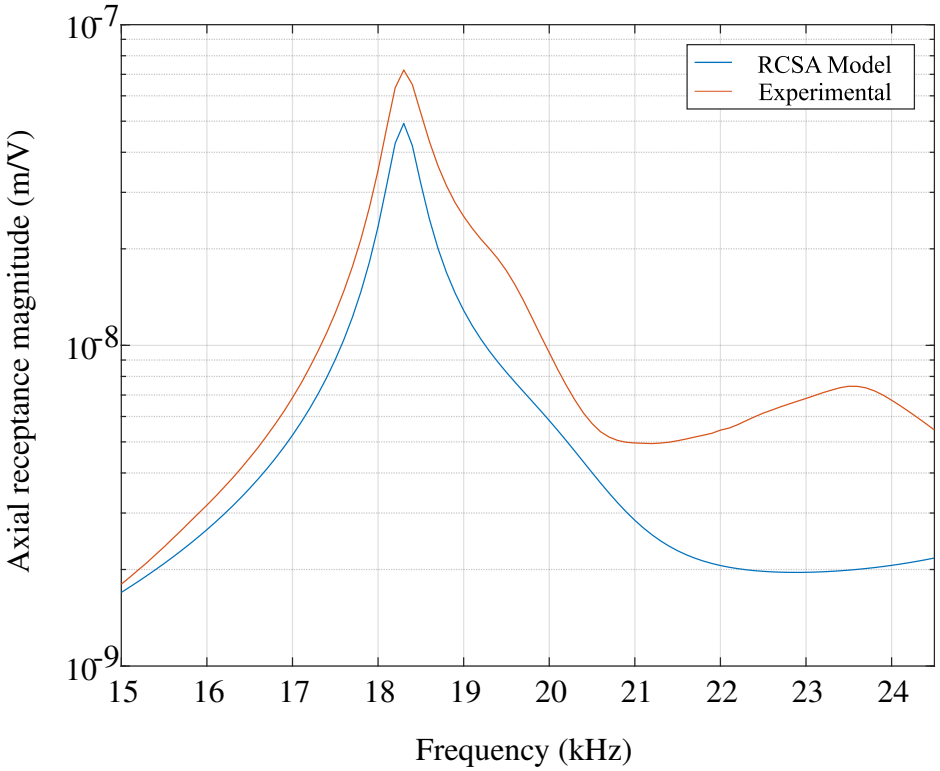

Fig. 4.17 Axial receptance magnitude for 35 mm clamped length

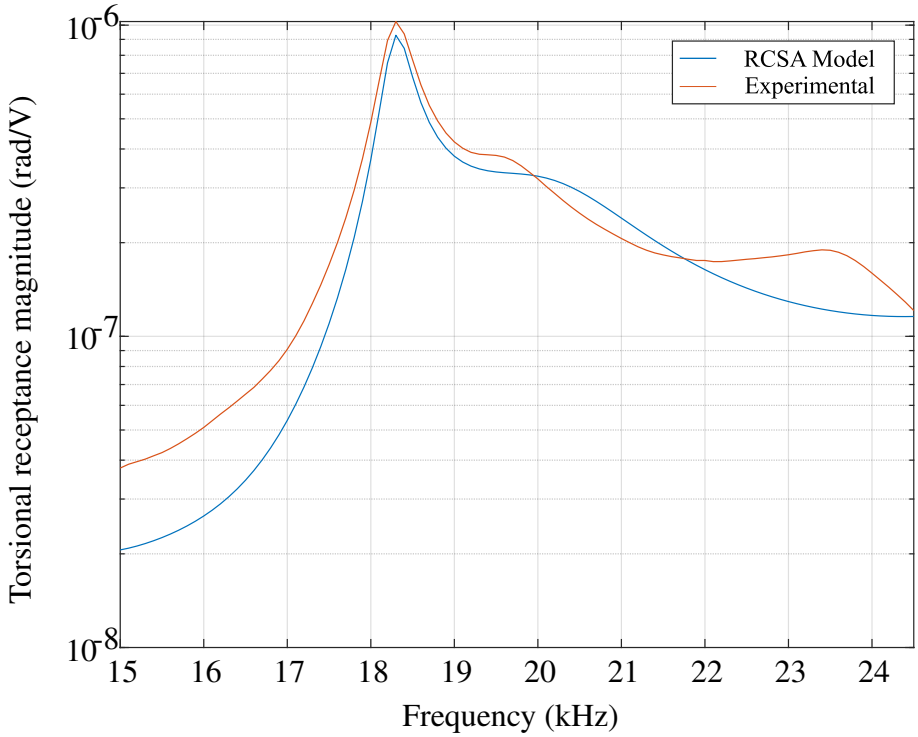

Fig. 4.18 Torsional receptance magnitude for 35 mm clamped length

4.6 Structural modification by electric circuit adjustment

Structural modification by mechanical adjustments in substructures may not be so practical because of assembly limitations. The electro-mechanical coupling of piezoelectric materials enables us to tune mechanical behaviour of the transducer by adjusting electric circuit. In structural modification using electric circuit adjustment [11], this coupling is employed to tune mechanical stiffness of one of the piezoelectric rings while using the other one as an actuator. Fig.4.19 shows how this system is implemented.

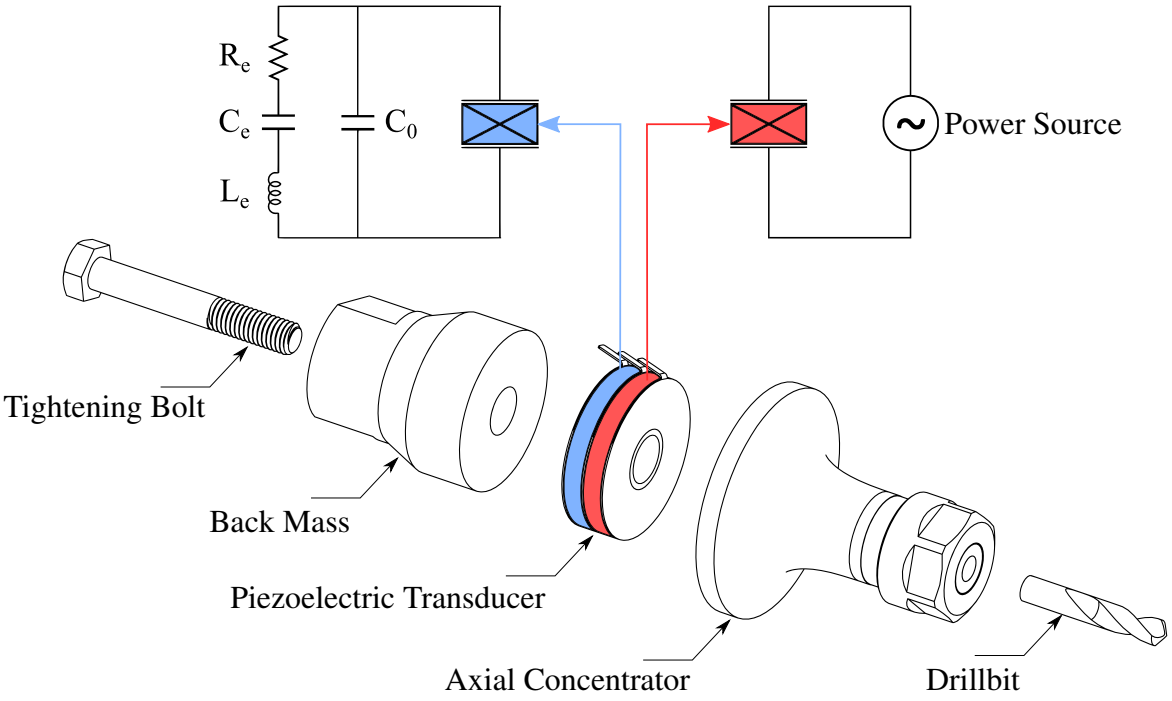

Fig. 4.19 Tool holder with electric circuit adjuster

The RCSA model developed in Chapter 3 needs some modification to be suitable for this application. The subsystem m in this case will be replaced by subsystem m' which is the result of coupling subsystems m and a as shown in Fig.4.20.

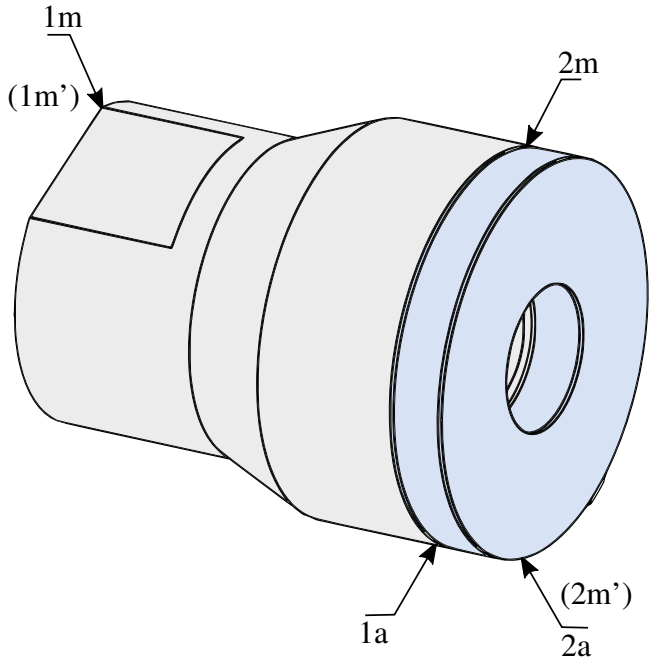

Fig. 4.20 Coupling back mass and adjustable piezoelectric ring

The FRF matrix of subsystem m', according coupling formulation of Section 2.2.2, will become as follows.

$$H_{m'} = \begin{bmatrix} H_{1m'1m'} & H_{1m'2m'} \\ H_{2m'1m'} & H_{2m'2m'} \end{bmatrix}_{4\times4}$$
$$= \begin{bmatrix} H_{1m1m} - H_{1m2m}(H_{2m2m} + H_{1a1a})^{-1} H_{2m1m} & H_{1m2m}(H_{2m2m} + H_{1a1a})^{-1} H_{1a2a} \\ H_{2a1a}(H_{1a1a} + H_{2m2m})^{-1} H_{2m1m} & H_{2a2a} - H_{2a1a}(H_{1a1a} + H_{2m2m})^{-1} H_{1a2a} \end{bmatrix}_{4\times4} \tag{4.26}$$

where FRFs of the subsystem a is obtained using a rod model with a mechanical compliance adjustable by the electrical components. This adjustable mechanical compliance is denoted by S_{adj}. In order to find S_{adj}, a model for the electric circuit shown in Fig.4.19 is required. Consider the circuit in Fig.4.21.

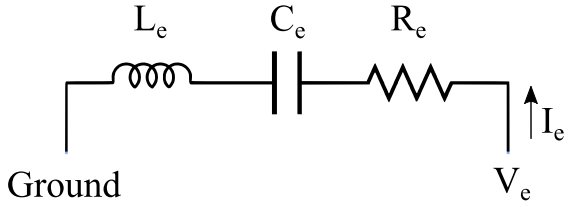

Fig. 4.21 RLC circuit

According to Kirchhoff's voltage law, the governing equation of the circuit shown in Fig.4.21 in the frequency domain is

$$V_e = L_e(j\omega)I_e + R_e I_e + \frac{1}{C_e}\frac{I_e}{(j\omega)} \tag{4.27}$$

where V_e is voltage applied to the RLC circuit and I_e is the current passing through the circuit which are functions of frequency. In Fig.4.21, L_e, C_e and R_e are inductance (H), capacitance (F) and resistance (Ω), respectively. The current FRF H_e is obtained as follow

$$H_e = \frac{I_e}{V_e} = \frac{j\omega}{-L_e\omega^2 + R_e j\omega + \frac{1}{C_e}} \tag{4.28}$$

There is another circuit representative of the piezoelectric capacitance denoted as C_0 that is in parallel with the external circuit as shown in Fig.4.19. Being in parallel means that the same voltage V_e will be applied to both circuits. The current FRF of this circuit denoted by H_0, which only includes the capacitor C_0, is similar to Eq.4.28 but by neglecting the terms corresponding to the inductor and resistor as follow

$$H_0 = \frac{I_0}{V_e} = \frac{j\omega}{\frac{1}{C_0}} \tag{4.29}$$

The constitutive equation of piezoelectric materials mentioned in Eq.2.79 and 2.80, in case of considering piezoelectric capacitance as an external capacitor will be simplified to

$$\varepsilon = S^E\sigma + dE \tag{4.30}$$

$$D = d\sigma \tag{4.31}$$

Writing Eq.4.31 for electric charge by substituting $D = q/A$ becomes

$$q = Ad\sigma \tag{4.32}$$

As mentioned before, the electric current is rate of change in electric charge per time. By substituting the electric charge in Eq.4.32 by the current formulation for two circuits in parallel of $q = (I_e + I_0)/(j\omega)$, the following equation is derived

$$\frac{I_e + I_0}{j\omega} = Ad\sigma \tag{4.33}$$

By substituting the corresponding current FRF from Eq.4.28 and Eq.4.29 into Eq.4.33, voltage can be described as a function of the mechanical stress applied to the piezoelectric material

$$(H_e + H_0)V_e = j\omega Ad\sigma \rightarrow V_e = \frac{j\omega Ad}{H_e + H_0}\sigma \tag{4.34}$$

By considering the relation between electric field and voltage of $E = V/l$ and substituting Eq.4.34 in Eq.4.30, the following equation will be obtained that describes a relation between mechanical stress and mechanical strain:

$$\varepsilon = (S^E - \frac{j\omega Ad^2}{(H_e + H_0)l})\sigma \tag{4.35}$$

Therefore, the mechanical compliance of the piezoelectric ring used as the adjustable subsystem a , which is modified by the electric circuit dynamics, will be obtained as follow

$$S_{adj} = S^E - \frac{j\omega Ad^2}{(H_e + H_0)l} \tag{4.36}$$

The effect of tuning each electrical component on the dynamic response of the VAD tool holder assembly is studied.

In Fig.4.22 and Fig.4.23, the effect of tuning R_e is on dynamics of the assembly is studied. Inductor (L_e) and capacitor (C_e) are neglected. As can be seen in the corresponding figures, by increasing the external resistance, the resonant frequency of the assembly will increase slightly in a limited range of frequency which is less than 200 Hz.

In Fig.4.24 and Fig.4.25, the effect of tuning the inductor L_e with a fixed capacitor value of $C_e = 1nF$ is considered. As can be seen in the corresponding figures, by increasing the external inductance, the resonant frequency of the assembly will decreases in a wider range of frequency, in a range of more than 2 kHz. The inductor has been observed to have the most significant effect on the dynamics of the tool holder structure.

In Fig.4.26 and Fig.4.27, the effect of tuning capacitor value of C_e with a fixed inductor value of $L_e = 50mH$ is presented. As can be seen in the corresponding figures, by increasing the external capacitance, the resonant frequency of the assembly will decrease in a range of frequency which is about 2 kHz.

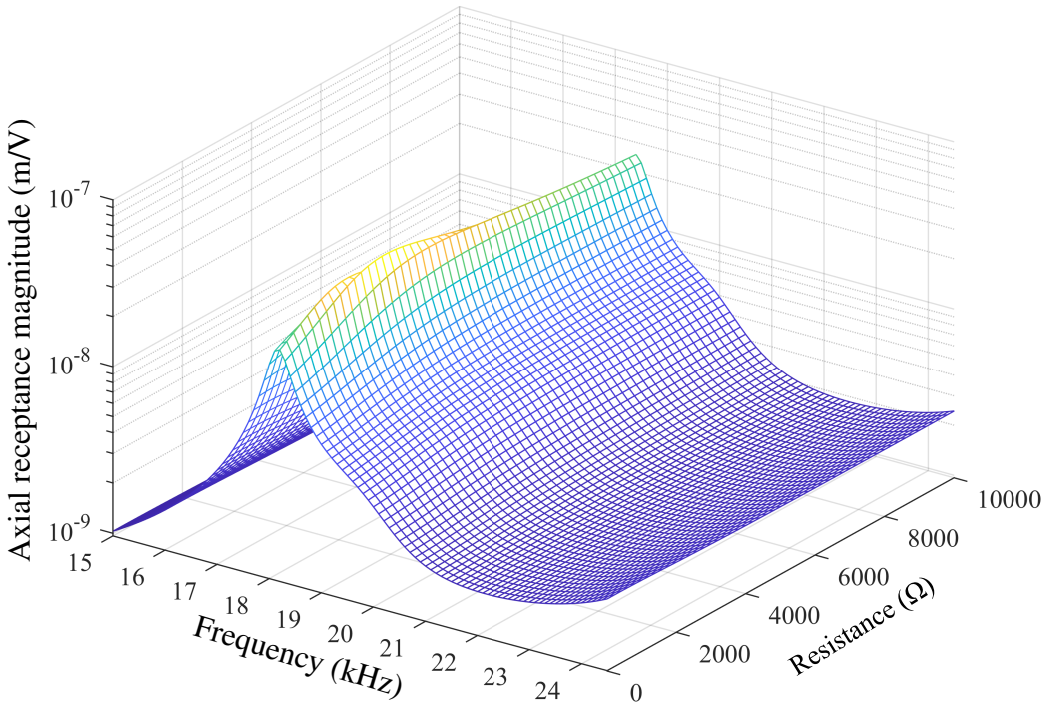

Fig. 4.22 Effect of tuning resistance on the axial receptance of the assembly

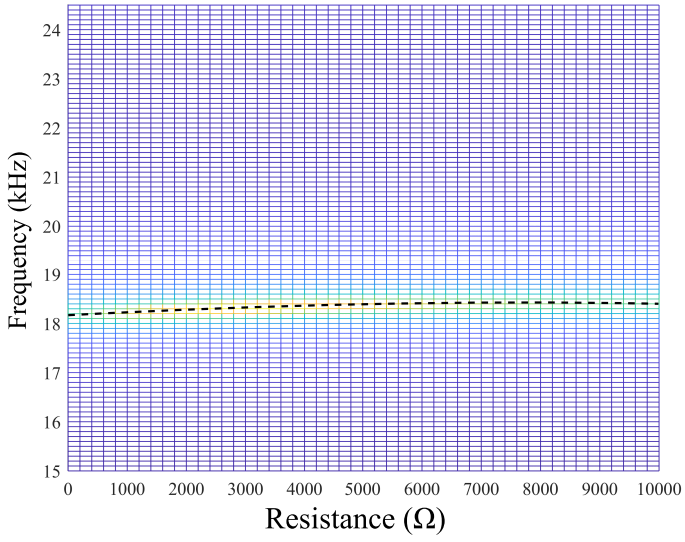

Fig. 4.23 Effect of tuning resistance on operational frequency of the Assembly

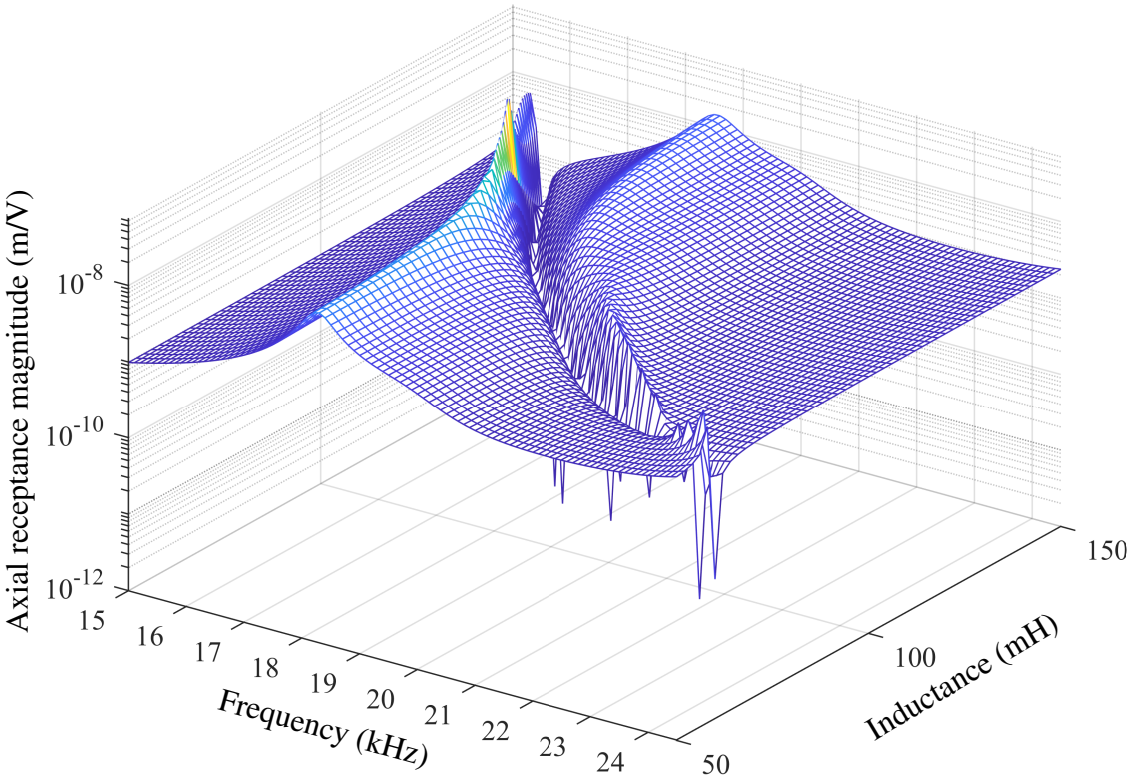

Fig. 4.24 Effect of tuning inductance on the axial receptance of the assembly

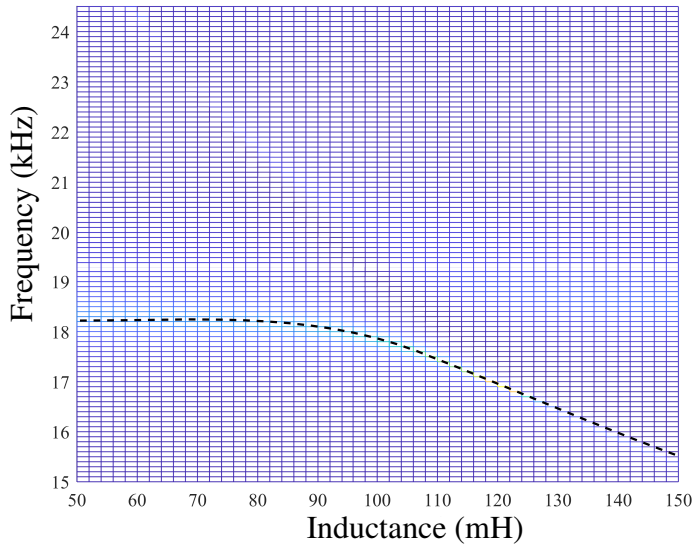

Fig. 4.25 Effect of tuning inductance on operational frequency of the Assembly

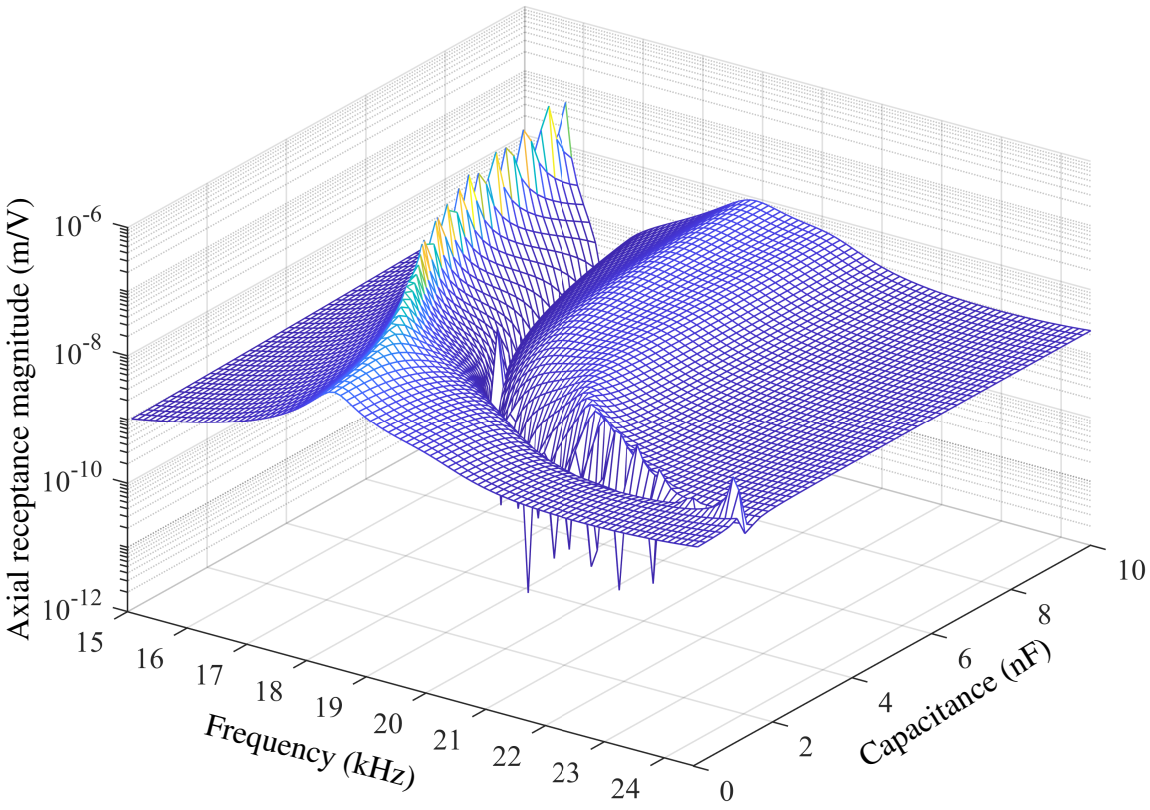

Fig. 4.26 Effect of tuning capacitance on the axial receptance of the assembly

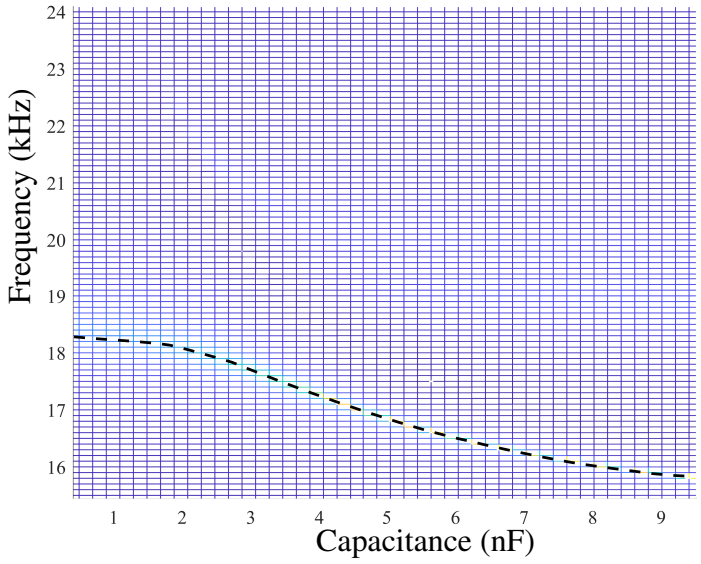

Fig. 4.27 Effect of tuning capacitance on operational frequency of the Assembly

Chapter 5

Conclusions and Future Work

In this thesis, the dynamics of the VAD tool holders were studied in a substructure coupling platform. Analytical models suitable for the geometry of each individual component were employed which increased the computational efficiency of the model. Also, experimental identification of the stiffness and damping of the joints between substructures was the other advantage of a substructure modeling. It was shown that the model can also predict the electric current FRF of the piezoelectric transducer, which is the most convenient way of monitoring the dynamics of the tool holder. The electro-mechanical coupling of piezoelectric material enables us to adjust its mechanical compliance through the RLC circuit tuning which provides the active structural modification ability.

The developed substructure coupling analysis method can be used to fine-tune the dynamics of the VAD system to maximize the performance of the VAD machining process in various machining conditions. It was shown that the model can accurately predict axial and torsional receptances of the drill-tip and also the electric current FRF of the VAD system. It was shown that the model, whose joint parameters are identified using the electric current FRF, can predict the axial and torsional receptance of the system with a good accuracy. This shows that the electric current data is a promising approach for assessments of the system which facilitates experiments, saves time and requires inexpensive equipment. The modeling with consideration of the individual components provided the ability of modifying the overall system dynamics by either mechanical or electrical adjustments to the substructures after the tool holder was manufactured.

Summary

The following is the summary of this thesis:

- An electro-mechanical substructure analysis was presented which provides the ability of designing axial and axial-torsional VAD systems with optimal dynamic performance.
- The stiffness and damping of the joints were considered and identified using experimental data.
- Modification of the VAD system by adjusting the parameters of mechanical and electrical components was the other advantage provided by the substructure analysis platform.

Potential Future Research Topics

- **Prediction of cutting forces by electric current measurement**
  The machining forces are typically measured using dynamometers. Using dynamometers are expensive and is subject to some limitations by the machine fixture. Electric current can easily been measured during the machining process. Since the model can provide information about electric current FRF, a model can be developed based on that to predict machining forces from the electric current measurements.
- **Automatically adjusting electric circuit**
  A VAD system is originally designed to have the best performance with a particular drill bit. However, the design and manufacturing VAD tool holders for each drill bit is not affordable. Developing a method to automatically adjust the electric components of the VAD system, will make the tool holder to be used for several different drill bits with the highest efficiency.
- **Real-time updating of stability lobe diagrams**
  Stability lobe diagrams are used to predict stable machining conditions. In developing a stability lobe diagram, the dynamics of the machining tool and workpiece plays the most important role. In the machining process, since the material is being removed from the workpiece and machining condition changes, the stability lobe diagram may not be accurate for the new machining condition. Having an accurate stability lobe diagram can determine the machining condition with the highest productivity. The electric current measurement from the VAD tool holder provides the ability of updating the dynamics of the machining structure which leads to real-time updating of the stability lobe diagram and maintains the machining process in the highest productivity.

References

[1] Al-Budairi, H., Lucas, M., and Harkness, P. (2013). A design approach for longitudinal–torsional ultrasonic transducers. *Sensors and Actuators A: Physical*, 198:99–106.

[2] Alam, K., Mitrofanov, A., and Silberschmidt, V. V. (2011). Experimental investigations of forces and torque in conventional and ultrasonically-assisted drilling of cortical bone. *Medical engineering & physics*, 33(2):234–239.

[3] Astashev, V. K. and Babitsky, V. I. (2007). *Ultrasonic processes and machines: dynamics, control and applications*. Springer Science & Business Media.

[4] Azarhoushang, B. and Akbari, J. (2007). Ultrasonic-assisted drilling of inconel 738-lc. *International Journal of Machine Tools and Manufacture*, 47(7-8):1027–1033.

[5] Brehl, D. and Dow, T. (2008). Review of vibration-assisted machining. *Precision engineering*, 32(3):153–172.

[6] Cardoni, A., Harkness, P., and Lucas, M. (2010). Ultrasonic rock sampling using longitudinal-torsional vibrations. *Physics Procedia*, 3(1):125–134.

[7] Chang, S. S. and Bone, G. M. (2005). Burr size reduction in drilling by ultrasonic assistance. *Robotics and computer-integrated manufacturing*, 21(4-5):442–450.

[8] Harkness, P., Lucas, M., and Cardoni, A. (2012). Coupling and degenerating modes in longitudinal–torsional step horns. *Ultrasonics*, 52(8):980–988.

[9] Jin, X. and Koya, N. G. (2016). Investigation of warping effect on coupled torsional-axial vibration of drilling tool. *The International Journal of Advanced Manufacturing Technology*, 86(9-12):2961–2974.

[10] Kadivar, M., Akbari, J., Yousefi, R., Rahi, A., and Nick, M. G. (2014). Investigating the effects of vibration method on ultrasonic-assisted drilling of al/sicp metal matrix composites. *Robotics and Computer-Integrated Manufacturing*, 30(3):344–350.

[11] Lin, S., Guo, H., and Xu, J. (2018). Actively adjustable step-type ultrasonic horns in longitudinal vibration. *Journal of Sound and Vibration*, 419:367–379.

[12] Liu, S., Shan, X., Cao, W., Yang, Y., and Xie, T. (2017). A longitudinal-torsional composite ultrasonic vibrator with thread grooves. *Ceramics International*, 43:S214–S220.

[13] Makhdum, F., Phadnis, V. A., Roy, A., and Silberschmidt, V. V. (2014). Effect of ultrasonically-assisted drilling on carbon-fibre-reinforced plastics. *Journal of Sound and Vibration*, 333(23):5939–5952.

[14] Moghaddas, M., Short, M., Wiley, N., Yi, A., and Graff, K. (2018). Improving productivity in an ultrasonic-assisted drilling vertical machining center. *Journal of manufacturing science and engineering*, 140(6).

[15] Moheimani, S. R. and Fleming, A. J. (2006). *Piezoelectric transducers for vibration control and damping*. Springer Science & Business Media.

[16] Neugebauer, R. and Stoll, A. (2004). Ultrasonic application in drilling. *Journal of materials processing technology*, 149(1-3):633–639.

[17] Paktinat, H. and Amini, S. (2018). Numerical and experimental studies of longitudinal and longitudinal-torsional vibrations in drilling of aisi 1045. *The International Journal of Advanced Manufacturing Technology*, 94(5-8):2577–2592.

[18] Rao, S. S. (2005). Mechanical vibrations (si edition).

[19] Rosen, A. (1983). Theoretical and experimental investigation of the nonlinear torsion and extension of initially twisted bars.

[20] Sanda, A., Arriola, I., Navas, V. G., Bengoetxea, I., and Gonzalo, O. (2016). Ultrasonically assisted drilling of carbon fibre reinforced plastics and ti6al4v. *Journal of Manufacturing Processes*, 22:169–176.

[21] Schmitz, T. L. (2010). Torsional and axial frequency response prediction by rcsa. *Precision engineering*, 34(2):345–356.

[22] Schmitz, T. L. and Smith, K. S. (2011). *Mechanical vibrations: modeling and measurement*. Springer Science & Business Media.

[23] Shao, Z., Jiang, X., Li, Z., Geng, D., Li, S., and Zhang, D. (2019). Feasibility study on ultrasonic-assisted drilling of cfrp/ti stacks by single-shot under dry condition. *The International Journal of Advanced Manufacturing Technology*, 105(1-4):1259–1273.

Appendix A

Receptance Coupling Formulation

A.1 Axial receptance coupling

Coupling receptances of subsystems to obtain the receptance of the assembled system using RCSA approach was introduces in Chapter 2. The detailed derivation of RCSA formulation with the approach by Tony Schmitz is presented. [22].

In the simplest case of substructure coupling for rigid coupling of two substructures in one direction as shown in Fig.2.1, has the compatibility and equilibrium conditions as mentioned in Eq.2.6 and Eq.2.7, respectively.

Let's assume that displacement of the coupled system at the point of $1ab$ is desired. This DOF has the same value of $1a$. This displacement can be caused by the forces applied directly at $1ab$ or the forces applied at $2ab$. Considering subsystem a, this displacement is a function of the forces applied to the subsystem a at $1a$ and the coupling location $2a$. The following equation describes this relation

$$x_{1a} = h_{1a1a} f_{1a} + h_{1a2a} f_{2a} \tag{A.1}$$

Since the displacement of the coupling DOF is not of interest, the displacements of the assembled system should be only functions of forces applied to non-coupling DOFs. Eq.A.1 in the assembled system coordinate system will be written as follows

$$x_{1ab} = h_{1a1a} f_{1ab} + h_{1a2a} f_{2a} \tag{A.2}$$

which includes the force applied to the subsystem a at the coupling DOF. This force f_{2a} should be replaced by the force applied at DOF $2ab$. The goal at this stage is to find a relation between f_{2a} and f_{2ab} while $f_{2ab} = f_{2b}$. By substituting the displacements in Eq.2.6, the

following equation is obtained

$$h_{2a1a}f_{1a} + h_{2a2a}f_{2a} = h_{1b1b}f_{1b} + h_{1b2b}f_{2b} \tag{A.3}$$

The substitution of the equilibrium condition from Eq.2.7 and rearranging enable solving for f_{2a}:

$$f_{2a} = -(h_{2a2a} + h_{1b1b})^{-1}h_{2a1a}f_{1a} + (h_{2a2a} + h_{1b1b})^{-1}h_{1b2b}f_{2b} \tag{A.4}$$

By substituting the relation of f_{2a} from Eq.A.4 in Eq.A.2 and considering that $f_{1ab} = f_{1a}$ and $f_{2ab} = f_{2b}$, the displacement x_{1ab} will be determined.

$$x_{1ab} = [h_{1a1a} - h_{1a2a}(h_{2a2a} + h_{1b1b})^{-1}h_{2a1a}]f_{1ab} + [h_{1a2a}(H_{2a2a} + h_{1b1b})^{-1}h_{1b2b}]f_{2ab} \tag{A.5}$$

Following the same procedure leads to a relation for the displacement at DOF $2ab$. This DOF has the same displacement as $2b$. This displacement can be caused by forces applied directly on the same DOF or forces applied on other DOFs. Considering subsystem b, this displacement is a function of the forces applied to the subsystem b at $2b$ and coupling DOF $1b$. The following equation describes this relation

$$x_{2b} = h_{2b1b}f_{1b} + h_{2b2b}f_{2b} \tag{A.6}$$

The displacements of the assembly should be only functions of forces applied to non-coupling DOFs. Eq.A.6 in the assembled system coordinate system will be written as follows

$$x_{2ab} = h_{2b1b}f_{1b} + h_{2b2b}f_{2ab} \tag{A.7}$$

which includes the force applied to the subsystem b at the coupling DOF $1b$ that does not exists in the assembled system. So, the force f_{1b} should be replaced by the force applied at $1ab$. The goal at this stage is to find a relation between f_{1b} and f_{1ab}, which is the same force of f_{1a} acting on subsystem a. By substituting the displacements in Eq.2.6, the following equation is obtained

$$h_{2a1a}f_{1a} + h_{2a2a}f_{2a} = h_{1b1b}f_{1b} + h_{1b2b}f_{2b} \tag{A.8}$$

The substitution of the equilibrium condition from Eq.2.7 and rearranging it enables solving for f_{1b}:

$$f_{1b} = (h_{1b1b} + h_{2a2a})^{-1}h_{2a1a}f_{1a} - (h_{1b1b} + h_{2a2a})^{-1}h_{1b2b}f_{2b} \tag{A.9}$$

By substituting the relation of f_{1b} in Eq.A.7 and considering that $f_{1ab} = f_{1a}$ and $f_{2ab} = f_{2b}$, the displacement x_{2ab} will be determined.

$$x_{2ab} = [h_{2b1b}(h_{1b1b} + h_{2a2a})^{-1} h_{2a1a}] f_{1ab} + [h_{2b2b} - h_{2b1b}(h_{1b1b} + h_{2a2a})^{-1} h_{1b2b}] f_{2ab} \tag{A.10}$$

According to Eq.A.5 and Eq.A.10, the direct (h_{1ab1ab} and h_{2ab2ab}) and cross (h_{1ab2ab} and h_{2ab1ab}) FRFs of the assembly ab are obtained as follows:

$$h_{1ab1ab} = \frac{x_{1ab}}{f_{1ab}} = h_{1a1a} - h_{1a2a}(h_{2a2a} + h_{1b1b})^{-1} h_{2a1a} \tag{A.11}$$

$$h_{1ab2ab} = \frac{x_{1ab}}{f_{2ab}} = h_{1a2a}(H_{2a2a} + h_{1b1b})^{-1} h_{1b2b} \tag{A.12}$$

$$h_{2ab1ab} = \frac{x_{2ab}}{f_{1ab}} = h_{2b1b}(h_{1b1b} + h_{2a2a})^{-1} h_{2a1a} \tag{A.13}$$

$$h_{2ab2ab} = \frac{x_{2ab}}{f_{2ab}} = h_{2b2b} - h_{2b1b}(h_{1b1b} + h_{2a2a})^{-1} h_{1b2b} \tag{A.14}$$

A.2 Axial-torsional receptance coupling

In axial-torsional coupling of subsystems a and b shown in Fig.2.2 the compatibility and equilibrium conditions were mentioned in Eq.2.17 and Eq.2.18, respectively.

In order to compute the displacement vector at $1ab$ which has the same displacement vector as $1a$, it needs to be written as a function of force vectors applied to the subsystem a.

$$X_{1a} = H_{1a1a} F_{1a} + H_{1a2a} F_{2a} \tag{A.15}$$

The force F_{2a} should be replaced by the force applied at $2ab$. The goal at this stage is to find a relation between F_{2a} and F_{2ab}, which is the same force of F_{2b} acting on subsystem b. By substituting the displacement vectors in Eq.2.17, the following equation is obtained

$$H_{2a1a} F_{1a} + H_{2a2a} F_{2a} = H_{1b1b} F_{1b} + H_{1b2b} F_{2b} \tag{A.16}$$

The substitution of the equilibrium condition from Eq.2.18 and rearranging for F_{2a},

$$F_{2a} = -(H_{2a2a} + H_{1b1b})^{-1} H_{2a1a} F_{1a} + (H_{2a2a} + H_{1b1b})^{-1} H_{1b2b} F_{2b} \tag{A.17}$$

By substituting the relation of F_{2a} in Eq.A.15 and considering that $F_{1ab} = F_{1a}$ and $F_{2ab} = F_{2b}$, the displacement vector X_{1ab} will be determined.

$$X_{1ab} = [H_{1a1a} - H_{1a2a}(H_{2a2a} + H_{1b1b})^{-1} H_{2a1a}]F_{1ab} + [H_{1a2a}(H_{2a2a} + H_{1b1b})^{-1} H_{1b2b}]F_{2ab} \tag{A.18}$$

Following the same procedure leads to a relation for the displacement vector at $2ab$:

$$X_{2b} = H_{2b1b}F_{1b} + H_{2b2b}F_{2b} \tag{A.19}$$

By substituting the displacement vectors in Eq.2.17, the following equation is obtained

$$H_{2a1a}F_{1a} + H_{2a2a}F_{2a} = H_{1b1b}F_{1b} + H_{1b2b}F_{2b} \tag{A.20}$$

The substitution of the equilibrium condition from Eq.2.18 and rearranging, F_{1b} is computed

$$F_{1b} = (H_{1b1b} + H_{2a2a})^{-1} H_{2a1a}F_{1a} - (H_{1b1b} + H_{2a2a})^{-1} H_{1b2b}F_{2b} \tag{A.21}$$

By substituting the relation of F_{1b} in Eq.A.19 and considering that $F_{1ab} = F_{1a}$ and $F_{2ab} = F_{2b}$, the displacement vector X_{2ab} will be determined.

$$X_{2ab} = [H_{2b1b}(H_{1b1b} + H_{2a2a})^{-1} H_{2a1a}]F_{1ab} + [H_{2b2b} - H_{2b1b}(H_{1b1b} + H_{2a2a})^{-1} H_{1b2b}]F_{2ab} \tag{A.22}$$

The direct (H_{1ab1ab} and H_{2ab2ab}) and cross (H_{1ab2ab} and H_{2ab1ab}) FRF matrices of the assembled system obtained from Eq.A.18 and Eq.A.22 as follows:

$$H_{1ab1ab} = H_{1a1a} - H_{1a2a}(H_{2a2a} + H_{1b1b})^{-1} H_{2a1a} \tag{A.23}$$

$$H_{1ab2ab} = H_{1a2a}(H_{2a2a} + H_{1b1b})^{-1} H_{1b2b} \tag{A.24}$$

$$H_{2ab1ab} = H_{2b1b}(H_{1b1b} + H_{2a2a})^{-1} H_{2a1a} \tag{A.25}$$

$$H_{2ab2ab} = H_{2b2b} - H_{2b1b}(H_{1b1b} + H_{2a2a})^{-1} H_{1b2b} \tag{A.26}$$